STUDIES OF THE EFFECTS OF SHEAR ON COLLOIDAL AGGREGATION AND GELATION USING SMALL ANGLE LIGHT SCATTERING

by

TAHEREH MOKHTARI

B.S., Sharif University of Technology, 1998

AN ABSTRACT OF A DISSERTATION

submitted in partial fulfillment of the requirements for the degree

DOCTOR OF PHILOSOPHY

Department of Physics
College of Arts and Sciences

KANSAS STATE UNIVERSITY
Manhattan, Kansas

2007

Abstract

We investigated the effect of shear on the structure and aggregation kinetics of unstable colloids using small angle light scattering. We used an aqueous suspension of 20 nm polystyrene latex microspheres and $MgCl_2$ to induce aggregation. The sample was only sheared once for approximately 33 sec at different times, typically 1 min, 5 min, or 15 min, after the onset of aggregation. The average shear rate was in the range of 0.13 - 3.56 sec^{-1}, which was in a laminar regime. The unsheared sample gelled after ca. 45 min. When the sample was sheared soon after the onset of aggregation, the aggregation followed the diffusion limited cluster cluster aggregation (DLCA) kinetics to yield D_f = 1.80 ± 0.04 aggregates unaffected by the shear. The gel time also remained the same as the unsheared gel. Shearing at later stages of aggregation shortened the gel time and enhanced the scattered light intensity significantly indicating rapid growth. Then, depending on the shear rate, there were three different behaviors. At high shear rates, the aggregate structure was inhomogeneous after the shear was stopped with a crossover in slope in the scattered light intensity versus q, to imply hybrid superaggregates with two different fractal dimensions. At intermediate shear rates far from the gel point, there was a similar crossover after the shear was stopped; however, the fractal dimension regained 1.80 ± 0.04 at the gel point. At low shear rates, the aggregation rate was increased, but the aggregate structure was uniform, and the fractal dimension remained 1.75 ± 0.05.

STUDIES OF THE EFFECTS OF SHEAR ON COLLOIDAL AGGREGATION AND GELATION USING SMALL ANGLE LIGHT SCATTERING

by

TAHEREH MOKHTARI

B.S., Sharif University of Technology, 1998

A DISSERTATION

submitted in partial fulfillment of the requirements for the degree

DOCTOR OF PHILOSOPHY

Department of Physics
College of Arts and Sciences

KANSAS STATE UNIVERSITY
Manhattan, Kansas

2007

Approved by:
Major Professor
Chris Sorensen

Abstract

We investigated the effect of shear on the structure and aggregation kinetics of unstable colloids using small angle light scattering. We used an aqueous suspension of 20 nm polystyrene latex microspheres and $MgCl_2$ to induce aggregation. The sample was only sheared once for approximately 33 sec at different times, typically 1 min, 5 min, or 15 min, after the onset of aggregation. The average shear rate was in the range of 0.13 - 3.56 sec^{-1}, which was in a laminar regime. The unsheared sample gelled after ca. 45 min. When the sample was sheared soon after the onset of aggregation, the aggregation followed the diffusion limited cluster cluster aggregation (DLCA) kinetics to yield D_f = 1.80 ± 0.04 aggregates unaffected by the shear. The gel time also remained the same as the unsheared gel. Shearing at later stages of aggregation shortened the gel time and enhanced the scattered light intensity significantly indicating rapid growth. Then, depending on the shear rate, there were three different behaviors. At high shear rates, the aggregate structure was inhomogeneous after the shear was stopped with a crossover in slope in the scattered light intensity versus q, to imply hybrid superaggregates with two different fractal dimensions. At intermediate shear rates far from the gel point, there was a similar crossover after the shear was stopped; however, the fractal dimension regained 1.80 ± 0.04 at the gel point. At low shear rates, the aggregation rate was increased, but the aggregate structure was uniform, and the fractal dimension remained 1.75 ± 0.05.

Table of Contents

List of Figures

List of Tables

Acknowledgement

I would like to express my sincere thanks to many people for their help in various ways during the work represented by this thesis. I am deeply indebted to Dr. Chris Sorensen for his constant support, encouragement, and guidance. Through difficult times, he has been my true and best friend while going out of his way to help me generously. He has taught me countless lessons of physics and life that shall stay with me forever. Beyond showing me the path, he has given me the freedom to follow my own instinct, and I will always be grateful to him.

I would like to thank Dr. Amit Chakrabarti for his helpful suggestions during this work. I have always enjoyed learning from Amit and Chris during our weekly group meeting with their deep understanding of physics and yet explaining difficult subjects in a simple way. Chris and Amit's humble and humorous attitude created a friendly research group.

I acknowledge Dr. Bruce Law for his useful suggestions throughout this work. I would also like to thank Dr. Maghirang for his thorough reading of this manuscript and his useful suggestions on this work. I also acknowledge Dr. Eric Maatta, my research committee chairperson.

I would like to thank Bob Geering and Russ Reynolds, our great machinists in the physics department. In the last couple of years of my research work, Russ always helped me with his great mechanical talent to improve the design and construction of the experimental setup.

My thanks to my family who have always supported me in my decisions and encouraged me throughout my life. I also wish to thank my friends for their great friendship and support.

CHAPTER 1 Introduction

Irreversible aggregation (i.e., non equilibrium growth phenomena) of small particles to form large clusters occurs in a wide variety of natural and technical systems such as aerosol growth, droplet formation, and colloidal aggregation. Aggregation phenomena have attracted a great deal of interest not only in pure science but also in industry where polymers, paints, and biological materials are formed or processed in this way.

It is now well established that the complex, seemingly disordered structure of aggregates can be quantitatively characterized by the use of fractal geometry which has allowed investigators to distinguish between relatively subtle differences that can be caused by changes in the aggregation kinetics (Mandelbrot 1983).

Aggregation of particles can occur due to their Brownian diffusion motion (random walk), convective fluid motion, or gravitational forces. Smoluchowski (1917) was the first to describe the aggregation of particles controlled by Brownian diffusion aggregation and shear-induced aggregation (Drake 1972). Shear-induced aggregation and Brownian aggregation are two mechanisms that exist simultaneously in sheared systems which have been shown to be independent over a wide range of conditions (Swift & Friedlander 1964).

In the Brownian diffusion aggregation process, there are two limiting irreversible aggregating regimes: diffusion-limited cluster aggregation (DLCA) and reaction-limited cluster aggregation (RLCA). The first is observed when the aggregating clusters move due to pure Brownian motion and form a larger cluster once they collide. The latter occurs when a large number of collisions is needed before the clusters stick (Kolb et al 1983, Lin et al 1990b, Lin et al 1990c, Meakin 1983).

Many experimental and theoretical studies have been carried out to investigate the effect of shear flow on the kinetics of aggregation, the resulting size distributions, and structures of

particle aggregates. It has been shown that shear can promote aggregation of colloidal particles (Russel et al 1999). Furthermore, it has been shown that an aggregating system subjected to shear may undergo shear-induced restructuring, shear-induced fragmentation, or a combination of both resulting in more compact aggregates (Selomulya et al 2002).

The previous work has investigated the effect of shear on the structure and kinetics of aggregation in a continuous presence of shear where shear-induced aggregation was dominant over Brownian aggregation during the entire experiment (Flesch et al 1999, Kikuchi et al 2005, Serra & Casamitjana 1998, Serra et al 1997, Spicer et al 1996, Wang et al 2005). In previous shear experiments, mostly large primary particles (0.5 -10 μm) have been used. There are some studies in which relatively smaller particle sizes (15nm-140nm) are used; however, in these experiments shear rates have been relatively high, and hence, fragmentation or restructuring have been observed by these groups (Lin et al 1990a, Selomulya et al 2002, Sonntag & Russel 1986, Torres et al 1991a).

In the work presented here, *in situ* light scattering measurements were performed to investigate the effect of low shear rates (0.13-3.56 $\sec^{-1}$) on an aggregating colloidal system with small primary particles, 20 nm. The shear was applied for a short period of time (ca. 30 sec) and only once. The aggregating system was subjected to shear (only once) at different times after the onset of aggregation. The effect of shear (e.g., fractal dimension, gel time) was studied both in a cluster dilute regime (similar to other works) and in a cluster dense regime. A cluster dilute regime is defined as when the mean nearest neighbor separation R_{nn} is much larger than the aggregates characteristic size R_g; a cluster dense regime is defined as when R_{nn} is comparable with R_g in an aggregating system (Huang et al 1998).

Our results have shown that shear may enhance the aggregation and gelation causing structural modification, not by shear destruction of aggregates (fragmentation or restructuring), but by shear induced growth, a new mechanism by which *superaggregates* form in a shear field.

We also performed a series of light scattering measurements to determine the experimental gel time of an aggregating system in a DLCA regime. Our results are then compared with the theoretical gel time. Our experimental results have shown good agreements between theoretical and experimental gel times only at low volume fractions of the polystyrene particles. Our results have shown that as the volume fraction of the polystyrene solution increases to higher values, the difference between theoretical and experimental values become significantly large. A scaling argument is proposed to explain this discrepancy between the theoretical and experimental gel times, proposing that the initial mixing time of the colloidal solution and the salt concentrations is essentially important in affecting the aggregation rate. Previous studies have shown the comparisons between the theoretical and experimental gel times only in a RLCA regime (Bremer et al 1995, Smith & Zukoski 2006), where the initial mixing time is negligible to the experimental gel time. These groups have found good agreements between the theory and their experimental gel time in a RLCA regime.

Relevant to our light scattering measurements, the extent and effect of multiple scattering on the static light scattering optical structure factor were studied. Our experimental results have shown that the average number of scattering events is a universal parameter to describe the extent of multiple scattering. This quantity can easily be measured or calculated, and hence provides a useful experimental indicator of multiple scattering.

This work includes an introduction to the concept of fractals in Chapter 2, the principles of light scattering in Chapter 3, the Brownian and shear induced aggregation in Chapter 4, followed by the gelation. In Chapter 5, the small angle light scattering setup and the experimental methods are described. We then present our experimental results on studies on the effect of initial mixing on gel time (Chapter 6) and the shear effect on the methodology and the kinetics of aggregation (Chapter 7), and finally the conclusion is given in Chapter 8.

CHAPTER 2 Fractals

Fractals[1] were first introduced and explained by Mandelbrot (Mandelbrot 1983). However, some of the building blocks of fractal geometry originated in the deterministic, exactly self-similar mathematical "monsters" (such as Koch curve and Sierpinski gasket) of the early 1900's (Voss 1989). It is now well established that fractal geometry can be used to describe an incredibly broad range of natural structures and phenomena (Mandelbrot 1983).

One of the common features of fractals is self-similarity. That is, a fractal object can be decomposed into parts geometrically similar to the whole system (Pfeifer & Obert 1989). In general, fractals are self-affine if they are scaled differently in different directions (or scaled anisotropically). However, a self-similar (or self-affine) structure is not necessarily a fractal (Peitgen et al 1991, Vicsek 1992). For example, a cube and any smaller cubes cut out of it are not called fractal (i.e., self-similarity is satisfied in a trivial way).

Fractals in physics never lead to structures with perfect symmetry, since fluctuations are always present in physical processes. Instead, physical fractals are more or less random with no high level of symmetry; in general, any object for which randomness is the basic factor determining the structure will turn out to be fractal over some range of length scales (Stauffer & Stanley 1990). In random fractals, self-similarity is true only in a statistical sense (not exactly), and to describe them it is more appropriate to use the term scale-invariance (i.e., the system looks the same at various magnifications) than self-similarity (Vicsek 1992).

---

[1] Fractal is derived from the Latin word *frangere* which means "to break" (Peitgen et al 1991).

2.1 Examples of Fractals

Figure 2.1 shows several examples of fractals and their self-similarity features. Figure 2.1(a) shows an example of fractals formed via a diffusion limited cluster aggregation (DLCA) process. Romanesco broccoli and its scale invariance feature can be seen in Fig. 2.1(b). In Fig. 2.1(c), an example of diffusion limited aggregation process (DLA) is shown in the breakdown of a dielectric due to electric discharge. Figure 2.1(d) is the familiar example of a crumpled paper ball.

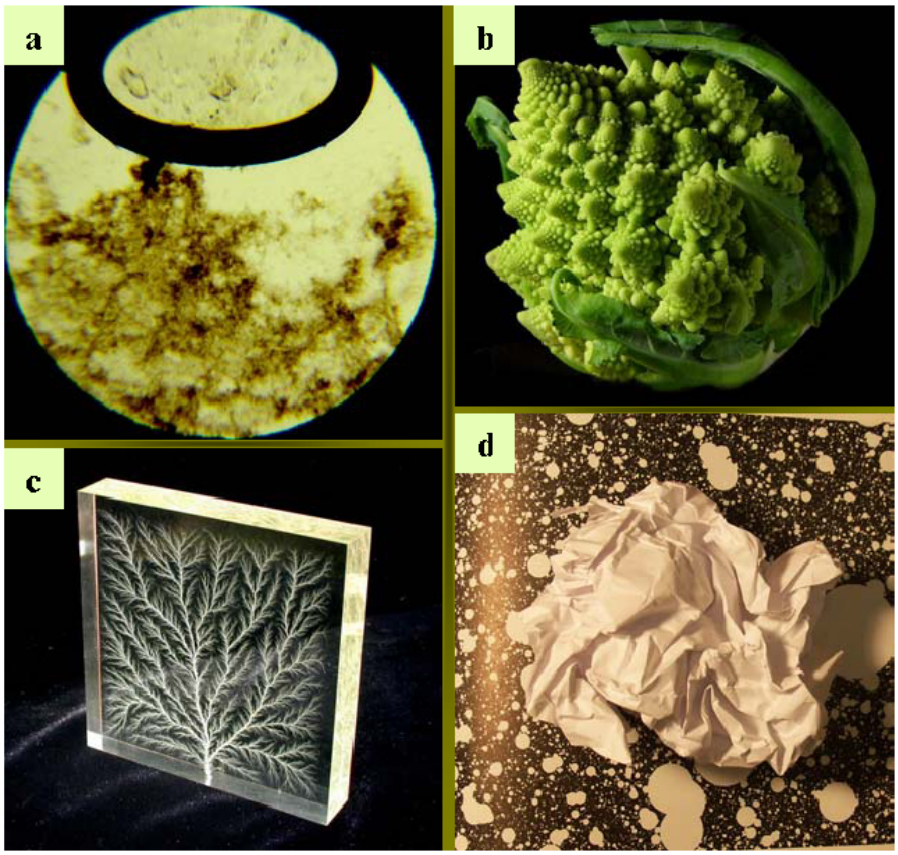

Figure 2.1 (a) Diffusion limited cluster-cluster aggregation of polystyrene nanoparticles, (b) Romanesco broccoli, (c) breakdown of a dielectric due to electric discharge[2], and (d) crumpled paper ball on "Swiss cheese" fractals.

[2] Figures 2.1(b) and (c) were reproduced by permission from www.wikipedia.org.

Figure 2.2 demonstrates how one can construct the Sierpinski gasket using an iteration procedure (Stanley 1985, Stauffer & Stanley 1990). One can start with a triangular-shaped tile with a mass m and of edge length l. For simplicity, the density is defined as $\rho \equiv m/l^2 = 1$. In the first stage, three tiles are joined together to create the structure shown in Fig. 2.2b with the mass of $M = 3m$ and the edge $L = 2l$. As a result, the density has decreased from unity to $3/4$. In the second dilation stage, three of the $\rho = 3/4$ structures constructed in stage one are joined together to build an object with $\rho = (3/4)^2$ (Fig. 2.2(c)). This procedure is iterated up to four stages as shown in Fig. 2.2(e).

As can be seen in Fig. 2.2, the Sierpinski gasket has holes on all length scales, and hence self-similarity can be directly checked in this example, whereas for random fractals, one needs other methods to detect and determine its fractal character that is described in section 2.2.

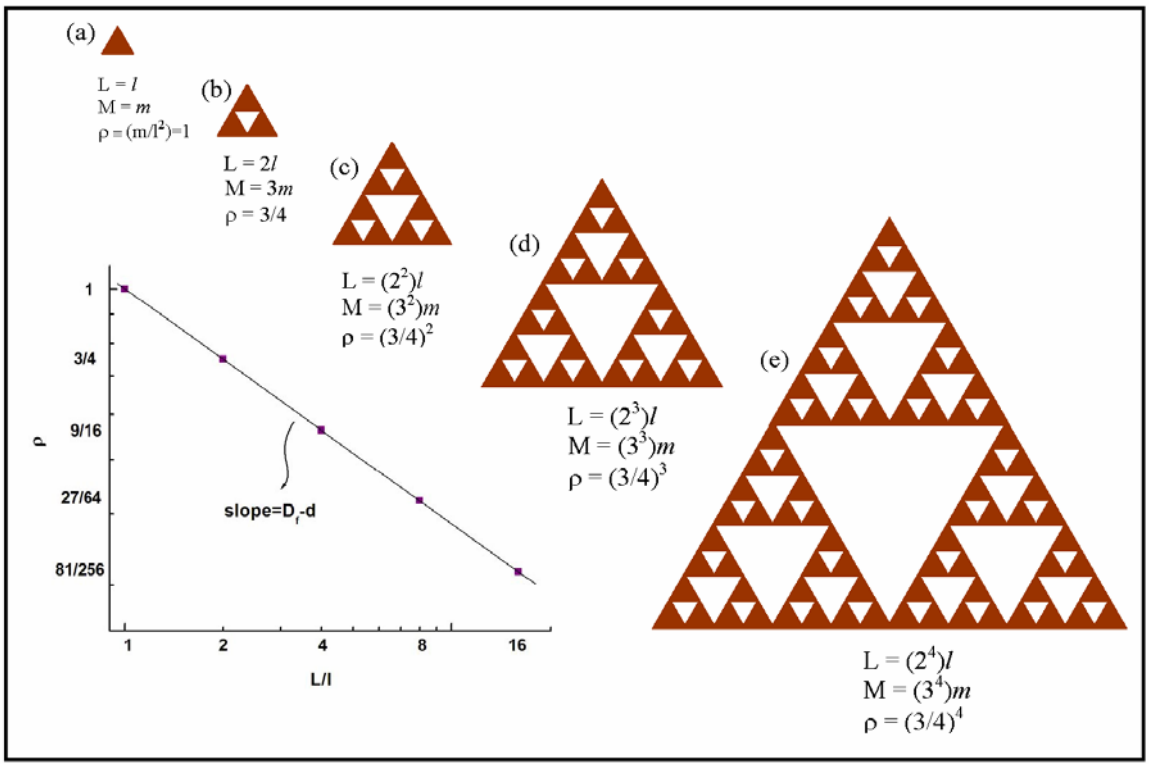

Figure 2.2 The basic construction steps of the Sierpinski gasket which exhibits a fractal dimension of $D_f = 1.58$. The graph on the left is the log-log plot of ρ as a function of L/l.

The graph, shown on the left of Fig. 2.2, is the log-log plot of ρ vs. L/l. It can be shown that the slope of the graph is $\mathrm{D_f} - \mathrm{d}$, where $\mathrm{D_f}$ is the fractal dimension, and d is the Euclidean dimension.

In this particular case, the fractal dimension $\mathrm{D_f}$ can be determined as follows. As can be seen in Fig. 2.2., three replicas of the fractal (i.e., triangle-shaped tile) are required to cover itself after dilation by a factor or 2, and the fractal dimension is given by $\mathrm{D_f} = \log 3 / \log 2 \approx 1.58$. This "definition" of the fractal dimensionality is in accord with our intuitive understanding of dimensionality in Euclidean objects. For example, if a d-dimensional hypercube is dilated by a factor of l in all directions, it can be covered by l^d replicas of the original (undilated) hypercube and the (Euclidean) dimensionality is given by $\mathrm{d} = \log(l^d) / \log l$ (Meakin 1988).

In general, if a self-similar fractal can be covered by N replicas of itself after an isotropic dilation by a factor of l, the fractal dimensionality is given by

$$\mathrm{D_f} = \log N / \log l . \tag{2.1}$$

As can be seen in Fig. 2.2, ρ decreases monotonically with L/l so that by iterating sufficiently one can achieve a fractal as low a density as possible. Furthermore, ρ decreases with L via a simple power law, whereas in Euclidean geometry the density is independent of the length scale on which it is measured (Stanley 1985). In general, the density of fractal objects (i.e., $\mathrm{D_f} < \mathrm{d}$) scales with their linear size as

$$\rho = A\left(\frac{L}{l}\right)^{\mathrm{D_f}-\mathrm{d}}, \tag{2.2}$$

where A is a constant. Because of their low density, fractal aggregates are often mechanically weak structures which can be easily distorted and collapse as a result of gravitational fields,

thermal fluctuations, etc. These effects limit the range of length scales over which fractal scaling can be maintained in real systems (Meakin 1988).

For colloidal aggregates and other random fractals in real space, it is convenient to think of the fractal dimensionality in terms of the scaling relationship between M mass and length L.

$$M \sim (\frac{L}{l})^{D_f}. \tag{2.3}$$

For non-fractal objects (Euclidean), Eqs. (2.2) and (2.3) give a trivial value for D_f, coinciding with the embedding Euclidean dimension (spatial dimension) d (Vicsek 1992).

2.2 Methods for Determining Fractal Dimensions

There are various methods to determine the fractal dimension of aggregating structures in real systems depending on their feasibility and the level of precision of defining the fractal dimension.

2.2.1 Light Scattering Technique

One of the powerful methods (i.e., if feasible) to determine the fractal dimension of aggregate structures is the scattering technique which is discussed in Chapter 3. One can also analyze the image of the fractal structures to determine the fractal dimension as follows:

2.2.2 Box Counting Method

This method provides a very simple and efficient way to determine the fractal dimension of the system, independent of whether the system is a dust, curve, surface, or bulk solid (Pfeifer & Obert 1989). One may divide the fractal structure, with the characteristic linear size of L, into sufficiently fine grids with size l (i.e., $l << L$). One can then count how many of the grids are intersected by the curve or the surface. For a fractal object, one can show that

$$N_{box}(l) = A(\frac{L}{l})^{\mathrm{D_f}}, \tag{2.4}$$

where A (i.e., shape factor) is a constant and the exponent $\mathrm{D_f}$ may have an integer or non-integer value.

In real systems, there is always a lower limit $l_{\min}$ and an upper limit $l_{\max}$ where Eq. (2.4) holds. These limits are called inner and outer cutoff of the fractal regime. A system may be fractal at small length scales and Euclidean at large scales (microporous materials) or vice versa (colloidal aggregates with smooth primary particles) (Pfeifer & Obert 1989). In order to accept an experimental $\mathrm{D_f}$ over a range $l_{\min} < l < l_{\max}$ as well-defined fractal dimension, $l_{\min}$ and $l_{\max}$ should span one decade of length or more. A minimal condition is that $l_{\max}/l_{\min}$ must exceed $2^{1/\mathrm{D_f}}$ (Pfeifer & Obert 1989).

2.2.3 Mass-Radius Method

In this method one chooses a point belonging to the fractal (usually close to its center of mass) and counts the number of sites $N(r)$ (i.e., proportional to mass of the cluster, $M(r)$) belonging to the object within a sequence of spheres of growing radius r . The fractal dimension $\mathrm{D_f}$ is then determined from the relation $M(r) \sim r^{\mathrm{D_f}}$ from the slope of log-log plots of $M(r)$ versus r (Vicsek 1992). If r is smaller than the particle size (inner cutoff) or larger than the linear size of the structure (outer cutoff), the power law behavior breaks down.

2.2.4 Density-Density Correlation Function

This method is an effective procedure to determine the fractal dimension of a random structure (Family et al 1989). The mass-radius method, described above, probes the mass within a given length scale. Whereas the density-density correlation function is an average over many points within a single cluster which is expected to improve the statistics (Vicsek 1992). Thus, in small-scale simulations, or in natural patterns with a limited range of length scales, these two

methods give slightly different values of fractal dimension (Family et al 1989). The density-density correlation function $g(r)$ gives the probability of finding a particle at the position $r + r'$, if there is one at r':

$$g(\vec{r}) = \frac{1}{N}\sum_{r'} \rho(\vec{r} + \vec{r}')\rho(\vec{r}'), \tag{2.5}$$

where N is the number of particles in the cluster, and $\rho(\vec{r})$ is the local density, i.e. $\rho(\vec{r}) = 1$ if the point r belongs to the object, otherwise it is zero. Ordinary fractals are statistically isotropic which means that the correlation functions are not dependent on the direction (i.e., a system without a particular origin site); therefore, $g(\vec{r}) = g(r)$ (Vicsek 1992).

The correlation function (see section 3.5.4.2) for fractal objects can be expressed as

$$g(r) = A(r/\xi)^{\mathrm{D_f}-\mathrm{d}}\, h(r/\xi), \tag{2.6}$$

where A is a normalization constant, $\xi \sim N^{1/\mathrm{D_f}}$ is the radius of the cluster consisting of N particles, and $h(r/\xi)$ is a cutoff function (Vicsek 1992).

According to the scaling assumption, given in Eq. (2.6), if a structure is statistically self-similar, the data obtained for $g(r)$ for various values of N should collapse onto the same universal curve $h(r/\xi)$, when $\ln[(r\xi)^{\mathrm{d-D_f}}\, g(r)]$ is plotted versus $\ln(r/\xi)$ using the correct value for $\mathrm{D_f}$ (Vicsek 1992). Plotting $\ln[(r\xi)^{\mathrm{d-D_f}}\, g(r)]$ versus $\ln(r/\xi)$ verifies the self-similarity and leads to a more reliable estimate of the fractal dimension (Vicsek 1992).

Many times it is the two-dimensional projection of a random fractal (i.e., three-dimensional) which is of interest or can be experimentally studied. If the fractal dimension of the random fractal is less than two $(\mathrm{D_f} < 2)$, one can apply any of the methods described above to

determine the projected fractal dimension D_s which is the same as D_f. However, if $D_f > 2$, the projected fractal dimension is $D_s = 2$, and hence the above methods will break down.

It has been shown that for sufficiently large aggregates, one might generally be able to extract the fractal dimension of a three-dimensional fractal aggregate by quantitatively analyzing the perimeter of its two-dimensional projection (Jullien et al 1994). The perimeter fractal dimension D_p is related to D_f via the following equations

$$\begin{cases} D_p = D_s = D_f & \text{for } D_f < 2, \\ D_p = 1 + (3 - D_f)^{3/2}, D_s = 2 & \text{for } D_f > 2. \end{cases} \tag{2.7}$$

CHAPTER 3 The Principles of Light Scattering

3.1 Introduction

The scientific study of light scattering may be said to have started with the experiments on aerosols by Tyndal (1869) which were followed from 1871 onwards by Lord Rayleigh's theoretical work (Kerker 1969). One motivation for developing a theory of light scattering was the attempt to explain the blue sky which had puzzled many scientists and thinkers ever since Plato (Pesic 2005).

Scattering is hardly restricted to the optical part of the spectrum, and the scattering laws apply with equal validity to all wavelengths (Kerker 1969). The study of electromagnetic scattering is an interdisciplinary activity. Chemists, physicists, biochemists, and various engineers utilize light scattering to study a whole range of materials including gases, pure liquids, colloidal suspensions, glasses, and polymers (Kerker 1969).

Scattering of electromagnetic waves by any system is related to the heterogeneity of that system (Bohren & Huffman 1983, Kerker 1969, van de Hulst 1957). In other words, if light traverses a perfectly homogeneous medium, it is not scattered. Scattering is a result of local density fluctuations in a medium (Bohren & Huffman 1983, van de Hulst 1957) where the number of molecules in a given volume element is different compared with any other instant (Bohren & Huffman 1983). Bohren and Huffman emphasize in their book that the molecules are the scattering agents, and it would be more precise to refer to the fluctuation theory of scattering by molecules rather than to scattering by fluctuations (Bohren & Huffman 1983).

In the presented work, we are only interested in the elastic scattering, i.e., there is no shift of frequency between the incident and the scattered light. Therefore, Raman scattering, Mandelstam-Brillouin scattering, and fluorescence are excluded. Also, we only consider single

scattering and independent scattering (Bohren & Huffman 1983, Mishchenko et al 2002, van de Hulst 1957). The first condition means that the number of scatterers is sufficiently small that the main contribution to the total scattered light by the sample comes from light scattered only once (Bohren & Huffman 1983, van de Hulst 1957). The latter condition means that the particles scatter independently. That is, the particles are many and their separation random so that there is no systematic relation among the phases of the waves scattered by the individual particles; thus, the total light intensity scattered by the collection is just the sum of the light intensity scattered by the individual particles (Bohren & Huffman 1983, van de Hulst 1957).

Light scattering can be classified as static light scattering (SLS) or dynamic light scattering (DLS). Static and dynamic light scattering have similar, yet different aspects which is somehow analogous to yin and yang. In order to gain a better understanding of the light scattering, a brief overview on dynamic light scattering is also given in this chapter.

3.2 Rayleigh Scattering

Rayleigh scattering is the scattering of light, or electromagnetic radiation in general, by particles much smaller than the wavelength. Therefore, the field to which the particle is exposed is approximately uniform over the region occupied by the particle, Eq.(3.1*a*) below. Moreover, the field inside the particle is uniform as well (Bohren & Huffman 1983), see Eq.(3.1*b*). These conditions are satisfied only if

$$\begin{cases} k\,a = 2\pi a/\lambda << 1, & (a) \\ |m|\,k\,a << 1, & (b) \end{cases} \tag{3.1}$$

where k is the wave vector, a is the characteristic length of the particle, λ is the wavelength of light in the medium, and m is the complex refractive index of the particle relative to that of the surrounding medium, e.g., m is a real constant for non-absorbing (dielectric) materials. Thus, in Rayleigh scattering all the elements (sub volumes) of a particle scatter in phase, and hence the scattering intensity would not vary much with direction.

Rayleigh's original derivation is simplicity itself. He applied a very general argument and used a dimensional analysis to derive his main result (Pesic 2005), that is

$$I_s \propto \frac{a^6}{\lambda^4 r^2} I_i \,, \tag{3.2}$$

where I_s and I_i are, respectively, the scattered and the incident light, and r is the distance from the observer to the particle. Rayleigh refined his result ten years later (Pesic 2005) by considering the interaction of (unpolarized) light and particles according to Maxwell's equations. He found

$$I_s = \frac{N k^4 a^6}{2r^2} F(m)(1+\cos^2\theta) I_i \,, \tag{3.3}$$

where N is the number of particles, and

$$F(m) = \left| \frac{m^2 - 1}{m^2 + 2} \right|^2 . \tag{3.4}$$

The range of validity of Eq. (3.3) is roughly when $\lambda / a < 0.05$ (Kerker 1969). Also, the scattered intensity is proportional to $1/\lambda^4$ only if the quantity $F(m)$ (i.e., the Lorentz term) is weakly dependent on wavelength; this is not always true, for example, for metallic particles (Bohren & Huffman 1983).

Equation (3.3) applies to an incident unpolarized light; it is important to know that the angular distribution of the scattered light depends on the polarization of the incident light (Bohren & Huffman 1983). If the incident light is polarized perpendicular to the scattering plane (S-polarization), the scattered intensity is

$$I_s = \frac{N k^4 a^6}{r^2} F(m)\, I_i, \tag{3.5}$$

and if the incident light is polarized parallel to the scattering plane (P-polarization), the scattered intensity then becomes

$$I_s = \frac{N k^4 a^6}{r^2} F(m)(\cos^2\theta)\, I_i. \tag{3.6}$$

There are a number of important features for Rayleigh scattering:

(i) The λ^{-4} dependence: Blue light scatters more than red. This is often associated with the blue sky and the red sunset. However, other factors are involved here including the fact that in perfectly clean air (no particles) scattering occurs from small, thermodynamic fluctuation in the air density (Sorensen 1997).

(ii) The strong size dependence of a^6 is proportional to particle volume squared V_{part}^2. This feature leads to Tyndall effect which describes the increased scattering from an aggregating system of constant mass (Sorensen 1997).

3.3 Rayleigh-Debye-Gans Scattering

The Rayleigh scattering equations are derived under the assumption that the phase of the incident electromagnetic wave does not change across the particle. This is achieved by assuming the size of the particle to be small compared to $\lambda / 2\pi$ ($ka << 1$). This condition can be relaxed if the phase across the particle changes only negligibly relative to the phase change in the surrounding medium (Sorensen 1997). Moreover, if a particle does not have a regular geometrical shape, then it is difficult to solve the scattering problem in its most general form. However, under some assumptions, it is possible to obtain relatively simple approximate expressions for the light scattered by these arbitrary shaped particles. These approximations,

which are the bases of the Rayleigh-Debye-Gans (RDG) theory[3], consider the scattering system (e.g., aggregates, macromolecules) as a set of independent, non-interacting Rayleigh scattering elements (Bohren & Huffman 1983, Kerker 1969, van de Hulst 1957). The fundamental approximation in the Rayleigh-Debye approach is that the phase shift ρ corresponding to any point in the particle be negligible, i.e., that

$$\rho = 2k\,a\left|m-1\right| << 1, \tag{3.7}$$

where a is the characteristic size of the particle. This condition allows for very large particles ($ka > 1$) so long as m is close enough to unity to satisfy the condition. Also, the refractive index is close to one, i.e., that

$$\left|m-1\right| << 1. \tag{3.8}$$

Below some of the important features of the Rayleigh-Debye-Gans theory is given for the light scattering from a uniform dielectric sphere (Berg et al 2005, Sorensen 1997, Sorensen & Fischbach 2000).

(RDG-i) The differential scattering cross section in the scattering plane for S-polarized light is

$$(d\sigma/d\Omega)_{\mathrm{RDG}} = (d\sigma/d\Omega)_{\mathrm{Ray}}\left(\frac{3\sin(qa)-3qa\cos(qa)}{(qa)^3}\right)^2, \tag{3.9}$$

[3] Rayleigh-Debye-Gans scattering is also variably called Rayleigh-Gans (Bohren, 1983;van de Hulst, 1957) or Rayleigh-Debye scattering (Kerker, 1969) depending on the opinion of the author that who has significantly contributed to developing this theory.

In Eq. (3.9), the subscripts RDG and Ray denote Rayleigh-Debye-Gans and Rayleigh, $(d\sigma/d\Omega)_{Ray} = k^4 a^6 F(m)$, and $q = (4\pi/\lambda)\sin(\theta/2)$ (see Eq. (3.15)). For small $qa < 1$, $(d\sigma/d\Omega)_{\mathrm{RDG}} = (d\sigma/d\Omega)_{\mathrm{Ray}}$, and hence $I \propto (qa)^0$.

(RDG-ii) The RDG form is the square of the Fourier transform of the uniform sphere. Thus, for $qa > 1$ $I \propto (qa)^{-4}$ (i.e., Porod regime).

(RDG-iii) The scattering is larger in the forward direction, and this anisotropy increases with increasing size.

3.4 Mie-Lorentz Scattering

Rayleigh's theory was successful in explaining many things such as the blue sky or the red sunset. However, it cannot explain the ruby color of the colloidal gold solutions in which the particles are very small compared to the wavelength of light. Also, even the smallest spheres with $m = \infty$ do not give Rayleigh scattering (van de Hulst 1957).

In 1908, Mie developed the theory of absorption and scattering by an isotropic, homogeneous sphere with a finite arbitrary size and refractive index. His work was an effort to understand the varied colors in absorption and scattering exhibited by small colloidal particles of gold suspended in water (Bohren & Huffman 1983, van de Hulst 1957). It is important to note that Lorentz contributed significantly to developing this theory according to Kerker[4] (Kerker 1969). Although this theory is discussed very briefly in this chapter, the term "Mie-Lorentz" will be used rather than "Mie."

Mie-Lorentz theory is the exact solution of Maxwell's equation for an arbitrary particle. This theory can provide a first-order description of optical effects in nonspherical particles; also,

[4] Kerker notes in his book, "...coincident and consecutive discoveries are common occurrences in science. But certainly if this theory is to be associated with the name or names of individuals, at least that of Lorenz should not be omitted."

it correctly describes many small-particle effects that are not intuitively obvious (Bohren & Huffman 1983). However, it is important to know the extent to which Mie-Lorentz theory is applicable to nonspherical particles; this is discussed further in Ref. (Bohren & Huffman 1983). In brief, nonspherical particles and area-equivalent spheres scatter similarly near the forward direction, but differences between the two tend to increase with increasing scattering angle (Bohren & Huffman 1983). Below some of the important features of the Mie-Lorentz theory is given for the light scattering from a uniform dielectric sphere (Berg et al 2005, Sorensen 1997, Sorensen & Fischbach 2000).

(ML-i) The scattering cross section reduces to the Rayleigh limit as size approaches zero ($\rho \to 0$), and hence $I \propto (qa)^0$.

(ML-ii) The envelope of the Mie-Lorentz scattering curve becomes $I \propto (qa)^{-2}$ for $\rho > 1$ when $qa \le \rho$.

(ML-iii) Mie-Lorentz scattering has an envelope proportional to $I \propto (qa)^{-4}$ when $qa \ge \rho$.

(ML-iv) In the RDG limit ($\rho < 1$ and $|m-1| < 1$), the Mie-Lorentz solution simplifies to the RDG differential cross section (see Eq. (3.9)).

(ML-v) The differential scattering cross section for the regime where θ dependence first occurs is

$$d\sigma / d\Omega = (d\sigma / d\Omega)_{\text{Ray}} (1 - \frac{1}{5} q^2 a^2). \tag{3.10}$$

(ML-vi) The first minimum in Mie-Lorentz scattering that occurs at $qa \approx 3.5$ is roughly universal.

Sorensen and Fischbach (Sorensen & Fischbach 2000) first showed that the Mie-Lorentz scattering evolve from the $\rho \to 0$ limit of Eq. (3.9) to the equations given above for the intensity in (ML-i), (ML-ii), and (ML-iii). Berg et al. (Berg et al 2005) later found a new feature when the scattered intensity is normalized to the Rayleigh differential cross section. Some of these features are briefly discussed here.

Figure 3.1 gives a schematic description of light scattering from a sphere of arbitrary size a and real refractive index.

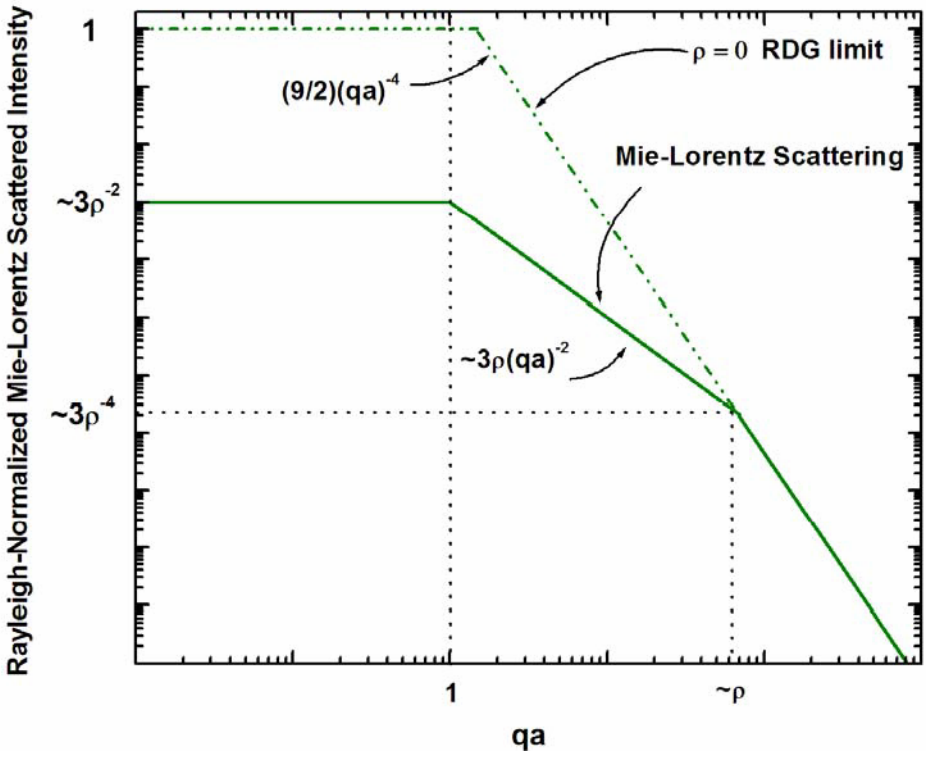

Figure 3.1 Schematic diagram of the Rayleigh-normalized Mie-Lorentz scattering pattern for uniform dielectric spheres of arbitrary size and real refractive index, plotted with green line. The dashed line is the RDG limit, $\rho \to 0$.

In Fig. 3.1, the Rayleigh normalized Mie-Lorentz scattering intensity is plotted versus qa. In the RDG limit (i.e., $\rho = 0$), for $qa < 1$ the RDG curve is flat, i.e., $I \propto (qa)^0$ (RDG-i); for $qa > 1$ the intensity falls off with a negative four power law with magnitude $(9/2)(qa)^{-4}$ (RDG-ii). When ρ increases above one, scattering in the Rayleigh regime decreases relative to true Rayleigh scattering (Berg et al 2005). The relative decrease is proportional to ρ^2 as shown in Fig. 3.1. For $qa > 1$ the scattering falls off as $(qa)^{-2}$ until this

curve crosses the RDG curve for $qa = \rho$ (ML-ii). For $qa \geq \rho$ the scattering is identical to RDG scattering, falling off as $(qa)^{-4}$ for all sizes and refractive indices (ML-iii).

One can apply $qa \approx 3.5$ to approximately estimate the size of the suspended particles in a medium when their size is sufficiently large compared to the wavelength of light (i.e., Mie-Lorentz scattering). Figure 3.2 shows an example of a lunar corona caused by small cloud droplets (left) and a halo caused by a colloidal suspension (right).

Figure 3.2 The picture[5] on the left shows a lunar corona caused by the small clouds droplets. The right picture shows a halo caused by scattering from a suspension of 9.6 μm polystyrene particles in water; the white circle in the center is due to the saturation of the CCD camera.

By knowing or approximately measuring the angular size of the moon (i.e., 0.5^{o}), one can estimate the size of the cloud droplets. We used this approximate formula (i.e., $qa \approx 3.5$) to measure the size of the 9.6 μm polystyrene particles suspended in water. The size of the polystyrene particles was estimated with an error up to 30%.

---

[5] With permission from http://www.atoptics.co.uk/

3.5 The Structure Factor

The structure factor[6] describes the intensity of radiation scattered from a scattering system such as an aggregate or an ensemble of aggregates as a function of the scattering wave vector. The structure factor is both the Fourier transform of the density autocorrelation function of the scattering system and the square of the Fourier transform of the density distribution of the scattering system; thus, it is the q-space description of the structure. Experimentally it describes scattered intensities as a function of scattering angle. Thus, it is of prime importance in light scattering, and therefore, a brief description of the structure factor is given below.

3.5.1 The Scattering Wave Vector

In Fig.3.3, a scalar electromagnetic field with incident wave vector $\vec{k}_i$ hits a scattering element (sub volume) at $\vec{r}$. For simplicity, we have only shown the phase information of the field. The incident field at $\vec{r}$ is

$$E_i(\vec{r}) \propto \exp i(\vec{k}_i \cdot \vec{r}) . \tag{3.11}$$

The field scatters elastically towards the detector placed at a distance $\vec{R}$ from the origin and at an angle θ with respect to the incident beam. In light scattering experiments, the incident light field is sufficiently weak that the system can be assumed to respond linearly to it. Therefore, the scattered field at the detector is

$$E_s(\vec{R}) \propto \exp[i\vec{k}_s \cdot (\vec{R} - \vec{r})] , \tag{3.12}$$

---

[6] Ref (Sorensen 2001) gives a great comprehensive review on principles of light scattering. Hereafter in this chapter, most of the concepts are taken from this reference unless otherwise noted.

where $\vec{k}_s$ is the scattered wave vector, and its magnitude is equal to that of the incident wave vector. The phase at the detector is the sum of the phases of the incident and the scattered field which is

$$E(\vec{R}) \propto \exp[i(\vec{k}_s \cdot \vec{R}) + i(\vec{k}_i - \vec{k}_s) \cdot \vec{r}]. \tag{3.13}$$

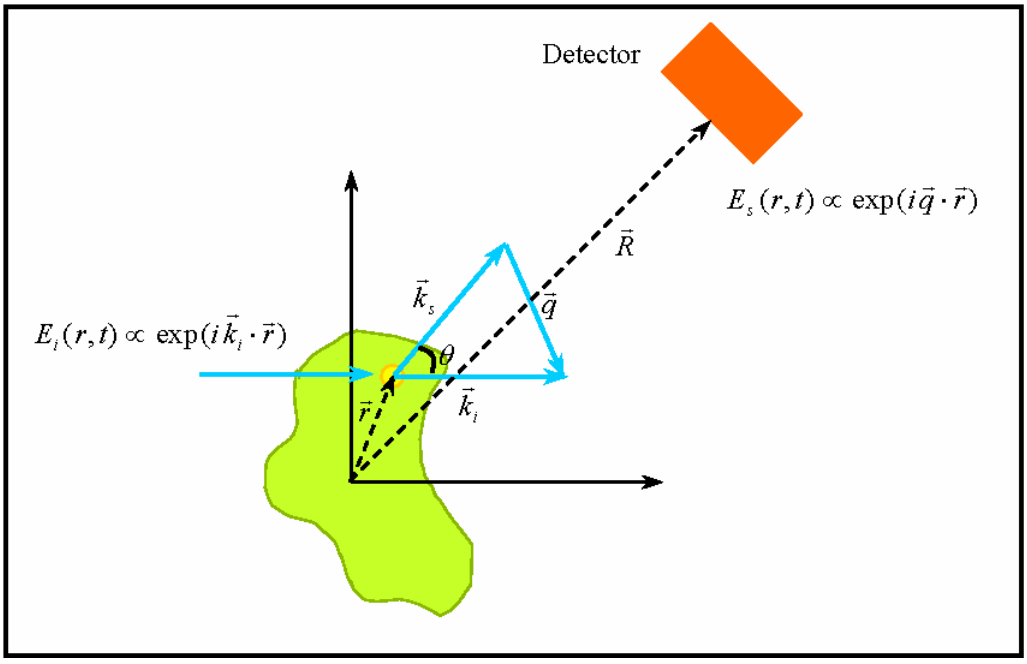

Figure 3.3 The incident field is scattered from a scattering element at $\vec{r}$ toward the detector at a scattering angle θ. The difference of the scattering wave vectors, $\vec{k}_i - \vec{k}_s$, $\vec{q}$ is, scattering wave vector.

The second term in Eq. (3.13) shows that the phase at the detector is a function of the position of the scattering element and $\vec{k}_i - \vec{k}_s$ which is defined as the scattering wave vector, $\vec{q}$. Thus Eq. (3.13) can be simplified to

$$E_s(\vec{R}) \propto \exp i(\vec{q} \cdot \vec{r}). \tag{3.14}$$

The magnitude of $\vec{q}$ can simply be determined from the vector diagram as

$$q = (4\pi / \lambda)\sin(\theta / 2)\,. \tag{3.15}$$

3.5.2 Fundamental Equation for the Structure Factor

Before proceeding to write the general form of the structure factor, let's consider the following assumptions which are the bases of this approach.

(i) The scattering system is consisting of N identical and independent scatterers (see above "scattering element").

(ii) The incident and scattered waves are scalar. This is a plausible assumption in light scattering experiments in which polarization of the incident beam is perpendicular to the scattering plane defined by $\vec{k}_i$ and $\vec{k}_s$, and when multiple scattering is negligible.

(iii) The system is an ensemble of randomly oriented scatterers, hence the structure factor is spherically symmetric $S(\vec{q}) = S(q)$.

The structure factor can therefore be written as the sum of the scattered intensities by all scatterers (scattering elements) in this system, i.e., that

$$S(q) = \sum_{i}^{N}\sum_{j}^{N} \exp[i\vec{q}\cdot(\vec{r}_i - \vec{r}_j)], \tag{3.16}$$

where $\vec{r}_i$ and $\vec{r}_j$ are the positions of i th and j th scatterers.

In Eq. (3.16), $\vec{q}\cdot(\vec{r}_i - \vec{r}_j)$ represents the difference in phase between waves scattered at $\vec{q}$ from points with separation $(\vec{r}_i - \vec{r}_j)$. Thus, if the N scatterers are within the region q^{-1} (i.e., $\vec{q}\cdot(\vec{r}_i - \vec{r}_j) < 1$) the phases of the N scattered waves will be essentially the same, resulting in constructive interference. In this case the total scattered field amplitude will be proportional to

N, and hence the total scattered intensity in Eq. (3.16) will be proportional to N^2. If $\vec{q} \cdot (\vec{r}_i - \vec{r}_j) > 1$, the scattering is incoherent, and the total scattered field amplitude will be proportional to $\sqrt{N}$; therefore, the total scattered intensity will be proportional to N. For example, let's consider the scattering from a fractal aggregate at a scattering angle corresponding to q. Scattering within regions that are smaller than q^{-1} is in phase (i.e., Rayleigh scattering), whereas scattering beyond such regions is incoherent. Thus q^{-1} represents as a probe length for structure of size q^{-1}.

3.5.3 The Scaling Approach for the Structure Factor

In order to obtain the general form of the structure factor based on a scaling approach (Oh & Sorensen 1999, Sorensen 2001), a system of N scatterers in a d-dimensional, spherical region of radius R is considered. These scatterers are separated uniformly by $2a$ from one another. It is known that only fluctuations in density scatter waves in the nonzero scattering angle direction as a consequence of the Ewald-Oseen extinction theorem; thus, all the scattering is due to the surface scattering (Hecht 2002).

The structure factor would vary depending on the length scale q^{-1} of which the system is observed, for example, a movable detector that can be placed at variable angles θ, hence variable q^{-1}. The structure factor for three different regions is as follows:

(i) $q^{-1} > R$: In this case all the scattered waves are in phase at the detector

$$S(q) \propto N^2. \tag{3.17}$$

(ii) $a < q^{-1} < R$: In this regime all scatterers within q^{-1} length scale scatter in phase, and hence $S_1(q) \propto N_q^2$, where N_q is the number of scatterers within the q^{-1} length scale. However, all the scatterers separated by distances greater than q^{-1} scatter incoherently,

and hence $S_2(q) \propto n_q$, where n_q is the number of regions of size q^{-1} needed to cover the surface of the system. The total scattering then becomes $S(q) = S_1(q)S_2(q) \propto n_q N_q^2$. one can then obtain

$$S(q) \propto N^2 (qR)^{-2D_m + D_s}, \tag{3.18}$$

where D_m and D_s are, respectively, mass and surface dimension of the system of scatterers(Sorensen 2001).

(iii) $q^{-1} < a$: In this regime all scatterers scatter randomly, but only those on the surface contribute to the scattering, i.e., that

$$S(q) \propto N^2 (R/a)^{-2D_m + D_s}. \tag{3.19}$$

We now apply the scaling approach to a fractal aggregate, and the possibility of detecting the monomers is excluded for now. In a fractal aggregate, all the monomers are essentially on the surface. Thus, the surface and mass fractal dimension are equal, i.e., $D_m = D_s = D_f < d$, where D_f is the fractal dimension of an aggregate. We also use R_g instead of R for an aggregate, because R is not a proper definition for an aggregate with its indefinite perimeter. The structure factor for a fractal aggregate then becomes

$$S_{\text{fractal aggregate}}(q) \propto \begin{cases} N^2 & q^{-1} > R_g, \\ N^2 (qR_g)^{-D_f} & a < q^{-1} < R_g, \\ N^2 (R_g/a)^{-D_f} = Nk_o & q^{-1} < a. \end{cases} \tag{3.20}$$

In order to simplify the equation for $q^{-1} < a$ regime, $N = k_o (R_g/a)^{D_f}$ was used. However, the monomers can also be observed by a detector depending on the size of the monomers and the technique used to detect these monomers. If we consider a solid sphere where

the separation between its scattering points goes to zero, then we can rewrite Eqs. (3.19) and (3.20) for this situation as

$$S_{\text{sphere}}(q) \propto \begin{cases} 1 & q^{-1} > a, \\ (qa)^{-2D_m + D_s} = (qa)^{-4} & q^{-1} < a, \end{cases} \tag{3.21}$$

where $D_m = d = 3$, $D_s = d - 1 = 2$, and d is the spatial dimension. $S_{\text{sphere}}(q)$ is often called the form factor, and in general it is the scattered intensity function from a single primary particle which could have an arbitrary shape. We can now write the total structure factor, or the scattered intensity $I(q)$, as the product of the structure factor for a fractal aggregate and a spherical monomer (or primary particle), i.e., that

$$I(q) = S_{\text{fractal aggregate}}(q)\, S_{\text{sphere}}(q). \tag{3.22}$$

Figure 3.4 shows the generic behavior of the scattered intensity from a fractal aggregate described as follows:

(i) Rayleigh regime where the scattering from all parts of the aggregate is in phase at the detector.

(ii) Power law (fractal regime) where S(q) versus q functionality is proportional to $(qR_g)^{-D_f}$, and one can obtain the fractal dimension of an aggregating system based on this regime.

(iii) Porod regime (monomer regime) where S(q) versus q functionality is proportional $(qa)^{-4}$. However, based on the Rayleigh-Debye-Gans theory for light scattering from a sphere, there are interference ripples for $qa > 1$; these ripples cannot be obtained by the scaling approach (Sorensen 2001).

(iv) The region shown by the dashed circle is called the Guinier regime. One can obtain the size of the aggregates based on the Guinier analysis given in this chapter. However, we

should note that the curve in this regime is not as sharp as it is predicted by the scaling approach (Sorensen 2001).

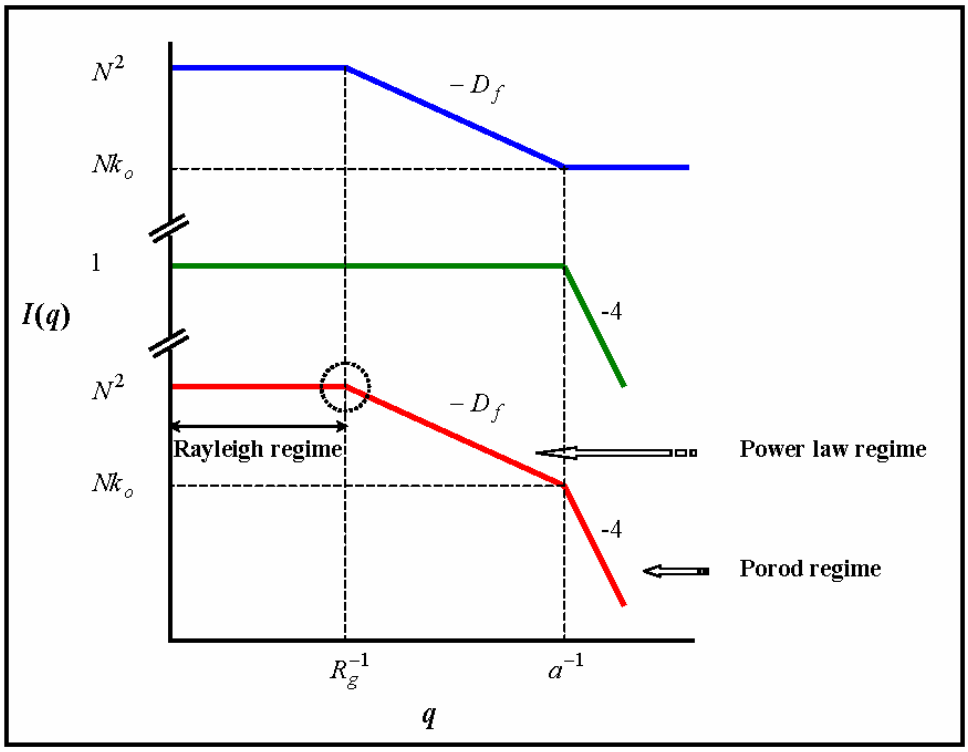

Figure 3.4 Generic illustration of scattering from a fractal aggregate of radius R_g with a fractal dimension of D_f. Upper curve is for a fractal of point particles, second curve is for spherical monomers of radius a, lowest curve is the product of these two structure factors.

3.5.4 Exact Formulation of the Structure Factor

The scaling approach is mostly applicable under the assumption of independent and single scattering (Sorensen 2001). The complete description, however, must account for the facts that the wave might scatter more than once within the aggregate, and the fields across the individual monomers may not be uniform (Sorensen 2001). Rayleigh-Debye-Gans theory can be applied to obtain the structure factor for a fractal aggregate. This theory is a most viable

description for $D_f < 2$ (Sorensen 2001). Below the structure factor for $qR_g < 1$ and $qR_g > 1$ are given:

3.5.4.1 The Guinier Regime: $qR_g < 1$

Guinier analysis (Guinier & Fournet 1955, Jullien 1992, Sorensen 2001) is a useful method to determine the size of the aggregates. One can show that the structure factor is the Fourier transform of the density autocorrelation function $g(r)$ (Sorensen 2001), i.e.,

$$S(\vec{q}) = \int g(\vec{r}) \exp i(\vec{q}.\vec{r})\, d\vec{r}. \tag{3.23}$$

Under the assumption of isotropy, i.e., $S(\vec{q}) = S(q)$ and $g(\vec{r}) = g(r)$ and the solid angle integration of Eq. (3.23) becomes

$$S(q) = 4\pi \int g(r) \frac{\sin qr}{qr} r^2 dr. \tag{3.24}$$

Now by expanding Eq. (3.24) for small qr (Guinier regime), one can obtain[7]

$$S(q) \approx 1 - \frac{q^2}{6} \int r^2 g(r) d\vec{r}. \tag{3.25}$$

It can be shown that the radius of gyration of an aggregate is (Jullien 1992, Sorensen 2001)

$$R_g^2 = \frac{1}{2} \int r^2 g(r) d\vec{r}. \tag{3.26}$$

Therefore, for small $qR_g < 1$ we have

---

[7] $\sin \mathrm{qr} / \mathrm{qr} \sim 1 - (\mathrm{qr})^3 / 3!$

$$S(q) \approx 1 - \frac{1}{3} q^2 R_g^2. \tag{3.27}$$

Equation (3.27) is often called the Guinier equation which is valid for $qR_g < 1$. Guinier analysis is independent of the form of the structure factor; this analysis allows for the measurements of the aggregate size regardless of the refractive index of the aggregate. In Eq. (3.27), $S(q)$ is normalized so that $S(0) = 1$.

One can determine the (average) radius of gyration of an ensemble of aggregates by plotting the inverse normalized scatterer intensity versus q^2. The plot should be linear, with a slope equal to $R_g^2 / 3$. This approximation is only true for $qR_g < 1$.

3.5.4.2 The Fractal Regime: $qR_g > 1$

In order to obtain the structure factor for the large qR_g, one needs to use an exact form of the density autocorrelation function (Sorensen 2001) which is

$$g(r) = A r^{D_f - d} h(r/\xi), \tag{3.28}$$

In Eq. (3.28), A is a normalization constant, d is the spatial dimension and ξ is a characteristic size representing the size of the aggregate, i.e., $\xi \approx R_g$. The $r^{D_f - d}$ term is characteristic of a fractal. The $h(r/\xi)$ is the cutoff function describing the perimeter of the aggregate and is independent of the fractal nature. It is suggested by Sorensen et al. (Sorensen et al 1992) that structure factors derived from autocorrelation function with roughly Gaussian cutoffs (i.e., $\beta = 2$) gave the best fit to their data when the effect of the aggregate polydispersity was included

$$h(r/\xi) = e^{-(r/\xi)^{\beta}}. \tag{3.29}$$

The explicit form of the structure factor can be determined by analytically Fourier transform Eq. (3.28) with (3.29)(Sorensen et al 1992) that is

$$S(q) = e^{-(qR_g)^2/D_f}\,{}_1F_1\left(\frac{3-D_f}{2}, \frac{3}{2}; \frac{(qR_g)^2}{D_f}\right), \tag{3.30}$$

where ${}_1F_1$ is the confluent hypergeometric series (Kummer function) (Sorensen et al 1992) and

$$\xi^2 = \frac{4}{D_f} R_g^2. \tag{3.31}$$

Equation (3.30) can be simplified for $qR_g >> 1$ to

$$S(q) = C(qR_g)^{-D_f}, \tag{3.32}$$

where

$$C = D_f^{\,D_f/2} \frac{\Gamma(3/2)}{\Gamma\left(\frac{3-D_f}{2}\right)}, \tag{3.33}$$

and Γ is the gamma function.

In order to determine the fractal dimension, one can fit Eq. (3.32) to the experimental data by constraining the fit to $qR_g \geq 5$ (Sorensen et al 1992, Sorensen & Wang 1999). It is found that in Eq. (3.32), $C = 1.0 \pm 0.05$ is the best value to describes the power law regime of the structure factor of a single aggregate with D_f in the range 1.7-2.2 (Sorensen 2001). However, one should be aware of the effects of polydispersity on the structure factor, especially in the large qR_g regime, and hence the value of the power law's coefficient.

Another popular expression for the structure factor is the Fisher-Burford form

$$S(q) = (1 + \frac{2}{3D_f} q^2 R_g^2)^{-D_f/2}. \quad (3.34)$$

Fisher-Burford form is a good approximation near $D_f = 2$, and its great advantage is its simplicity. It is also found that if the effects of polydispersity were not included, i.e., if the experimental data were fit with the single cluster structure factors, the best fit were obtained with the exponential (i.e., $\beta = 1$ in Eq. (3.29)) and Fisher-Burford forms. This fit, however, cannot be correct because real systems are polydisperse (Sorensen et al 1992).

3.6 Multiple Scattering Effects

Multiple scattering can affect the polarization and angular dependency of the scattered light (Lattuada et al 2001, Sorensen 2001, Urban & Schurtenberger 1998). Therefore, it is important to be aware of how multiple scattering can affect light scattering measurements, how to detect it, and how one can possibly avoid it. Multiple scattering can become significant for systems with a strong index of refraction contrast, high volume fraction or both.

Previous work has shown that multiple scattering can affect the scattered intensity measurements as the concentration of the dispersed particles in the solution increases for the same optical path length (i.e., determined by either the thickness of the cell or the detector field of view) (Urban & Schurtenberger 1998) or the optical path length increases for the same particle concentration (Lattuada et al 2001).

Here we show that the effect of multiple scattering on scattered intensity as a function of q (or θ) is described by a single parameter $< s >$, i.e., the average number of scattering events per photon along the length of the scattering volume(Mokhtari et al 2005). We show that

$< s >$ is equal to the product of the extinction turbidity and the optical path length of the medium; $< s >$ can be easily determined from a measurement of the transmittivity.

3.6.1 Light Extinction

Scattering is often accompanied by absorption. Both scattering and absorption remove energy from a beam of light as it traverses a particulate medium, and hence the beam is attenuated. If multiple scattering is negligible, and the particles are randomly positioned so that the intensity of scattering is simply an additive property of the number of particles (Kerker 1969), the intensity of a beam traversing a distance x through a medium is attenuated exponentially from I_o to I ,i.e.,

$$I/I_o = \exp(-\tau_{ext}\, x) = \exp(-n\,\sigma_{ext}\, x). \tag{3.35}$$

In Eq. (3.35), τ_{ext} is the extinction turbidity, n is the number of particles per unit volume, and σ_{ext} is the particle extinction cross section, i.e.,

$$\sigma_{ext} = \sigma_{abs} + \sigma_{sca}, \tag{3.36}$$

where σ_{abs} and σ_{sca} are the absorption and scattering cross sections (Bohren & Huffman 1983). Although scattering and absorption occur simultaneously, there are instances where one or the other dominates. For example, visible light passing through a fog is attenuated almost entirely by scattering, whereas light passing along the shaft of a coal mine might be attenuated primarily by absorption (Bohren & Huffman 1983). Equation (3.35) is usually referred to as the Lambert-Beer law (Monk 1937) although this law was empirically found for the absorption of a medium.

Equation (3.35) can be derived from two complimentary points of view that we will refer to as the "extinction cross section approach" and the "statistical approach." Below we use each approach to derive Eq. (3.35); we then compare the results to find the photon mean free path in terms of the scattering cross section and the particle number density.

3.6.1.1 Extinction Cross Section Approach

Envision a volume with differential thickness dx and area A hence volume $V = Adx$. Include in this volume N particles with extinction cross-section σ_{ext}. Light incident on this volume, perpendicular to A, parallel to dx, has intensity I. The length dx can be made small enough so that none of the particles falls in the extinction shadow of any other. Then the small amount of intensity lost as the light passes through this volume is

$$dI = -I\frac{N\sigma}{A}. \tag{3.37}$$

Each side of Eq. (3.37) can be divided by dx. On the right hand side use is made of $V = Adx$ and the particle number density $n = N/V$. The resulting differential equation yields

$$I(x) = I(0)\exp(-n\,\sigma_{ext}\,x). \tag{3.38}$$

The simple derivation above does not include the wave nature of light. One can derive Eq. (3.38) starting directly from Maxwell's equations assuming that the spherically symmetric particles dispersed in the medium are "independent scatterers" and are made of an optically isotropic material (Mishchenko 2002, Mishchenko et al 2004). Mishchenko et al. have presented a detailed analysis of the concept of the "independent scatterers" in their paper (Mishchenko et al 2004). As we mentioned earlier, independent scattering means that the scattered light by each particle is independent of the light scattered by all other particles in the system, and this is in accordance with having no coherent interference between the particles. In order to have independent scattering, the following assumptions should be satisfied:

(i) The distance from the observation point and the scatterer is much larger than any linear dimension of the scattering volume and the wavelength of the light.
(ii) Particle positions within the scattering volume are completely random during the time interval necessary to take a measurement.

(iii) The mean particle separation between the particles is at least several times larger than the radius of the particles. The linear dimension of the scattering volume is also much larger than the wavelength of the light.

(iv) The sum of the extinction cross sections of the particles filling the volume element is much smaller than the volume-element geometrical cross section.

3.6.1.2 Statistical Approach

Consider a long right volume (e.g., a right cylinder) of length x and cross sectional area A with a rate of photons per second, proportional to the light intensity $I(0)$, incident perpendicular to A. The medium inside the volume is turbid due to particles with an extinction cross section. At what rate, proportional to $I(x)$, do photons leave the other end of the volume?

We will make the assumption that the photons act like classical particles. We will also assume that the encounters of the photons with extincting particles in the volume is a Gaussian random process. For such a process, we can envision photons encountering an extincting particle, but then continuing along the same path to possible encounters with other particles. Therefore, the probability that a given photon has s encounters with extincting particles during its passage along the entire length x is given by the Poisson distribution[8], i.e., that

$$P(s) = \exp(- < s >) \frac{< s >^s}{s\,!} \cdot \tag{3.39}$$

In Eq.(3.39), $< s >$ is the average number of photon-particle encounters for an ensemble of photons. The average distance traveled between photon-particle encounters (i.e., the photon mean free path) is

$$l = x / < s > \cdot \tag{3.40}$$

[8] Poisson distribution, i.e., the limiting case of the Binomial distribution is a discrete probability distribution for rare independent events.

In the real turbid medium situation, only photons that have no encounters (i.e., $s = 0$) pass out of the far end of the volume. Thus, by Eq. (3.39)

$$P(0) = \exp(- < s >) \cdot \tag{3.41}$$

Then the light intensity passing through the volume, $I(x)$, is equal to this probability times the incident intensity, $I(0)$, to yield

$$I(x) = I(0) \exp(- < s >) \cdot \tag{3.42}$$

Both approaches yield the Lambert-Beer Law. Comparison connects the scattering variables to the statistical variables as:

$$< s >= n \sigma_{ext} x, \tag{3.43}$$

$$l = (n \sigma_{ext})^{-1}. \tag{3.44}$$

3.6.2 Measurements of the Effects of Multiple Scattering

In order to determine the effect of multiple scattering in light scattering measurements, we performed a set of experiments in which we varied the concentrations of the particulate medium as well as the optical path length of the cells. The experiments were performed with aqueous dispersions of polystyrene latex spheres with a diameter of 9.6 μm (7.4% coefficient of variance), obtained from Interfacial Dynamics Corporation. The refractive index of polystyrene particles does not have an imaginary part in the visible spectral region. Therefore, polystyrene particles are nonabsorbing, and the light extinction is due to scattering alone (i.e., $\sigma_{ext} = \sigma_{sca}$).

We used three quartz cells with different optical path lengths of 2 mm, 4.8 mm, and 10 mm. The small angle light scattering (SALS) experiments were performed with a vertically polarized argon-ion laser operating at a wavelength of $\lambda_o = 488\, nm$. The range of angles for the

SALS experiments, which is described in Chapter 5, was $0.9^o \le \theta \le 11.1^o$ corresponding to wave vectors of $2.1\times10^3\, cm^{-1} \le q \le 2.5\times10^4\, cm^{-1}$.

We prepared six aqueous dispersions of polystyrene microspheres with different volume fractions, each increasing by a factor of two. The range of volume fractions was $5.4\times10^{-4} \le f_v \le 1.6\times10^{-2}$. Volume fraction is related to particle number density n by $f_v = 4\pi R^3 n/3$, where R is the radius of the spherical particle. The colloidal suspensions were transferred into each cell, and the scattered light intensity was measured versus the scattered angle. The background intensity was measured by filling the cell with distilled water before each set of runs; the background intensity was then subtracted from subsequent measurements of solutions.

The conditions of independent scattering (i.e., conditions (i) through (iv) above) for the different volume fractions of the polystyrene solutions were checked which were qualitatively satisfied. For our highest volume fraction, however, the mean particle separation was almost 6 times larger than the particle size; this was right on the edge of having independent scatterers.

We should note that a small ratio of mean particle separation to size will likely cause multiple scattering to occur along with a loss of independent scattering. However, multiple scattering also occurs when this ratio is large, and hence the scattering is independent if the scattering volume is sufficiently large. It is this later situation for which our results apply.

Figure 3.5 shows the experimental scattered intensities $I(q)$ versus q for the 2 mm optical path length cell at different volume fractions. The theoretical Mie-Lorentz scattering curve is also plotted which was created by using the BHMIE code integrated over a lognormal size distribution (Bohren & Huffman 1983). The parameters needed to input the code were the most probable radius R of the polystyrene particles (4.8 μm) and 7.4% coefficient of variation of the radius, the relative refractive index of the particles ($m = 1.196$), and the wavelength of light

(488 nm). All curves are normalized to one on the intensity scale at $q = 2.1 \times 10^3 \, cm^{-1}$, our smallest experimental q value.

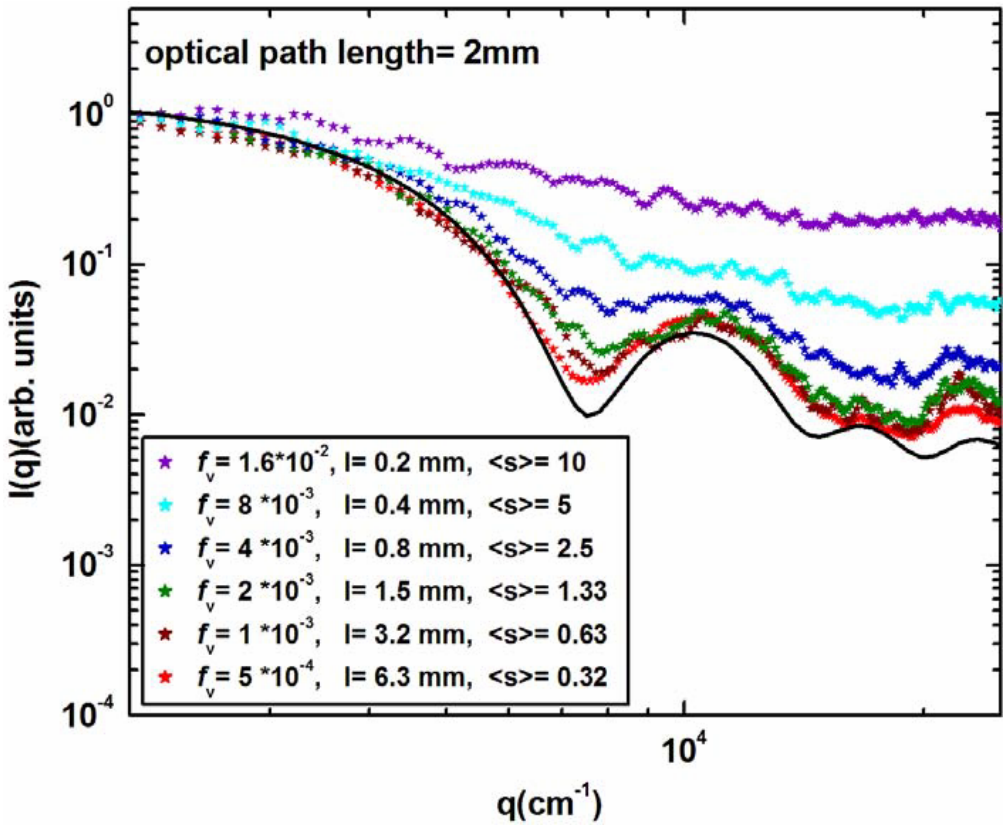

Figure 3.5 Normalized light scattering intensities (arbitrary units) plotted versus q at different volume fractions, f_v. The solid curve is the Mie-Lorentz scattering theory for 9.6 μm polystyrene with a geometric size dispersion of 7.4%. The optical path length of the cell is 2 mm. The photon mean free path l and the average number of scattering events $< s >$ are calculated for each concentration.

Figure 3.5 shows that for low volume fractions of polystyrene solutions, the scattered intensity is highly q (hence angle) dependent with the characteristic Mie-Lorentz ripples and mimics the theoretical calculation. As the volume fraction of the colloidal solution increases, the scattered intensity becomes more isotropic and loses its q dependence due to multiple scattering

effects (Lattuada et al 2001, Urban & Schurtenberger 1998). The results were similar for the cells with 4.8 mm and 10 mm optical path lengths.

The average number of scattering events $< s >$ (see Eq. (3.43)) and the photon mean free path for different volume fractions (see Eq. (3.44)) are also calculated and given in Fig. 3.5; this requires the total scattering cross section which can be obtained theoretically from BHMIE. The calculated optical cross section was $2.03\pi R^2$. Both the theory and the results shown in Fig. 3.5 suggest that the simple fundamental parameter to describe the extent of multiple scattering is the ratio of the path length divided by the photon mean free path (i.e., the average number of scattering events $< s >= x/l$). This is demonstrated in Figs. 3.6a, b, and c where the light scattering data with similar $< s >$ but different volume fractions and optical path lengths are plotted together (ca. 0.7±0.06, 2.8±0.4, and 12.4±0.3, respectively). The graphs are again normalized to one on the intensity scale at $q = 2.1 \times 10^3 cm^{-1}$.

Figure 3.6 shows that the graphs with similar $< s >$ overlap and show similar behavior. This supports our contention that the average number of scattering events is the universal parameter to describe the extent of multiple scattering. This extent can be quantified with the Poisson statistics of Eq. (3.39). For example, $P(2)/P(1) = < s > /2$ would be the relative ratio of double scattering to single scattering. Fortunately the value of $< s >$ can be obtained by either calculation or measurement.

In order to measure $< s >$, one needs to measure the relative amounts of incident and transmitted light, a ratio often called the transmittivity, to obtain $< s >= \ln[I(0)/I(x)]$. However, we should note that extinction is easy to measure in principle but may be difficult in practice, especially for large particles where it becomes difficult to discriminate between incident and forward-scattered light (Bohren & Huffman 1983). There are various techniques to directly measure the absorption or the extinction (Bohren & Huffman 1983). We used a photomultiplier to measure the transmittivity of the sample. The agreement between the theoretical and experimental value of $< s >$ had an error up to 20%.

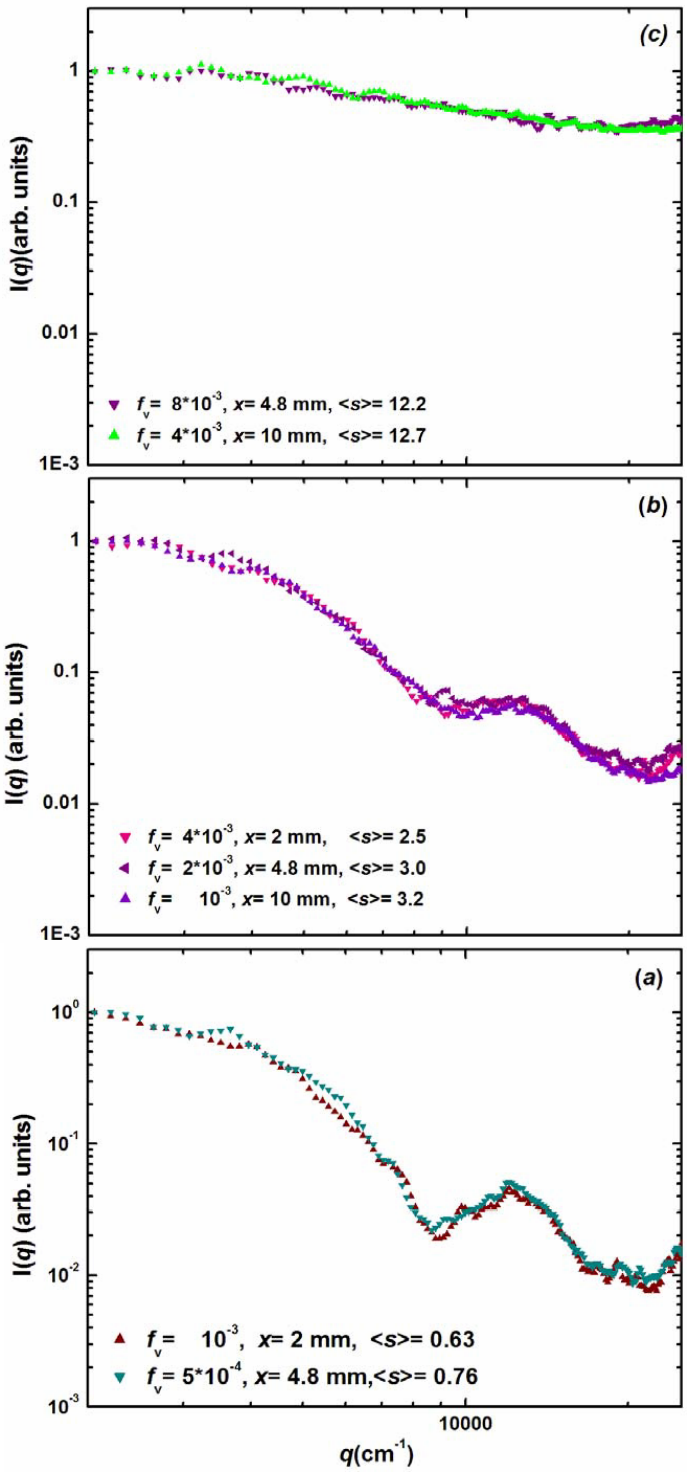

Figure 3.6 Normalized light scattering intensity (arbitrary units) plotted versus q for different $< s >$ that is the average number of photon-particle encounters. x is the optical path length of the cells. $< s >$ in Fig. 3.6a, 3.6b and 3.6c is 0.7 ± 0.06, 2.8 ± 0.4 and 12.4 ± 0.3, respectively.

3.7 Dynamic Light Scattering

Time dependent correlation functions have been familiar for a long time in the theory of noise and stochastic processes. Correlation functions provide a concise method for expressing the degree to which two dynamical properties are correlated over a period of time (Berne & Pecora 2000).

Dynamic Light Scattering (DLS), also known as Photon Correlation (PCS) or Quasi-Elastic Light Scattering Spectroscopy (QELS), is a technique used to obtain information about particles' movement. This technique is based on the measurements of the fluctuations in the scattered intensity within a given time with a monochromatic and coherent light source. The time dependence of the intensity will generally resemble a noise pattern (see the inset of Fig. 3.7). The scattered light by the particles (scatterers) can undergo either constructive or destructive interference; thus, within this intensity fluctuation, information is contained about particles' movements. The spectral measurements in dynamic light scattering is in the range of ca. 0.1 to 10^6 Hz. Hence particles in the range of a few angstroms to micron can be detected by this technique.

Let's consider Eq. (3.14) once again: if the particle moves a small distance relative to q^{-1}, there is no phase change. Whereas if the particle moves a large distance relative to q^{-1}, there is large phase change, and hence there are intensity fluctuations. The field correlation function $g^{(1)}(\tau)$ for a diffusing particle is

$$g^{(1)}(\tau) = < E(t)\,E(t+\tau) > / < E^2 >, \tag{3.45}$$

where $E(t)$ and $E(t+\tau)$ are the electric fields at time t and $t+\tau$, and $< ... >$ denotes statistical averages. The detector, however, can measure the scattered intensity rather than the electric field. Thus, the intensity correlation function $g^{(2)}(\tau)$ is defined as

$$g^{(2)}(\tau) = < I(t)\, I(t+\tau) > / < I^2 > . \tag{3.46}$$

The intensity autocorrelation function given in Eq. (3.46) is a stationary process meaning that the measurements can be performed at any time and yield the same results. Moreover, $g^{(2)}(\tau)$ should be measured over a sufficiently long time compared with the period of fluctuation to yield reliable information about the dynamical properties about the system. The autocorrelation function $g^{(2)}(\tau)$ is a measure of the similarity between two noise signals $I(t)$ and $I(t+\tau)$. When $\tau = 0$ these two signals are completely in phase with each other, and $< I(t)I(t+\tau) >$ is large; as τ increases, $I(t)$ and $I(t+\tau)$ get out of phase with one another, and the autocorrelation function $< I(t)I(t+\tau) >$ is small (Berne & Pecora 2000). Thus, it would appear that the autocorrelation function either remains equal to its initial value for all times τ, in which case the intensity I is a constant of the motion, or decays from its initial value which is a maximum (Berne & Pecora 2000)

$$< I(t)^2 > \; \geq \; < I(t)\, I(t+\tau) > . \tag{3.47}$$

For large times compared to the characteristic time for the fluctuation of Intensity, $I(t)$ and $I(t+\tau)$ are expected to become totally uncorrelated (Berne & Pecora 2000); thus,

$$\lim_{T\to\infty} < I(t)\, I(t+\tau) > = < I(t) >< I(t+\tau) > = < I >^2 . \tag{3.48}$$

Therefore, the intensity autocorrelation function decays from $< I^2 >$ to $< I >^2$ (i.e., the background or the noise level). This is shown in Fig. 3.7 where t is set to zero. The inset of Fig. 3.7 shows the time dependence of the scattered intensity which generally resembles a noise pattern.

The Siegart equation (Brown 1993) relates the second order autocorrelation function, Eq. (3.46), with the first order autocorrelation function, Eq. (3.45).

$$g^{(2)}(\tau) = B(1 + \beta \mid g^{(1)}(\tau) \mid^2), \tag{3.49}$$

where B is the baseline, and β is the coherence factor which is an adjustable parameter in the data analysis procedure.

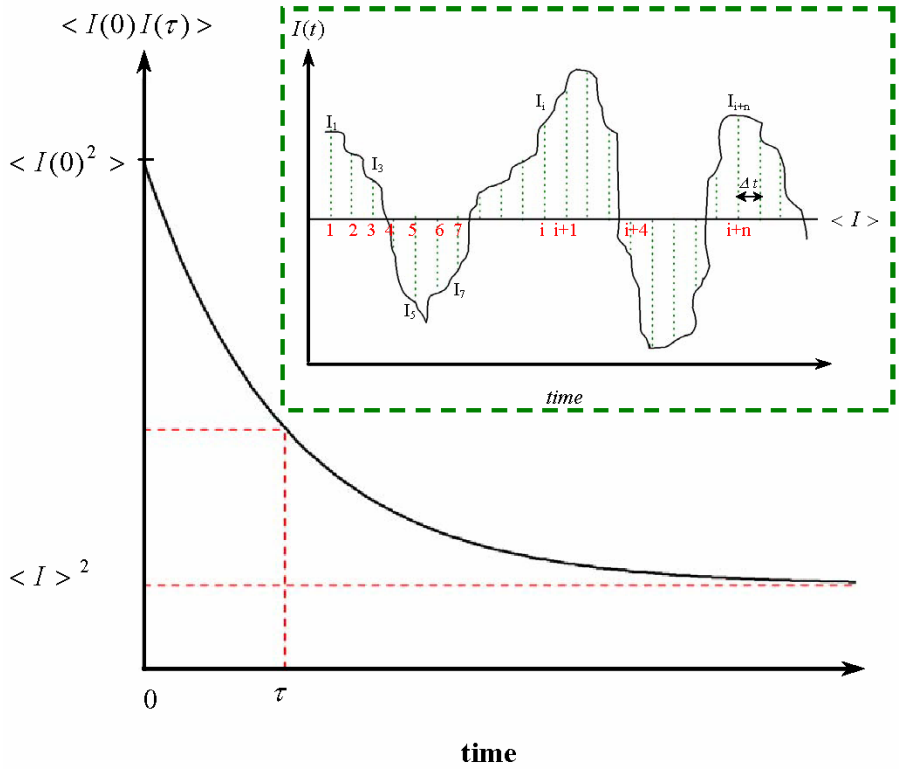

Figure 3.7 The time correlation function $< I(0)I(\tau) >$ versus time is plotted. $< I(0)I(\tau) >$ decays initially from $< I(0)^2 >$ to $< I >^2$ for times large compared to the correlation time. The inset graph shows the intensity fluctuations (noise pattern) in times. The time axis is divided into discrete time intervals Δt.

For the Siegart equation to be valid, the scattered electric field must be a Gaussian process (Brown 1993). The Siegart equation is violated for cases such as experiments with a small number of particles in the scattering volume, experiments with strongly interacting particles, and scattering from non-ergodic systems such as gels glasses where the time averaged

intensity correlation function of scattered light is different from the ensemble averaged function (Brown 1993).

For monodisperse particles, $g^{(2)}(\tau)$ is an exponential decay function, i.e.,

$$g^{(2)}(\tau) =< I >^2 +(< I^2 > - < I >^2) \exp(-\tau / \tau_c), \tag{3.50}$$

where τ_c is the correlation time of the diffusing particle in the solution. For spherical particles the correlation time is related to the size of particles by

$$\tau_c = \frac{1}{2Dq^2}, \tag{3.51}$$

where D denotes the translational diffusion coefficient

$$\mathrm{D} = \frac{\mathrm{k_B T}}{3\pi\eta \mathrm{d}}. \tag{3.52}$$

In Eq. (3.52), η is the viscosity of the solvent, d is the average diameter of the particles, k_B is the Boltzmann constant, and T (K) is the temperature of the solution. Thus, by meausuring the autocorrelation function $g^{(2)}(\tau)$ and fitting it with Eq. (3.50), the correlation time, and consequently, the particle size can be found. Here we only presented the simplest form; however, the autocorrelation function can have various forms depending on the shape of the particles, polydispersity, absorption, and other parameters (Berne & Pecora 2000, Brown 1993).

In dynamic light scattering, the fluctuation in the intensity can be measured via homodyne (self-beating) or heterodyne techniques. In the heterodyne technique, which is much less used in practice, it is the field correlation function, $g^{(1)}(\tau)$, that is measured. This technique involves optical mixing of the scattered light with a ca. 100 times more intense local oscillator (e.g., wall glare) (Brown 1993). The field autocorrelation function can also be obtained from the

intensity autocorrelation function (Siegart equation). In the homodyne technique, the intensity autocorrelation function is measured via the scattering from the sample.

CHAPTER 4 Colloidal Aggregation and Gelation

4.1 Colloids

Colloid particles dispersed in liquids exhibit astonishing properties. Dispersions such as the colloidal gold sol prepared by Faraday (1791-1867) over a century ago can persist almost indefinitely, yet the addition of salt would cause fast, irreversible aggregation (Russel et al 1999). The term *colloid* was coined by Thomas Graham (1861) for *glue-like* materials which appeared to consist of only one phase when viewed under the microscope (Evans & Wennerström 1999, Goodwin 2004).

Colloidal systems consist of at least two phases and the dimension of the dispersed phase generally ranges from 1 nm to 10 μm (Goodwin 2004, Russel et al 1999). If we consider the three states of matter (i.e., gas, liquid, and solid), we can observe the colloidal systems in all possible combinations except the two gas phases which will mix on a molecular level and do not form a colloidal system. Various types of colloidal systems with some examples are demonstrated in Table 1.

The partial list given in Table 4.1 makes the importance of colloidal systems seem almost self-evident. Nearly all industrial processes involve colloidal systems, and our ability to understand, use, and control colloids depend on our mastery of their properties (Evans & Wennerström 1999).

Table 4.1 Types of colloidal dispersion with some examples

Dispersed phase				
Dispersion medium		Gas	Liquid	Solid
	Gas	N/A	Aerosol (Fogs, liquid sprays)	Aerosol (Dust, smokes)
	Liquid	Foam (Fire extinguishers)	Emulsion (Drug delivery, milk)	Colloidal sol (Cement, paint, cosmetics)
	Solid	Solid foam (Styrofoam, zeolites)	Porous material (High impact plastics)	Solid suspension (Composites)

Colloids are traditionally divided into two classes called *lyophilic* ('solvent loving') and *lyophobic* ('solvent hating') whose general behaviors are entirely different from one another (Hunter 1994). When water is the medium or solvent, the terms *hydrophilic* or *hydrophobic* are often used (Hiemenz 1986).

Lyophilic colloids can be dispersed merely by adding a suitable solvent (i.e., a dispersing medium) to the dry colloid (e.g. gelatin or micelles). Typical for lyophilic colloids are, for example, the swelling phenomena illustrating the great affinity between the gelatin and the water molecules (Verwey & Overbeek 1947). Lyophobic colloids, on the other hand, cannot be formed by spontaneous dispersion in the medium. Examples of lyophobic colloids are colloidal gold solutions or latex dispersions. The lyophilic and lyophobic solutions can also be distinguished based on the reversibility or irreversibility of the system (Verwey & Overbeek 1947). For example, a dry gelatin when brought into contact with water is converted spontaneously into an apparently homogenous gel, or, if the amount of water is sufficient and the temperature is not too low, into a stable colloidal solution (Verwey & Overbeek 1947). However, a gold crystal brought into contact with water will never generate a colloidal gold solution (Verwey & Overbeek 1947).

Before we proceed further, the term "stability" of a colloidal dispersion needs to be defined. For example, a colloidal solution can be relatively stable with respect to aggregation, and yet unstable with respect to sedimentation, or vice versa. In this work we use the definition given by Verwey and Overbeek that "a colloidal dispersion is *stable* in which the particles retain their individual independence." Similarly, a system is called *unstable* in which the particles adhere together (Verwey & Overbeek 1947). Therefore, by the definition given above, the sedimentation of a colloidal solution is not considered to be unstable, or similarly, a gelatin gel is not a *stable* system, although it is *thermodynamically* stable (i.e., the solution has a lower Gibbs free energy than the separated components) (Hunter 1994).

Colloidal particles in a dispersed medium are always subjected to Brownian motion which results in collisions between them. Stability and other characteristics of a colloidal dispersion[9] are therefore determined by the nature of interactions between the particles during such collisions (Somasundaran et al 1997). The aim of this chapter is not to give a brief, yet comprehensive description of different kinds of stability, thus we only present a brief, general overview of this subject, inasmuch as it is necessary for the understanding of the colloidal aggregation. There are at least two mechanisms to stabilize colloidal dispersions

(i) Electrostatic stabilization
(ii) Steric stabilization

4.1.1 Electrostatic Stabilization

Electrostatics stabilization is the result of the presence of *electrical double layers* which, on approach of particles, interact, leading to repulsion. Competition between *attractive van der Waals-Hamaker* and repulsive double-layer forces determines the stability or instability of many colloidal systems which forms the basis of theory of colloid stability due to Derjaguin-Landau-Verwey-Overbeek (DLVO theory) (Evans & Wennerström 1999, Tadros 2007).

[9] Hereafter in this chapter, we only discuss the stability or aggregation of "lyophobic" colloids.

In a colloidal dispersion, several processes can be visualized to account for charging suspended particles such as dissociation of surface groups (e.g., OH, COOH) and adsorption of certain ionic species (such as surfactants) (Tadros 2007). In all cases charge separation takes place with some of the specifically adsorbed ions at the surface forming a surface charge which is compensated with unequal distribution of counter and co-ions (Tadros 2007). This is the basis of the diffuse double layer due to Gouy and Chapman which was later modified by Stern (Tadros 2007). The double layer is illustrated schematically in Fig. 4.1.

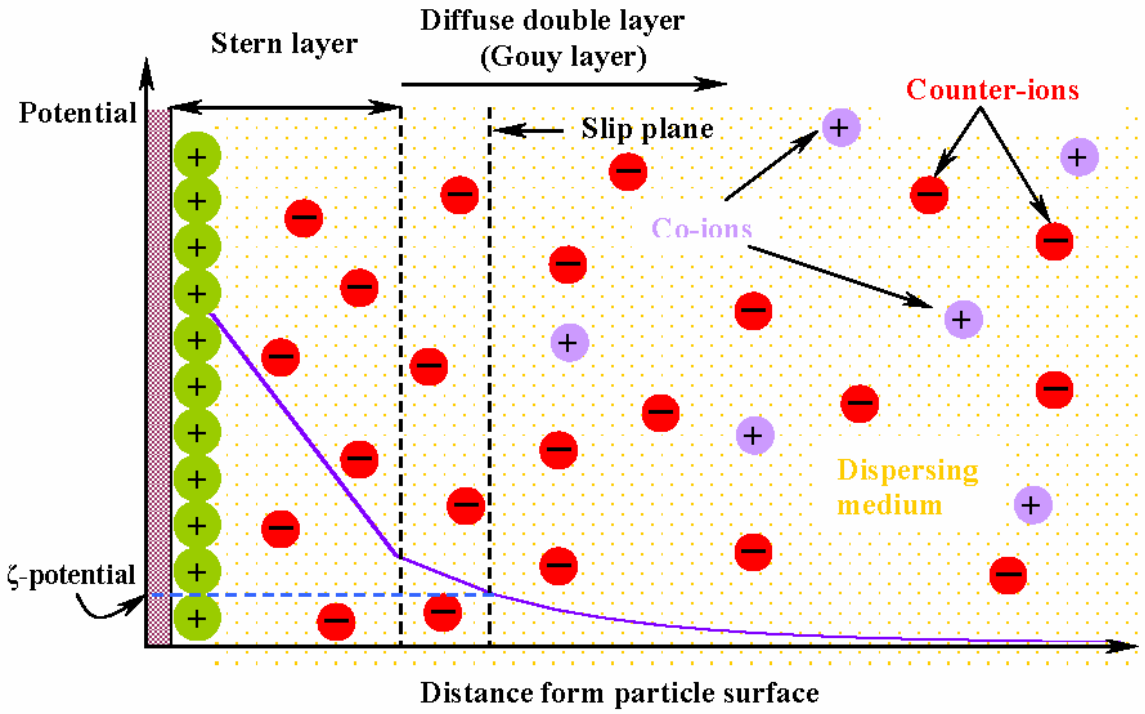

Figure 4.1 A Schematic representation of the electrical double layer (i.e., not drawn to scale). The surface charge on the particle is assumed to be positive. The schematic graph demonstrates the repulsion potential versus distance from the particle. The potential drops linearly through the Stern layer and decays exponentially in the diffuse double layer.

As shown schematically by the graph in Fig. 4.1, the potential drops linearly through the inner, compact layer (i.e., the Stern layer) and then exponentially decays in the outer diffuse later Gouy (or Gouy-Chapman) layer. The zeta (ζ) potential (or electrokinetic), which is a measurable

quantity, is the potential at the *slip plane* or *plane of shear*[10] (Hunter 1994, Tadros 2007). In general, the ζ-potential is smaller than the Stern potential because of the screening effect of the counterions within the slip plane.

The extension of the double layer, referred to as diffuse double-layer thickness or Debye length, depends solely on the properties of the liquid and not on any property of the surface such as its charge or potential (Israelachvili 2006). The Debye length increases with decrease in electrolyte concentration and decrease in the valency of the ions. The Debye length, λ_D of aqueous solutions at 25°C is given below (Israelachvili 2006).

$$\lambda_D = \left\{ \begin{array}{ll} 0.304/\sqrt{[\,\mathrm{NaCl}\,]}\ \mathrm{nm} & \text{for } 1:1 \textit{ electrolytes } (\text{e.g., NaCl}) \\ 0.176/\sqrt{[\,\mathrm{CaCl_2}\,]}\ \mathrm{nm} & \text{for } 2:1 \text{ and } 1:2 \text{ electrolytes} \\ & (\text{e.g., } \mathrm{CaCl_2} \text{ and } \mathrm{Na_2SO_4}) \\ 0.152/\sqrt{[\,\mathrm{MgSO_4}\,]}\ \mathrm{nm} & \text{for } 2:2 \text{ electrolytes } (\text{e.g., } \mathrm{MgSO_4}) \end{array} \right\} \quad (4.1)$$

where […] denotes the concentration of the salt solutions in molar (M).

4.1.1.1. Double Layer Repulsion

The origin of the repulsive forces between two similarly charged particles in a solvent containing counter-ions and electrolyte ions is, in fact, entropic (osmotic) and not electrostatic (Israelachvili 2006). In general, what maintains the diffuse double layer is the repulsive osmotic pressure between the counter-ions which forces them away from the surface and from each other so as to increase their configurational entropy. On bringing two such particles together one is therefore forcing the counter-ions back onto the surfaces against their preferred equilibrium state, i.e., against their osmotic repulsion, but favored by the electrostatic interaction. The osmotic pressure dominates the electrostatic interactions, and hence the net force is repulsive (Israelachvili 2006).

---

[10] The shear plane separates the region of fluid that moves with the particle from the region that flows freely when an electric field is applied in order to measure the ζ-potential (Hunter)

The electrostatic energy, $V_R(x)$ of the repulsion between two particles of diameter σ and a center-to-center distance of separation r is given by the following expression (Victor & Hansen 1984):

$$V_R(x) = J\frac{e^{-\kappa(x-1)}}{x}, \tag{4.2}$$

where $x = r/\sigma$ is the reduced distance between the centers of two particles, $\kappa = \sigma/\lambda_D$ is the reduced inverse Debye length, and J is the electrostatic coupling constant related to the surface or ζ-potential ψ_o via

$$J = \pi\varepsilon_o\varepsilon\sigma\psi_0^2. \tag{4.3}$$

In Eq. (4.3), ε_o is the permittivity of free space (i.e., 8.85×10^{-12} $C^2/N.m^2$), and ε is the relative permittivity (e.g., for water $\varepsilon = 78.5$).

4.1.1.2 Van der Waals-Hamaker (Dispersion) Attraction

The van der Waals-Hamaker (dispersion) energy is always an attraction energy between particles of the *same*[11] kind which may be considered to consist of three contributions: dipole-dipole (Keesom), dipole-induced dipole (Debye) and London or dispersion interactions (Tadros 2007).

For colloidal particles, which are assemblies of atoms or molecules, only the London (dispersion) interactions have to be considered because large assemblies have no net dipole moment or polarization (Tadros 2007). The London interaction arises from charge fluctuations within an atom or molecule which is associated with the motion of its electrons. The dispersion

[11] The van der Waals-Hamaker interaction between two different materials immersed in a liquid medium can be repulsive (Hirtzel, 1985).

energy of attraction between two identical spheres of diameter σ, at a distance r (i.e., center-to-center) in vacuum, is given by

$$V_A(x) = -\frac{A_H}{12} h(x), \tag{4.5}$$

where A_H is the Hamaker constant, and

$$h(x) = \frac{1}{x^2 - 1} + \frac{1}{x^2} + 2\ln\left(1 - \frac{1}{x^2}\right). \tag{4.6}$$

The Hamaker constant is determined by the nature of the particles and that of the surrounding medium (Israelachvili 2006). The Hamaker constant in water ranges from $\leq 1\ k_B T$ for some hydrocarbon to $\geq 100\ k_B T$ for metals, where k_B is the Boltzmann's constant, and T is the absolute temperature. For example, the Hamaker constant of polystyrene in water is $A_H = 1.3 \times 10^{-20}$ J or 3.16 $k_B T$ (Russel et al 1999).

4.1.1.3 DLVO Theory

The interaction between colloidal particles is modeled by the DLVO potential, which is the sum of the screened electrostatic repulsion between their double-layers and of the van der Waals-Hamaker attraction given in Eqs. (4.2) and (4.5), respectively.

$$V_T = V_A + V_R \tag{4.7}$$

A schematic representation of the variations of V_A, V_R, and V_T with x is plotted in Fig. 4.2.

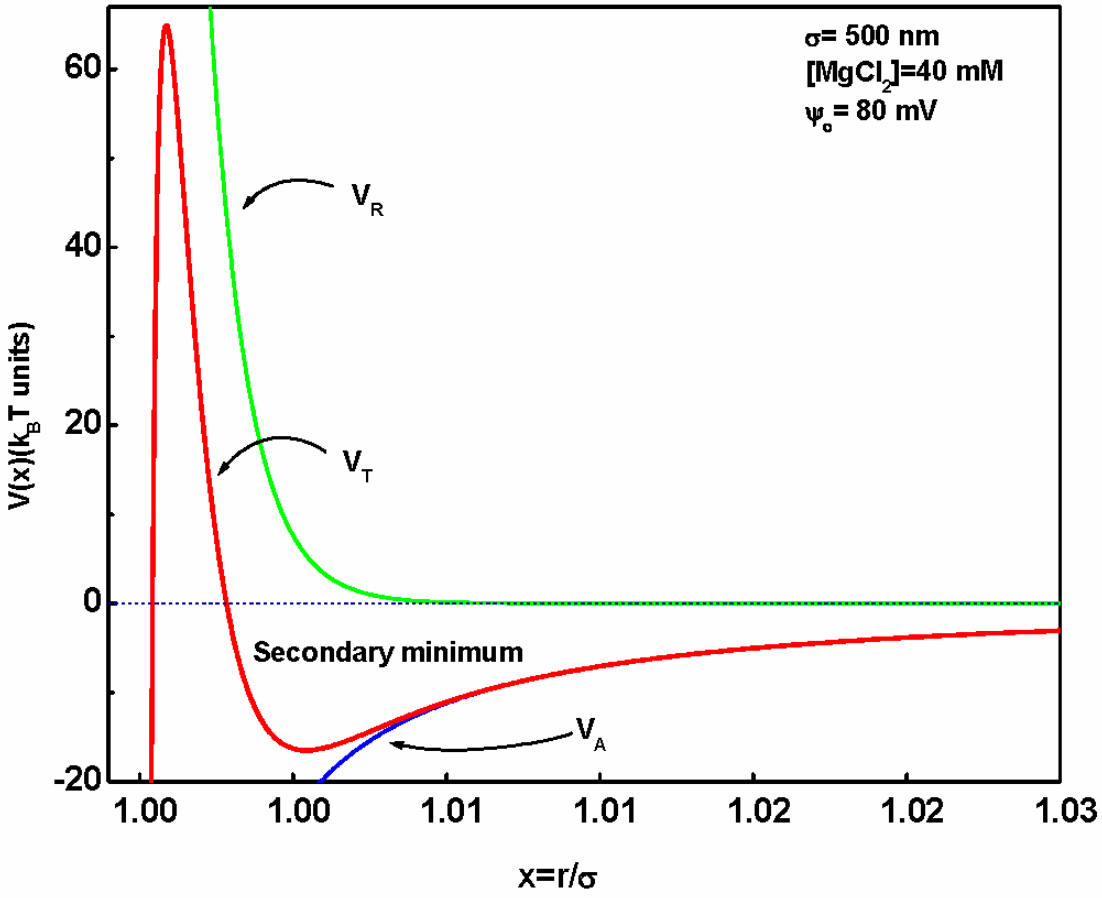

Figure 4.2 The van der Waals-Hamaker V_A, the double layer potential V_R, and the total potential energy V_T are plotted versus x (i.e., $x = r/\sigma$). The potential curves are plotted in k_BT units. The particle size is 500 nm, the salt molarity is 40 mM, and the ζ-potential is 80 mV.

As can be seen in Fig. 4.2, V_R shows an exponential decay with increase in x, approaching zero at large x, whereas V_A does not decay to zero at large x. The V_T curve shows two minima and one maximum. Near the particle, there is a deep minimum in the potential energy produced by the van der Waals-Hamaker attraction that is referred to as the primary minimum. There is an energy barrier at intermediate distances which depends on the zeta potential and the electrolyte concentration and valency (e.g., when the electrolyte ions do not screen too much). Farther away, there is a shallow minimum at large x that is referred to as

secondary minimum. It has theoretically been shown (Victor & Hansen 1984) that in order to have the secondary minimum in the potential curve, the following condition should be satisfied

$$\frac{24J}{\kappa A_H} > 2.7. \tag{4.8}$$

The condition for the stability of colloidal dispersion is to have an energy barrier that is much larger than the thermal energy of the particles (Brinker & Scherer 1990, Tadros 2007). In general, the energy barrier should be greater than $10^{-25}\ k_B T$ (Brinker & Scherer 1990, Hiemenz 1986, Tadros 2007). This is achieved by having a high zeta potential larger than 30-50 mV (Brinker & Scherer 1990, Tadros 2007). The DLVO theory will be used again later in this chapter in order to explain different types of aggregation.

Finally, it is important to note that there are some situations that cannot be handled by the DLVO theory; some of these situations are given below (Peker 2007).

(i) High ionic strength
(ii) Heteroaggregation(e.g., dissimilar components in terms of shape, size, surface and other physical properties)
(iii) Discrete surface charges
(iv) Strong electrostatic interactions as in the case of multivalent counterions or low dielectric constant of the solvent
(v) Specific ion effects
(vi) Non-DLVO forces (such as steric, hydrophobic, depletion) and very short-range hydration forces

4.1.2 Steric Stabilization

In practice, there are many circumstances when a flexible method is needed to control the stability of a suspension. One of the most efficient ways to accomplish this is steric stabilization. Steric stabilization arises from the presence of adsorbed surfactant or polymer layers mostly of

the nonionic type which prevents the close approach of the particles; this is briefly explained below (Tadros 2007).

When two particles approach one another, the polymer-layers of neighboring particles (i.e., strongly adsorbed to the particles) begin to overlap or become compressed. This results in the reduction of the entropy of the chains in the interaction region. At the same time, the solvent molecules that surround the polymer chains are also "squeezed" out from between the particles which would increase the free energy of the system. As a result, an osmotic pressure is created in the overlap region which would cause the particles to repel one another and result in a *thermodynamically* stable dispersion (Brinker & Scherer 1990, Hirtzel & Rajagopalan 1985). In order to have an effective steric barrier, there are a number of conditions that need to be satisfied (Brinker & Scherer 1990, Tadros 2007):

(i) The surface of the particle should be completely covered to prevent polymer chains from attaching to both particles which is causing the *bridging flocculation.*
(ii) The polymer should be strongly adsorbed (or 'anchored') to the particle surface so that it cannot be displaced during the Brownian collisions. The lack of this criterion would result in *depletion flocculation*.
(iii) The adsorbed layer thickness should be sufficiently large enough (typically > 5 nm) to keep the point of closest approach outside the range of the attractive van der Waals-Hamaker forces. Otherwise, weak flocculation (i.e., reversible) occurs when the adsorbed layer thickness is smaller than 5 nm.
(iv) The non-anchored portion of the polymer should be highly soluble in the medium and strongly solvated by its molecules. Whereas, strong flocculation (i.e., irreversible) occurs when the solvency of the medium for the stabilizing chains becomes poor.

If the condition (ii) (i.e., given above) is not satisfied, depletion flocculation can occur. Depletion flocculation can be achieved by addition of 'free', *non-adsorbing* polymer to a dispersion (Tadros 2007). The free polymer cannot approach the particle surface by a distance equal to twice the radius of gyration (see 4.3.1) of the polymer because when the polymer coils approach the surface, they loose entropy and this loss is not compensated by an adsorption

energy. Hence the particles will be surrounded by a depletion zone with thickness δ (free of polymer) (Tadros 2007). Now, when two particles approach one another to a distance less than 2δ, the depletion zones of the two particles will overlap. At and above a *critical volume fraction* of the free polymer, the polymer become "squeezed" out from between the particles, and hence the osmotic pressure outside the particle surface becomes higher than in between them; this results in a weak flocculation which is referred to as depletion flocculation (Tadros 2007).

4.2 Colloidal Aggregation

Colloidal particles undergo Brownian motion due to their thermal energy and small sizes which can cause collisions between them. Collisions between particles may be caused not only by thermal motion but also by gravitational forces and by convective diffusion. The stability and other properties of colloidal dispersions depend on whether such collisions lead to aggregation (Sonntag & Strenge 1987).

Diffusion controlled processes (i.e., particle collisions arise solely from Brownian diffusion of particles) are usually referred to as perikinetic aggregation. If external energy is applied on the system, e.g., shear, ultrasound or centrifugal, or the system is not at thermal equilibrium (so that convection currents arise), then the rate of particle collisions is usually increased, and the aggregation is referred to as orthokinetic (Tadros 2007).

The aggregation[12] of colloidal particles can occur in the primary or secondary minimum of the DLVO potential energy (see Fig. 4.2). As a result, the aggregation may be irreversible or reversible, respectively. In order for the particles to undergo aggregation into the primary minimum, they need to overcome the energy barrier. The higher the energy barrier, the lower is the probability of aggregation. Hence one can consider the process of aggregation as a rate phenomenon which increases with reduction of the energy barrier and ultimately, in the absence of any barrier, it becomes very fast (Tadros 2007). On the other hand, if the secondary minimum

[12] In the literature, the term "aggregation" is also referred to as flocculation, agglomeration, and coagulation.

in the potential energy becomes deep enough (several $k_B T$ units), the system can weakly aggregate; this aggregation is reversible in nature, and some deaggregation may occur. The process of weak reversible aggregation may produce gels which on application of shear breakup, forming a sol. This process of sol-gel transformation produces thixotropy (i.e., reversible time dependence of viscosity) which can be applied in many industrial formulations, e.g., in paints (Tadros, 2007).

Irreversible aggregation of small particle to form large clusters is one of the most common phenomena which can be seen in nature and many areas of science and technology such as aerosol and colloidal science, polymer science, phase transitions and critical phenomena (Mitsugu 1989).

The aggregation processes can be classified variously of which one is shown in Fig. 4.3.

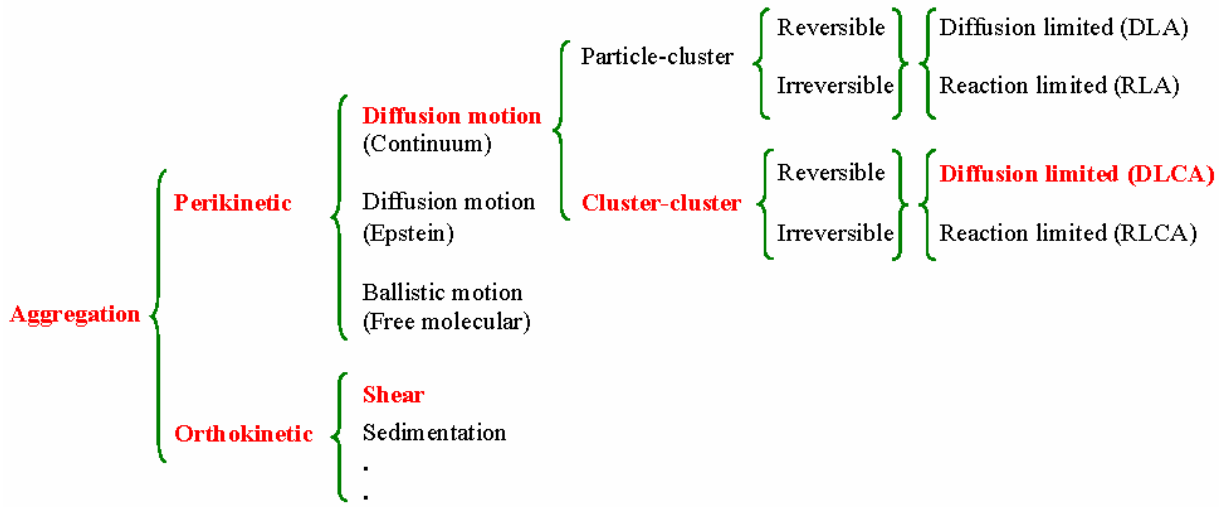

Figure 4.3 The classification of the aggregation processes of which the DLCA aggregation and shear-induced aggregation are discussed in this work.

4.2.1 Brownian Diffusion Aggregation

Diffusion-controlled processes can be classified based on the mechanisms by which the aggregation occurs which is particle-cluster aggregation or cluster-cluster aggregation. Furthermore, the aggregation kinetics can be either a diffusion-limited process or a reaction-limited mechanism. These mechanisms of aggregation are explained below.

In particle-cluster model, the aggregation mechanism starts from a seed particle, and the particles are added one after another on the aggregate. The Eden model (1961) is an example of this type of aggregation which has been mostly used to describe nonequilibrium biological processes, such as tumor expansion (Jullien & Botet 1987). Another model, which was associated mainly with aggregation of colloids in solution, was the DLA model (i.e., diffusion-limited aggregation) (Witten & Sander 1981). The DLA model can explain some of the aggregation processes such as electrodeposition, fluid displacement, and electrical breakdown (see Fig. 2.1c). However, this model was not able to describe most of the regular aggregation processes such as those encountered in colloids and aerosols. The Fractal dimension in Witten-Sander model in three dimension, i.e., $D_f = 2.5$, was too large to account for the experimental value which is generally 1.75 or slightly more, in colloids and aerosols (Jullien & Botet 1987).

In cluster-cluster aggregation model, unlike the particle-cluster aggregation model, the clusters are allowed to diffuse, collide, and stick together to form larger clusters (Kolb et al 1983, Meakin 1983). Cluster-cluster aggregation mechanism can be classified as

(i) Diffusion limited cluster-cluster aggregation (DLCA)
(ii) Reaction limited cluster-cluster aggregation (RLCA)
(iii) Ballistic limited cluster-cluster aggregation (BLCA)

In the DLCA regime, the height of the energy barrier is reduced to much less than $k_B T$, so that every collision will result in the particles sticking together (i.e. the sticking probability is one, $P_{stick} \sim 1$), leading to very fast aggregation. Hence the aggregation rate is limited only by the

diffusion (random walk) of the clusters. The fractal dimension of the aggregates formed via DLCA mechanism is $D_f = 1.75 \pm 0.05$ (Lin et al 1990c). Whereas in the RLCA regime, there is a repulsive energy barrier which is substantially larger than $k_B T$, but not insurmountable, and hence many collisions are required before two clusters actually stick. In this case, the aggregation rate is limited by the probability of overcoming the repulsive barrier $\phi_{\max}$ (i.e., $P_{stick} \sim \exp(-\phi_{\max} / k_B T) << 1$) leading to much slower aggregation. Here the diffusive motion of any two clusters gives them the opportunity to explore many more possible mutual bonding configurations, resulting in somewhat higher fractal dimension than that in DLCA regime, i.e., $D_f = 2.05 \pm 0.05$ (Lin et al 1989, Lin et al 1990b). Moreover, clusters produced under reaction-limited conditions are more polydisperse in size than their diffusion limited counterparts (Fry et al 2004).

The classical understanding of Brownian aggregation kinetics is given by the Smoluchowski theory (1917) which follows from the assumption that the collisions are binary and that fluctuations in density are sufficiently small so that the collisions occur at random (Sonntag 1993). For dilute dispersions with volume fractions less than 1%, only the binary collisions need to be considered, and the probability of three-particle collisions is small (Sonntag 1993).

The coagulation of two clusters of size (number of monomers) i and j is given by the following relation

$$i^{\text{th}} \text{ mer} + j^{\text{th}} \text{ mer} \xrightarrow{K_{ij}} (i+j)^{\text{th}} \text{ mer} = k^{\text{th}} \text{ mer}, \tag{4.9}$$

where K_{ij} is the aggregation kernel (or collision frequency factor). The aggregation kernel is a constant, independent of the particles concentration (number densities).

For Brownian aggregation, the collision rate, J, between two particles (or two aggregates) of radius a_i and a_j is

$$J_{ij} = K_{ij}\, n_i\, n_j, \tag{4.10}$$

where n_i and n_j are the corresponding number densities.

The conservation (or population balance) equation describing the temporal evolution of the cluster of size k is as follows

$$\frac{dn_k}{dt} = \frac{1}{2}\sum_{i+j=k} J_{ij} - \sum_{i=1}^{\infty} J_{ki}. \tag{4.11}$$

The first term on the right-hand side of Eq. (4.11) gives the rate of creation of clusters of size k by aggregation of two smaller clusters, and the second term gives the rate at which clusters of size k are eliminated by further aggregation (Drake 1972, Sonntag 1993).

The Smoluchowski equation is a *mean-field* analysis because it assumes that the probability of two clusters meeting is simply proportional to the product of their number densities, i.e., there are no spatial correlations between clusters (Fry et al 2002). For realistic collision models the aggregation kernel is found to be a time-independent homogeneous function of i and j, i.e.,

$$K(\alpha i, \alpha j) = \alpha^{\lambda} K(i, j) = \alpha^{\lambda} K(j, i), \tag{4.12}$$

where λ is the degree of homogeneity, and α is a constant.

It can be shown that the Brownian aggregation kernel K_{ij} is

$$K_{ij} = 4\pi (R_{ij})(D_{ij}), \tag{4.13}$$

where D_{ij} is the relative diffusion coefficient associated with the particles (or aggregates), and R_{ij} is the effective collision radius that is the distance at which the van der Waals-Hamaker attraction becomes dominant (Sonntag 1993).

For spherical particles R_{ij} equals the sum of the particle radii. In the continuum regime, the relative diffusion coefficient of two spherical particles of radii a_i and a_j is given by the Stokes-Einstein equation

$$D_i + D_j = \frac{k_B T}{6\pi\eta}\left(\frac{1}{a_i} + \frac{1}{a_j}\right), \tag{4.14}$$

where η is the viscosity of the medium. Therefore, the aggregation kernel for spherical symmetry equals

$$K_{ij} = \frac{2k_B T}{3\eta}\frac{(a_i + a_j)^2}{a_i a_j}. \tag{4.15}$$

Equation (4.15) can be simplified by assuming that collisions between particles (clusters) of approximately equal size dominate such that for $a_i = a_j$

$$(a_i + a_j)\left(\frac{1}{a_i} + \frac{1}{a_j}\right) = 4. \tag{4.16}$$

Therefore, the aggregation kernel[13] simplifies to

---

[13] Swift and Friedlander have stated that the agreement between the aggregation kernel found in an experiment (using polystyrene, 1.83 μm in diameter) was found to be approximately up to 60% of $8k_BT/3\eta$.

$$K_o = \frac{8k_B T}{3\eta}. \tag{4.17}$$

It is important to note that the aggregation kernel (given in Eq. (4.15)) for unequal spheres is larger than 4, and hence the aggregation rate increases with increasing polydispersity. However, it has been shown that Smoluchowski's approximation theory may be used with reasonable accuracy for initially monodisperse systems, and also for dispersions having low polydispersity initially (Sonntag & Strenge 1987).

Equations (4.10), (4.11), and (4.17) can be combined to yield the simplified Smoluchowski equation, i.e.,

$$\frac{dn_k}{dt} = \frac{4k_B T}{3\eta}\left(\sum_{i+j=k} n_i n_j - 2\sum_{i=1}^{\infty} n_k n_i\right). \tag{4.18}$$

The solution to Eq. (4.18) gives the following expression for the kinetics of the decay of the total particle concentration, n_c, i.e.,

$$n_c(t) = \frac{n_c(0)}{1 + (t/t_c)}, \tag{4.19}$$

where $n_c(0)$ is the initial particle concentration (i.e., $n_c(0) = n_m$, where n_m is the monomer number density) and t_c is given as

$$t_c = \frac{3\eta}{4n_m k_B T} = \frac{\pi\eta a^3}{f_v k_B T}, \tag{4.20}$$

where f_v is the volume fraction of the particles in the system. Equation (4.20) is referred to as the characteristic time ,that is, the time required for half of the original dispersed particles to aggregate.

In order to solve Eq. (4.11), Smoluchowski assumed that no repulsive barrier was present (i.e., fast aggregation). Fuchs (1934) then extended the theory formally, allowing the collision probability to depend on an arbitrary interaction potential and expressing the results in terms of the stability ratio, W_B (Hiemenz 1986), i.e.,

$$W_B = 2a \int_{2a}^{\infty} \exp(\frac{V(r)}{k_B T}) r^{-2} dr, \tag{4.21}$$

where $V(r)$ is the potential energy of interaction of the particles, r is the center-to-center distance between the particles, and a is the particle radius assuming that the particles have equal size (Hiemenz 1986). Therefore, the aggregation kernel for the fast aggregation corresponds to that for slow aggregation through the stability ratio given in Eq. (4.21), i.e.,

$$W_B = \frac{K_{ij}(\text{fast})}{K_{ij}(\text{slow})}. \tag{4.22}$$

An approximation relating W_B and the maximum potential barrier $\phi_{\max}$ is given for polystyrene particles as follows

$$W_B = W_\infty + 0.25[\exp(\frac{\phi_{\max}}{k_B T}) - 1], \tag{4.23}$$

where W_∞ is the stability ratio due to dispersion forces (van der Waals-Hamaker attraction) alone. In general, even at high ionic concentration, W_∞ differs from unity because of the finite range of the attraction and the hydrodynamic interactions omitted from Smoluchowski's calculation of the collision rate. The theoretical stability ratio W_∞, for fast aggregation of polystyrene particles in water, is found to range approximately between 1.7-2 for polystyrene particles ranging between $0 \le a \le 400$ nm (Russel et al 1999).

The theoretical stability ratio of an aqueous salt solution is related to the concentrations of the counter-ions c (i.e., in moles per liter) as follows

$$\log (W_B / W_\infty) = -K_1 \log c + K_2, \tag{4.24}$$

where K_1 and K_2 are constants. For water at $25^o C$, the value of K_1 has been calculated to be

$$K_1 = 2.15 \times 10^9 \ \psi_o^2 \ a / z^2, \tag{4.25}$$

where the proportionality constant (i.e., 2.15×10^9) has a unit of m^{-1}, a is the radius of the particle (i.e., mentioned earlier) , and ψ_o is given by

$$\psi_o = \frac{\exp(ze\psi_o / 2k_B T) - 1}{\exp(ze\psi_o / 2k_B T) + 1}, \tag{4.26}$$

z is the valency of the counter-ions, and ψ_o is the zeta potential (Hiemenz 1986).

Figure 4.4 shows a schematic plot of the stability ratio W_B / W_∞ versus the salt concentration. As can be seen in this figure, the plot is linear as required by Eq. (4.24) with a negative slope of K_1 at low salt concentrations. In theory, K_1, hence the slope depends on the particle size (Eq.(4.25)). However, Ottewill and Shaw showed that the measured stability ratio, for polystyrene particles ranging from 60 nm to 423 nm, varied little with the particle size (Ottewill & Shaw 1966). We should remind here that the horizontal asymptote at high salt concentration, where $W_B / W_\infty = 1$, corresponds to the fast aggregation (DLCA). Further, the region at lower salt concentration, where $W_B / W_\infty \sim W_B >> 1$, corresponds to the slow aggregation (RLCA).

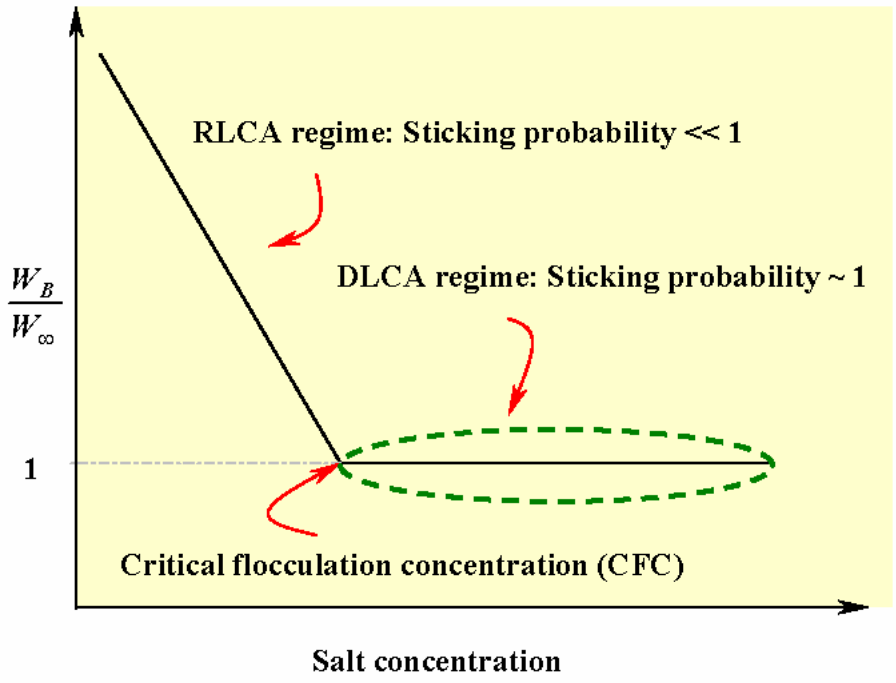

Figure 4.4 Schematic plot of stability ratio, W_B / W_∞ versus salt concentration. The horizontal asymptote at high salt concentrations corresponds to fast aggregation (e.g., DLCA). The region at lower salt concentration, where $W_B >> 1$ corresponds to slow aggregation (e.g., RLCA). The inflection point between these two regions is referred to as "critical flocculation concentration" (CFC).

The concentration at which $W_B / W_\infty = 1$ (where the break in the curve appears) measures the critical flocculation point (CFC) (or "critical coagulation concentration" CCC). For $W_B / W_\infty >> 1$, the slow aggregation regime has been observed for up to $W_B \sim 10^4$ (i.e., corresponding to $\phi_m \approx 15\ k_B T$). From this, one may conclude that the height of an energy barrier must be *at least* $15\ k_B T$ [14] to have any appreciable stability for a colloidal solution. Likewise, one can also assume that if the secondary minimum (see Fig. 4.2) is less than $15\ k_B T$, the

[14] The reported value of ϕ_m (i.e., minimum potential barrier required for the stability) is found to have some variation in the literature, e.g., 10 $k_B T$ (Brinker 1990), 15 $k_B T$ (Heimenz 1986), and 25 $k_B T$ (Tadros 2007).

particles will be able to "escape" from it (i.e., weak aggregation resulting in deaggregation) (Hiemenz 1986).

4.2.2 Shear Induced Aggregation

The aggregation of particles in a colloidal system can be controlled by three different mechanisms including perikinetic aggregation due to Brownian motion (dominant for particles with diameters smaller than 1 μm), shear-induced orthokinetic aggregation (dominant for particles in the range of 1-40 μm), and differential sedimentation aggregation (typically important for particles larger than 40 μm) (Wang et al 2005).

When colloidal particles are immersed in a shear field, aggregation is promoted by the fluid motion. Assuming that the (spherical) particles follow linear fluid streamlines of the unperturbed shear flow (i.e., no hydrodynamic, electrostatic, or van der Waals interaction), until they collide as if other particles did not exist, Smoluchowski derived the analytical solutions for the aggregation kernel in the laminar shear flow (Adachi 1995, Sonntag & Russel 1986).

In Smoluchowski's theory of shear-induced aggregation, Brownian diffusional effects are considered negligible and particle collisions result from a nonuniform macroscopic flow field applied to the dispersion. It should be reminded here that Smoluchowski's derivation of the Brownian aggregation, that was discussed earlier, was under the assumptions that particle collisions were solely from diffusion induced by Brownian motion and macroscopic convective effects were ignored (Feke & Schowalter 1985).

The aggregation rate J_{ij} between (homogeneous) spheres of radius a_i and a_j in a laminar shear field is given as

$$J_{ij} = \frac{4}{3}(a_i + a_j)^3 \gamma n_i n_j, \tag{4.27}$$

where γ is the shear rate (or strain rate) with dimensions of reciprocal time, and n_i and n_j are the number concentrations of the corresponding particles (Feke & Schowalter 1985). Smoluchowski then obtained an analytical solution for the change in total number of particles n in a system by assuming that $a_i + a_j = 2a_i$.

Similar to the Brownian aggregation theory, the conservation equation (population balance) is given as

$$\frac{dn_k}{dt} = \frac{1}{2}\sum_{i+j=k} J_{ij} - \sum_{i=1}^{\infty} J_{ki}. \tag{4.28}$$

Substitution of Eq. (4.27), the assumption of equal sized spherical particles in the system (i.e., $a_i + a_j = 2a_i = 2a$), and $f_v = (4/3)\pi a^3 n$ (i.e., volume fraction of the particles in the system) into Eq. (4.28) yields

$$\frac{dn}{dt} = -\frac{4\gamma f_v}{\pi} n. \tag{4.29}$$

Equation (4.29) shows that, unlike Brownian aggregation, the total number of particles decays exponentially. Also, the aggregation rate is independent of temperature and viscosity, unlike the case for Brownian aggregation which is sensitive to both. Moreover, this theory predicts that aggregation by shear flow becomes important as particle size increases (Swift & Friedlander 1964).

The characteristic time τ_s for shear aggregation can be determined using Eq. (4.29), i.e.,

$$\tau_s = \frac{\pi}{4\gamma f_v}. \tag{4.30}$$

For fractals the above equation must be considered for the effective volume fraction (i.e., the monomer volume fraction of an individual cluster) (Sonntag & Russel 1986).

In reality, the relative motion between colloidal particles immersed in a viscous liquid is hydrodynamically influenced by the presence of other particles, and later investigators included hydrodynamic interactions and colloidal forces by introducing the stability ratio W_s into Smoluchowski's equations (Adachi 1995, Feke & Schowalter 1985) such that

$$J_{ij} = \frac{4}{3}(a_i + a_j)^3 \frac{\gamma n_i n_j}{W_s}. \tag{4.31}$$

However, the Smoluchowski result given in Eq. (4.27) often provides a useful estimate of the actual aggregation rate given in Eq. (4.31) (Torres et al 1991a); in fact, Swift and Friedlander have confirmed the Smoluchowski's shear flow theory for shear rates ranging from 1-80 $\sec^{-1}$ (Swift & Friedlander 1964).

Shear-induced aggregation and Brownian aggregation are two mechanisms that exist simultaneously in sheared system. Swift and Friedlander have shown that these two aggregation mechanisms are independent over a wide range of conditions (Swift & Friedlander 1964). Therefore, the aggregation rate J (the subscripts ij are dropped to refer to equal-sized spheres) in a system undergoing both shear-induced aggregation and Brownian aggregation can be written as

$$J = \frac{8k_B T n^2}{3\eta W_B}[1 + \frac{4}{3\pi}\frac{W_B}{W_s} Pe], \tag{4.32}$$

where W_B is the stability ratio introduced into the Brownian aggregation due to the potential barrier in DLVO theory (see Eq. (4.21)), η is the solvent viscosity, and Pe is referred to as Péclet number, i.e.,

$$Pe = \frac{3\pi\eta \mathrm{a}^3 \gamma}{\mathrm{k_B T}}. \tag{4.33}$$

The Péclet number is a dimensionless quantity that reflects the relative importance of shear to Brownian diffusion in a sheared colloidal dispersion (Feke & Schowalter 1985, Swift & Friedlander 1964). Some care is necessary in using this quantity as different authors have used definitions that vary by the numerical constant of 3π (e.g., 6π) (Clarke et al 1995).

The Péclet number can also be defined as $Pe := \gamma \tau_B$, where τ_B is the time scale characteristic of the Brownian motion defined by $a^2 = 2D\tau_B$, and D is the Stokes-Einstein diffusion constant (West et al 1994).

4.3 Gelation

A particulate gel is a dispersion consisting of two continuous phases: the liquid and the particle network, with the latter determining the strength of the gel (Strenge 1993). The term "gel" has been used rather vaguely to describe anything with a jelly-like consistency, sometimes with the specification that there should be a non-zero yield stress (Evans & Wennerström 1999). The definition used in this work is based on the light scattering experiments. That is, when the scattered light does not evolve further with time, the system is called a gel which is not necessarily an elastic gel (e.g., gelatin gel or jelly). From this point of view a *gel* can be defined as below:

As fractal aggregates grow, their mass increases less rapidly with size than would be the case for homogenously close packed clusters. In nondilute dispersions, the space occupied by the growing fractal aggregates eventually fills the entire space available, and so by necessity the aggregates connect together to produce a system-spanning network, i.e., a gel (Dickinson 2000). This occurs approximately when the monomer volume fraction of an individual cluster $f_{v,c}$ (i.e., referred to as the effective volume fraction) is equal to the fixed monomer volume fraction of the entire system, f_v, $f_{v,c} = f_v$ (Bremer et al 1995, Dickinson 2000, Sorensen et al 1998).

Figure 4.5 illustrates the transition from a sol to a gel. As depicted in this figure, the *gel* forms when the clusters reach to a critical size, spanning the entire system.

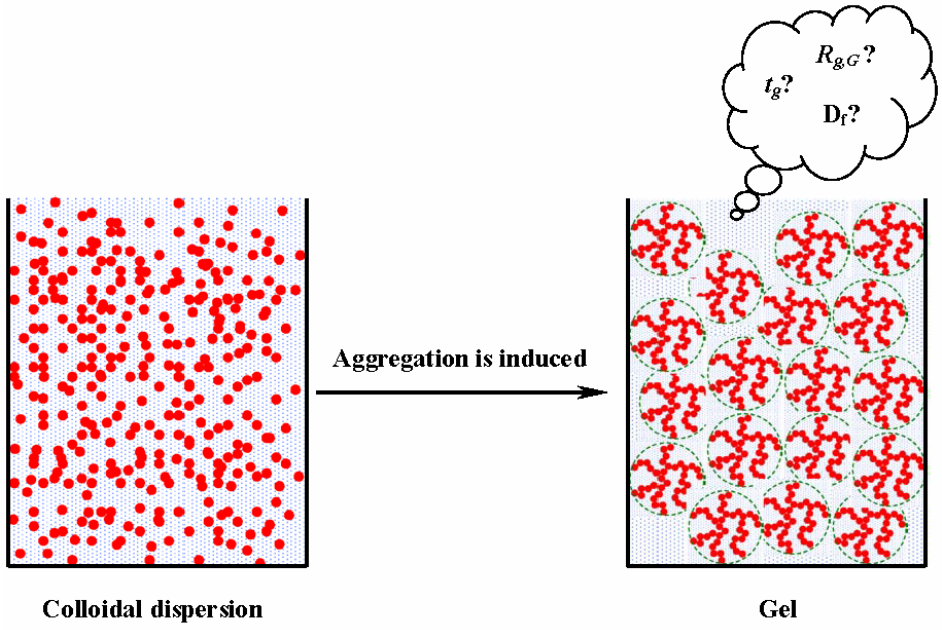

Figure 4.5 Transition from a sol to a gel. The colloidal solution can be destabilized by any mechanisms given earlier. A gel can form when the aggregates reach a critical size at which they span the entire system.

The size of the aggregates at the gel point, $R_{g,G}$ and the gel time t_g can be determined theoretically by applying the condition given above. We then compare the theoretical gel time with the measured gel time using SALS. Before proceeding to derive $R_{g,G}$, t_g, a few definitions are needed to be given first:

4.3.1 Aggregates Radius of Gyration, R_g

The radius of gyration R_g of an aggregate is a measure of its overall size, and it can be expressed as

$$R_g^2 = \frac{\int r^2 \rho(\vec{r})\, d\vec{r}}{\int \rho(\vec{r})\, d\vec{r}}, \tag{4.34}$$

where r is the radial distance measured from the cluster center of mass and $\rho(\vec{r})$ is the position dependent mass density (Fry et al 2004). As mentioned earlier the mass density of a fractal object corresponds to its size by a power law, i.e.,

$$\rho(\vec{r}) = \rho_o\, r^{\mathrm{D_f - d}}, \tag{4.35}$$

where d is the spatial dimension. Cluster mass scales with its geometric size as

$$M \sim (\frac{R_g}{a})^{\mathrm{D_f}}, \tag{4.36}$$

where a is the monomer size. The above equation is similar to the expression given earlier for the Sierpinski fractals, i.e., $M \sim (L/l)^{\mathrm{D_f}}$.

4.3.1.1 Number of Monomers per Cluster, *N*

The number of primary particles in an aggregate of size R_g scales as

$$N = k_o (\frac{R_g}{a})^{\mathrm{D_f}}, \tag{4.37}$$

where k_o is the prefactor of the fractal scaling relationship. In the DLCA regime $k_o \approx 1.3$ (Sorensen & Roberts 1997), and in a RLCA regime $k_o \approx 1.2$ (Fry et al 2004).

In an aggregating system, mass conservation during aggregation implies a constant number of monomers n_m in the system. Hence the number of monomers per cluster N times the

cluster number density n_c (i.e., number of clusters in the system) should be conserved and equal to n_m, i.e.,

$$n_m = N n_c . \tag{4.38}$$

4.3.2 Perimeter Radius R_p

In analogy with a solid sphere, the perimeter radius is defined for fractal aggregates by considering a fractal aggregate as spherically isotropic cluster of radius R_p. In order to find R_p, Eq. (4.35) can be substituted into Eq. (4.34) to yield

$$\mathrm{R_g^2} = \frac{\int_0^{\mathrm{R_p}} \rho_\mathrm{o}\, \mathrm{r}^{\mathrm{D_f}-3} \mathrm{r}^4 \mathrm{dr}}{\int \rho_\mathrm{o}\, \mathrm{r}^{\mathrm{D_f}-3} \mathrm{r}^2 \mathrm{dr}} = \frac{\int_0^{\mathrm{R_p}} \mathrm{r}^{\mathrm{D_f}+1} \mathrm{dr}}{\int_0^{\mathrm{R_p}} \mathrm{r}^{\mathrm{D_f}-1} \mathrm{dr}}, \tag{4.39}$$

then by integrating Eq. (4.39), we have

$$R_g^2 = \frac{\mathrm{D_f}}{\mathrm{D_f}+2} R_p^2 . \tag{4.40}$$

Equation (4.40) can be refined if a power law density correlation function $g(r)$ is used instead of the power law density $\rho(r)$, i.e.,

$$R_g^2 = \frac{2\mathrm{D_f}(\mathrm{D_f}+1)}{(\mathrm{D_f}+5)(\mathrm{D_f}+2)} R_p^2 . \tag{4.41}$$

Equations (4.40) and (4.41) are especially useful to determine R_g when one analyzes the 2-d projection of a fractal aggregate (Oh & Sorensen 1997). However, for simplicity we will use Eq. (4.40) when needed.

The radius of gyration and the perimeter radius are depicted in a cartoon shown in Fig. 4.6.

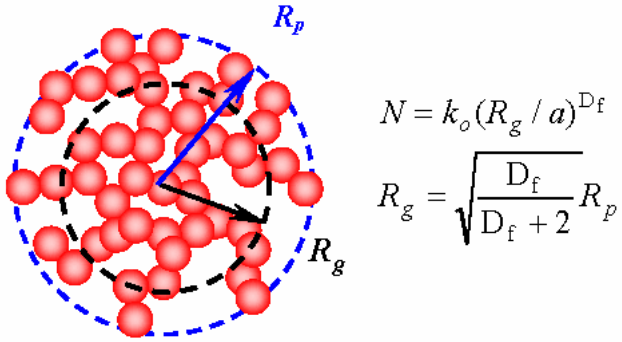

Figure4.6 A cartoon of a fractal aggregate. The radius of gyration and the perimeter radius are illustrated by the black and green dashed circles, respectively. The ratio R_g / R_p for an aggregate is 0.69 in the DLCA regime.

4.3.3 Radius of Gyration at the Gel Point

As mentioned earlier, at the gel point, the monomer volume fraction[15] of an individual cluster $f_{v,c}$ is equal to the fixed monomer volume fraction of the entire system, f_v. The monomer volume fraction of a colloidal solution can be determined by knowing the monomer number density provided by the manufacturers (e.g., Invitrogen Corp.), i.e.,

$$f_v = n_m (4/3)\pi a^3, \tag{4.42}$$

[15] Volume fraction f_v is the ratio of the volume of the dispersed phase to the true volume of the dispersion. In colloid science f_v is often denoted as ϕ.

where n_m is the monomer number density, and a is the radius of the monodispersed particles. Thus, the initial volume fraction of a system is a known parameter. The monomer volume fraction of an individual cluster $f_{v,c}$ is

$$f_{v,c} = \frac{N(4/3)\pi a^3}{(4/3)\pi R_p^3}, \tag{4.43}$$

where N is the number of monomers per cluster, and R_p is the cluster perimeter radius. For simplicity, it is assumed that the clusters are monodisperse and spherical. Substituting Eqs. (4.37) and (4.40) into Eq. (4.43) yields

$$f_{v,c} = k_o \left(\frac{\mathrm{D_f}}{\mathrm{D_f}+2}\right)^{3/2} \left(\frac{R_{g,G}}{a}\right)^{\mathrm{D_f}-3} \tag{4.44}$$

where $R_{g,G}$ is the radius of gyration at the gel point. $R_{g,G}$ can be determined by using Eq. (4.44) and $f_{v,c} = f_v$, i.e.,

$$R_{g,G} = a\left[k_o^{-1}\left(\frac{\mathrm{D_f}+2}{\mathrm{D_f}}\right)^{3/2} f_v\right]^{1/(\mathrm{D_f}-3)} \tag{4.45}$$

Equation (4.45) can be approximated for the DLCA regime as

$$R_{g,G} \approx 0.5\, a\, f_v^{\,1/(\mathrm{D_f}-3)}. \tag{4.46}$$

4.3.4 Theoretical Gel Time

A scaling argument can be used to approximately determine the theoretical gel time. The theoretical gel time is related to the characteristic time, i.e., $t_g \propto t_c$. The gel time is basically the

time needed for the monomers to aggregate to form a cluster of size $R_{g,G}$. The number of monomers N_G in an aggregate of size $R_{g,G}$ can be determined using Eq. (4.37), i.e.,

$$N_G = k_o (\frac{R_{g,G}}{a})^{\mathrm{D_f}}. \tag{4.47}$$

N_G is the proportionality constant relating t_c to t_g, and hence

$$t_g = N_G t_c. \tag{4.48}$$

Equation (4.48) can also be obtained by using Eqs. (4.19) and (4.38). By substituting Eqs. (4.45) and (4.47) into Eq. (4.48), the gel time can be obtained, i.e.,

$$t_g = t_c \left[k_o^{-3/\mathrm{D_f}} (\frac{\mathrm{D_f} + 2}{\mathrm{D_f}})^{3/2} f_v \right]^{\mathrm{D_f}/(\mathrm{D_f}-3)}. \tag{4.49}$$

Equation (4.49) can be used for both DLCA and RLCA regimes as described below.

4.3.4.1 The DLCA Regime

Substitution of t_c (i.e., Eq. (4.20)) into Eq. (4.49) and some further simplifications leads to an approximation of the gel time, i.e.,

$$t_g \approx \frac{\eta a^3}{k_B T} f_v^{3/(\mathrm{D_f}-3)}, \tag{4.50}$$

4.3.4.2 The RLCA Regime

In the RLCA regime, the characteristic time given in Eq. (4.20) requires the correction factor of W (i.e., stability ratio) (Russel et al 1999)

$$t_c = \frac{\pi \eta a^3 W}{f_v k_B T}, \tag{4.51}$$

where W can be measured experimentally, or can be calculated by using Eq. (4.23) in which the $\phi_{\max}$ can be obtained from the DLVO theory, or Eq. (4.24). The gel time in the RLCA regime can be obtained by substituting Eq. (4.51) in Eq. (4.49), i.e.,

$$t_g \approx \frac{\eta a^3 W}{k_B T} f_v^{3/(\mathrm{D_f}-3)}, \tag{4.52}$$

It is important to note that the definition of a gel point is based on several assumptions that are invalid for real systems (Dickinson 2000).

(i) It is known experimentally that fractal aggregtaes formed in DLCA or RLCA regime have a broad cluster-mass distribution with the time dependent mean size. This means that when the largest aggregates are just beginning to join together to form a system spanning network, a susbstantial fraction of the particles still exist as monomers or small aggregates. These "free" particles become incorporated into the dveloping network structure only at times well beyond the gel point.

(ii) In this model, the aggregate-aggregate interactions are neglected. In reality, even in the initial stages of aggregation of a nondilulte dispersions, the local aggregate growth must depend on the local particle concentartion gradient, and hence depending on the growth of the neighboring aggregates.

(iii) Once the mean aggregate radius is approaching $R_{g,G}$, the increasing crowding and interpenetration of the largest aggregates must inevitably modify their structure in the

gelling system from that in the nongelling DLCA or RLCA system at high dilution leading to an increase in th edegree of compactness of the largest aggregates, i.e., to increase their effective fractal dimension.

In practice, however, the simple model of gelation can remain reasonably valid up to concentartions at which the aggregates' radii are conciderably larger than the average size of the gaps seperating the neighboring clusters (i.e., nearenest neighbour seperation) (Dickinson 2000).

CHAPTER 5 Experimental Methods

5.1 Small Angle Light Scattering (SALS) Setup

Small angle static light scattering (SALS) is one of the most useful techniques to probe length scales of the order of the wavelength of light or larger. This technique allows the determination of fundamental parameters such as fractal dimension and sizes of aggregating clusters or the correlation length of a critical system undergoing a phase transition. This technique is also suitable to investigate the kinetics of a growth process in an aggregating system.

SALS is not only of interest for basic research. It is also used in many fields of applied sciences, such as in atmospheric and aerosol sciences (Friedlander 2000), or in pharmaceutical and agricultural industries. The interest for SALS relies on its capabilities to perform particle size measurements. Therefore, SALS finds application in many industrial situations, and nowadays, commercial instruments are available on the market. However, we would prefer to build the SALS ourselves. Because, with the commercial SALS the apparatus would be less flexible to any modification related to the different experiments performed in this lab, such as studying the flame soot (Kim et al 2004), aerosol gel formed in a combustion chamber (Dhaubhadel et al 2006), or the shear experiments presented in this work. In addition, by building the SALS setup, we could fix almost any problem that would arise with the set up.

Different designs for the SALS set up have been suggested in the literature (Carpineti et al 1990, Ferri 1997, Weber & Schosseler 2002). Our SALS set up is similar to that of Ferri (Ferri 1997).

Figure 5.1 shows the schematic diagram of the experimental setup. We used a vertically polarized argon-ion laser (Spectra Physics 165) with the Model 265 Power Supply. The laser was operating at a wavelength of $\lambda_o = 488\,nm$. The size of the laser beam at $1/e^2$ is 1.25 mm. A

variable attenuator made of a Glan-Thompson polarizer and a linear polarizer was used to reduce the beam power and sets the polarization of the electrical field in the vertical direction. The beam then hits the sample. The light scattered by the sample is then collected by lens L_1 (Achromat F =75 mm, ϕ=50.8 mm, Thorlabs AC508-075-A1). The Fourier image (Hecht 2002) of the sample forms at the focal plane of L_1 ; this Fourier image is what we are interested to detect. The lens L_2 (Achromat F =100 mm, ϕ=50.8 mm, Thorlabs AC508-100-A1) conjugates the Fourier plane of the lens L_1 and the plane of the detector sensor. A mirror, made of a drill bit (Gage 73, 0.024 inches) cut and polished at 45°, is placed in the focal plane of the lens L_1 . The small mirror deviates the transmitted beam to ca. 90° preventing the unscattered beam from reaching the detector. In order to avoid vignetting problems (Hecht 2002) associated with the lens L_2 , the cell is placed at a distance from the lens L_1 so that the cell plane and the L_2 plane are conjugated via the lens L_1 . Hence, all the light collected by the lens L_1 is also collected by the lens L_2 .

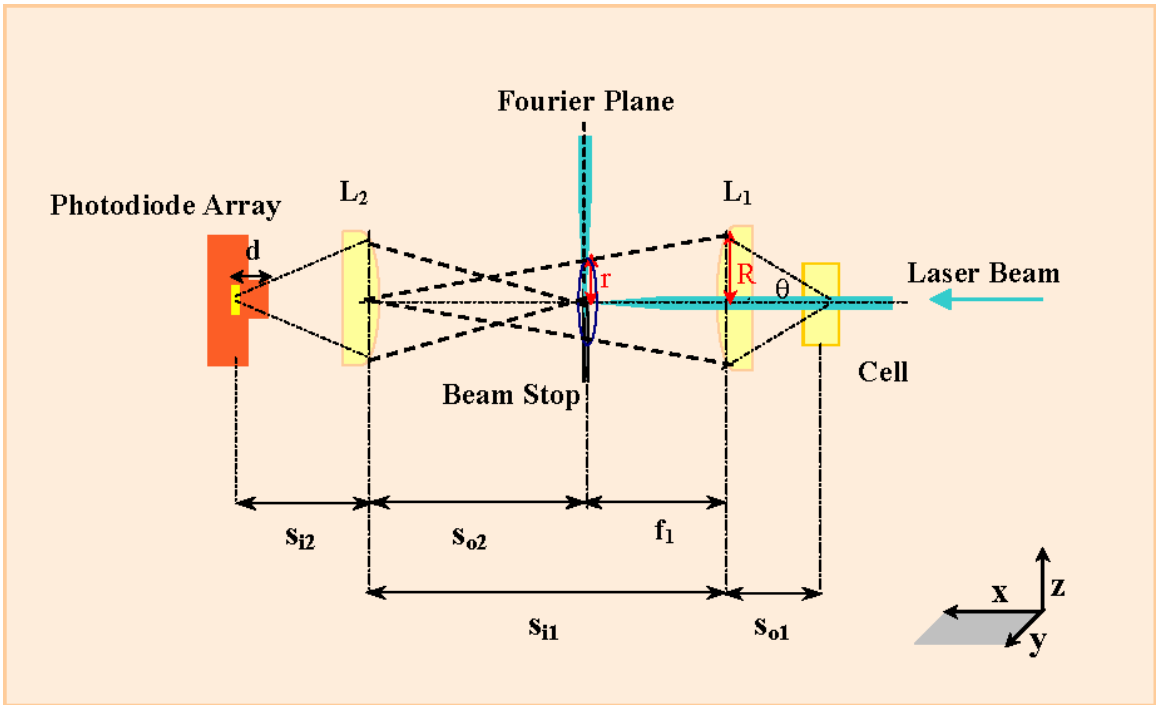

Figure 5.1 Schematic diagram of the Small Angle Light Scattering set up. The picture is not drawn to scale.

Although L_2 appears to be only conjugating the focal plane of L_1 and the detector sensor, there is an advantage of having L_2 in this setup

- By placing the detector at the focal plane of the lens L_1 , the transmitted focused beam needs to pass clear the detector without affecting the measurements. This can be done by inserting a tiny hole inside the detector (Carpineti et al 1990); with this configuration the detector needs to be specifically altered for this purpose. However, in Ferri's setup there is an advantage of simply placing a small mirror at the focal plane of L_1 .
- Lens L_2 conjugates the image formed at the focal plane of L_1 onto the detector sensor with a magnification less than one. Therefore, lens L_2 would allow one to collect the maximum scattered light from the sample without being limited by the actual size of the sensor chip.

In order to avoid the spherical aberration (Hecht 2002), hence obtaining a good calibration, it is important to position the correct side of both lenses in the SALS set up. As can be seen in Fig. 5.1, the more convex side of L_1 should face farther from the sample to suppress the spherical aberration. Subsequently, we should position L_2 with the more convex side towards L_1 . A simple experiment can be done to test the spherical aberration by placing a study lamp closely behind the lens and looking at the real image formed. The image is more focused when the less convex side of the lens is facing towards the study lamp.

We used a N-MOS 512 pixel photodiode array (HAMAMATSU, S 3902). Each pixel has 50 μm pitch and 0.5 mm height. The maximum light sensitivity of the detector is at 600 nm. The light sensitivity of the detector at 488 nm is ca. 10% less compared to that at 632 nm. The detector runs at 62.5 kHz pixel readout rate and a 50 ms integration time (20 Hz). The dynamic range of the detector (i.e., peak signal to RMS noise) is 30,000 to 1.

A Labview Interface program was used for the data acquisition. This program uses a National Instruments PCI-6034E Data Acquisition Card (NI Part # 778075-01) to collect "frames" of data. Each frame consists of one-512 pixel array with 16-bit resolution.

We determined the scattering wave vector q similar to that described by Ferri (Ferri 1997) as follows:

The light scattered at an angle θ is mapped by the lens L_1 into a ring of radius r placed on the focal plane (i.e., Fourier plane) of the lens L_1 [16]:

$$r = f_1 \tan\theta, \tag{5.1}$$

where f_1 is the focal distance of L_1. The horizontal component of this ring is then mapped by L_2 on the photodiode array into a distance l

$$l = r\,(s_{i2} / s_{o2}), \tag{5.2}$$

where s_{o2} and s_{i2} are, respectively, the object distance and the image distance of L_2. The scattering wave vector in the medium is

$$q = (4\pi / \lambda)\sin(\theta / 2), \tag{5.3}$$

where λ and θ are the wavelength of light and the scattering angle in the medium. However, we are interested to relate the scattering wave vector in the medium to that in the air

$$q = (4\pi / \lambda_o)\sin(\theta_o / 2), \tag{5.4}$$

where both λ_o and θ_o are the wavelength of light and the scattering angle in the air.

---

16 One can obtain Eq. (5.1) by using the thin lens equation (i.e., $1/s_{o1}+1/s_{i1}=1/f_1$) and $R/r = s_{i1}/(s_{i1}-f_1)$, where s_{o1} and s_{i1} are, respectively, the object and the image distances. The scattered light at angle θ refracts from L_1 at a distance R from the optical axis of L_1.

It can be shown that Eqs. (5.3) and (5.4) are identical when one uses a square cell[17]. We can now combine Eqs. (5.1), (5.2), (5.4), and the small angle approximation to obtain

$$q = \frac{2\pi}{\lambda_o}(s_{o2}\, l / f_1 s_{i2}). \tag{5.5}$$

In Eq. (5.5), l can be written in terms of the photodiode array pixel size and the pixel number as

$$l = (50\mu m) \times (\text{pixel \#}). \tag{5.6}$$

In order to find all the parameters for SALS setup, we started with an arbitrary distance for s_{o2}. We then calculated all the subsequent parameters and chose the parameters that would give the optimum results. However, we needed to consider the following points:

(i) There are always some limits set by the size of the optical table. We also prefered to keep the set up simple, and hence easy to calibrate. Therefore, we did not use any mirror to direct the beam around the optical table to gain more space.

(ii) To collect the maximum *possible* scattered angle with L_1 , i.e., 15°.

(iii) To avoid the vignetting problem: $2w_o(s_{i1}/s_{o1}) < \phi_2$, where $2w_o$ and ϕ_2 are, respectively, the laser beam diameter and the diameter of L_2 .

(iv) The PDA pixel size was 50 μm which was large compared to a typical CCD detector with a pixel size of ca. 10 μm. Therefore, in order to increase the image resolution with our available experimental setup, we kept the ratio $q/\text{pixel\#}$ small without sacrificing the maximum scattered angle collected by L_1. The only parameters in Eq. (5.5) that could conveniently be adjusted were s_{o2} and s_{i2}.

---

[17] By using the Snell's Law (i.e., $n\sin\theta=\sin\theta_o$, where n is the refractive index of the medium), $\lambda=\lambda_o/n$, and the small angle approximation ($\sin\theta\sim\theta$), one can show that Eqs. (5.3) and (5.4) are identical in a square cell.

The parameters (i.e., s_{o1}, s_{i1}, s_{o2}, and s_{i2}) depicted in Fig. 5.1 are s_{o1}=94 mm, s_{i1}=371 mm, s_{o2}=296 mm, and s_{i2}=151 mm. Note that all these parameters are measured from the principal planes of the lenses whose thicknesses are no longer negligible (Hecht 2002). The actual photodiode array chip (see Fig. 5.1) is located at ca. $d = 40$ mm from the outermost edge of the PDA detector.

We first needed to align the SALS setup before calibrating the set up. Since the SALS apparatus is meant to collect the scattered light at very small angles (i.e., 0.1^{o}), alignment of the laser beam is therefore an important procedure. One can first align the laser beam without having the optical components in place and then place a few irises to set a reference point during the alignment procedure. She/he can then place the lens L_1 and ensure that the beam is passing through the center of L_1 . This task can be easily done by having an iris at the front (or object side) of L_1 . One can then adjust L_1 (i.e., mounted on a XYZ translation stage) by looking at the backscattered beam onto the iris just behind L_1. The backscattered beam does not overlap with the incoming beam unless the beam has passed through the center of L_1. One can hold and precisely mark the position of each lens by using the L-shaped metal brackets. These brackets are bolted to the optical table as a guide which can sometimes be advantageous compared to bolting down the translation stages. Quite often, there is a need to repeat a process (alignment, calibration) several times; therefore, it would be less time consuming and more convenient if one can easily remove the lenses and/or put the lenses back in just a few seconds. The same procedure should be repeated for L_2 . Note that the alignment of the laser beam should be checked with the detector throughout the calibration procedure, i.e., the maximum peak of the beam should remain at the same pixel number.

Figure 5.2 shows the small angle light scattering set up. This setup can detect the scattering angle approximately ranging between 0.09^{o} - 14^{o} corresponding to the scattering wave vector ranging between ca. 200 cm^{-1} - 31000 cm^{-1}.

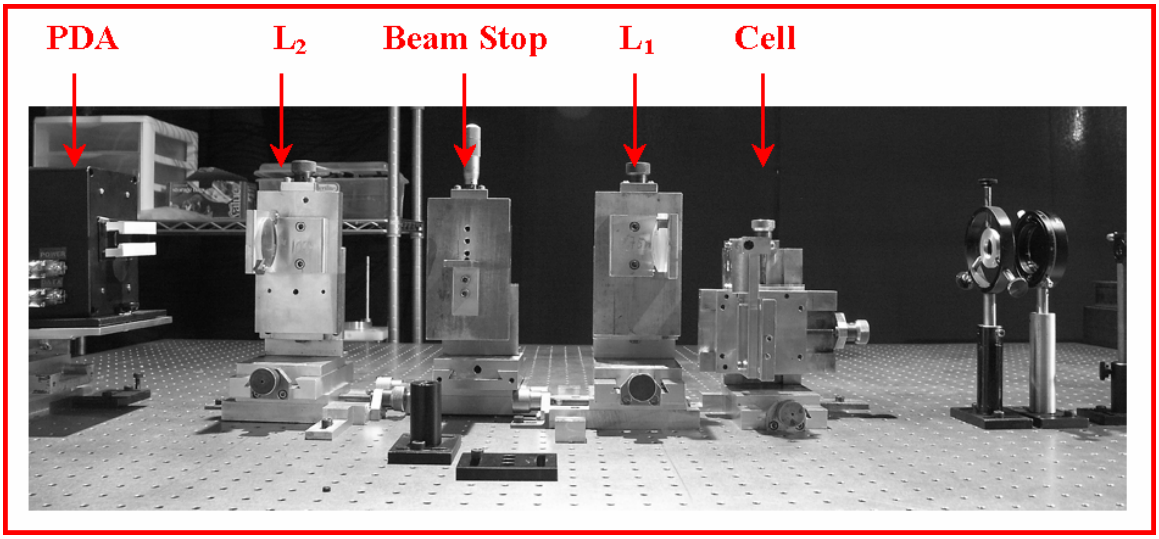

Figure 5.2 The Small Angle Light Scattering set up. The scattering angles ranges between 0.09° and 14°.

5.1.1 SALS Calibrations

The calibration of the SALS setup was carried out by using a 10 μm (Lenox Laser, A-SLIT-3/8-DISC-10) single slit. In order to adjust the position of the single slit, it was mounted onto a XYZ translation stage. We placed the slit at $s_{o1} = 94\,\text{mm}$, i.e., measured from its respective principal plane of the lens L_1. We then adjusted the position of the single slit and the detector in y-z plane to ensure that the maximum intensity was detected by the detector.

In order to minimize the stray light getting into the detector, we performed the experiment in a dark room. In addition, a cardboard box was placed over the detector and the lenses to ensure the maximum darkness during the measurements. We also removed the small mirror while calibrating the set up with the single slit.

The scattered intensity was then collected versus the pixel number. In order to measure the background, which was the ambient dark room in this experiment, the laser beam was blocked and the data were measured accordingly; the background was then subtracted from the

data. Note that the background measurements should be determined according to each experiment, and hence can be measured quite differently. To compare the calibration data with theory, we used the far-field diffraction theory (i.e., Fraunhofer diffraction) of a single slit, i.e.,

$$I(q) = I(0)\left(\frac{\sin(Dq/2)}{(Dq/2)}\right)^2, \tag{5.7}$$

where D (i.e., 10 μm) is the width of the single slit (Hecht 2002).

Figure 5.3 shows the result of the single slit calibration for s_{o1}=94 mm, s_{i1}=371 mm, s_{o2}=296 mm, s_{i2}=151 mm. In this figure the scattered intensity $I(q)$ is plotted versus q, i.e., determined from Eqs. (5.5) and (5.6). The experimental data are normalized to one on the intensity scale.

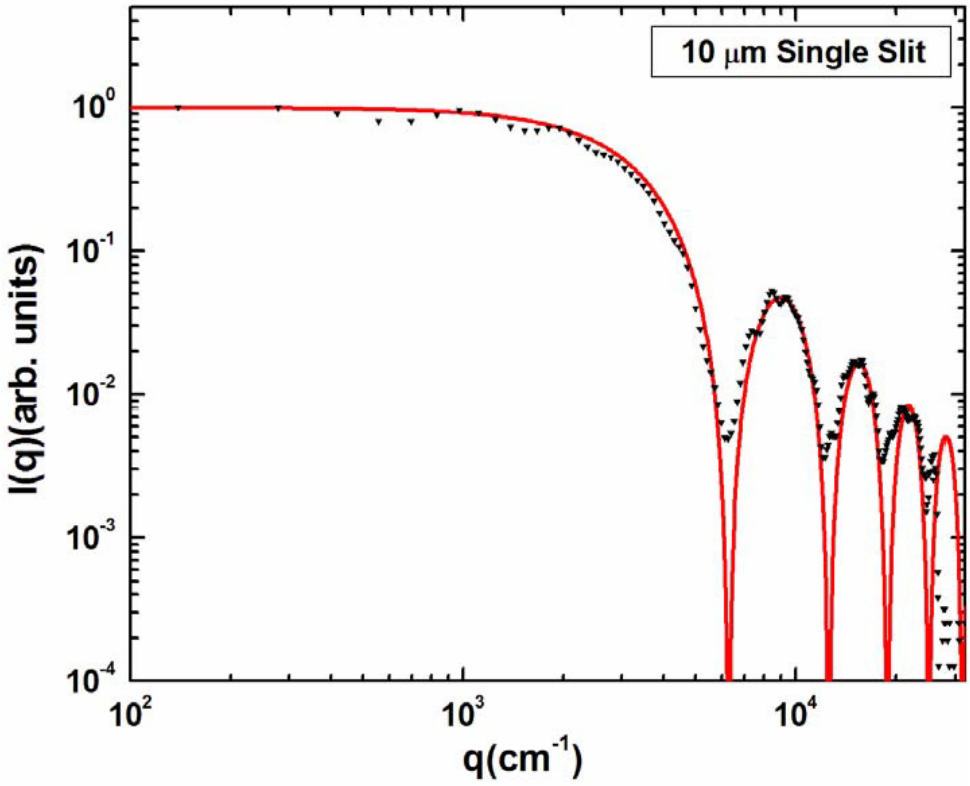

Figure 5.3 The 10 μm single slit calibration for the SALS setup, where s_{o1} = 94 mm, s_{i1} = 371 mm s_{o2} = 296 mm, and s_{i2} = 151 mm.

As can be seen in Fig. 5.3, the experimental data are somewhat noisy; also, the detected scattering angle is less than what was expected, i.e., based on Eq. (5.5) and (5.6) for the values given in the previous page.

We then gradually decreased the distance between the single slit and L_1 until the fourth peak was detected as well, we then measured the distance which is s_{o1} = 82 mm. The calibration for the new configuration is shown in Fig. 5.4.

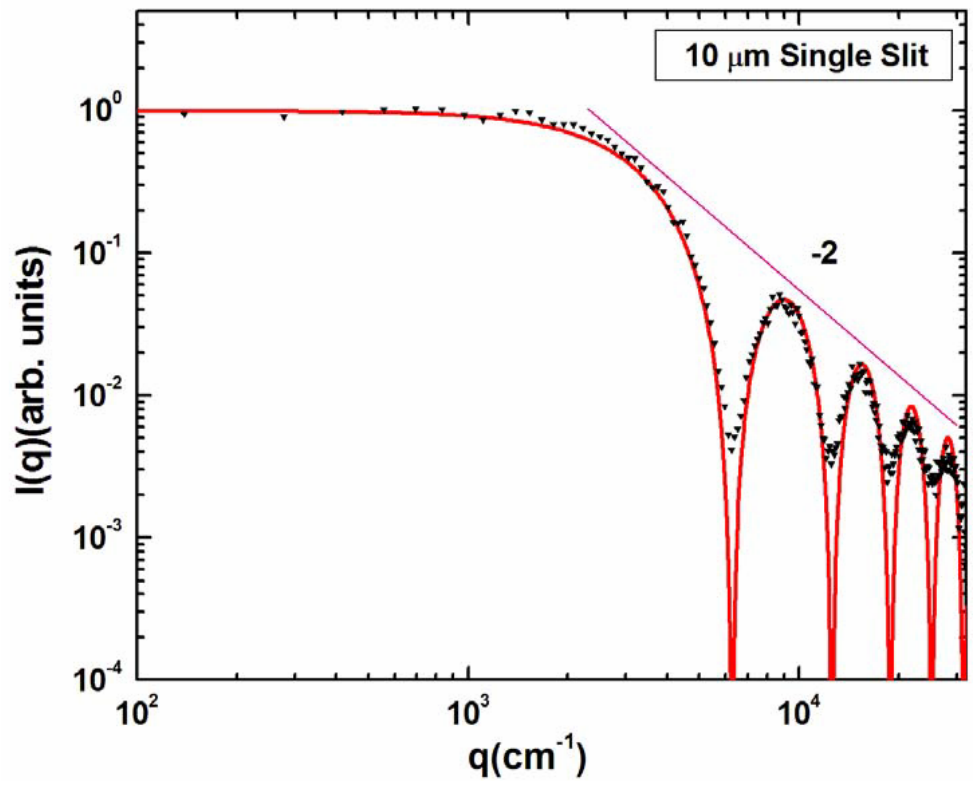

Figure 5.4 The 10 μm single slit calibration for the SALS setup, where s_{o1} = 82 mm, s_{i1} = 371 mm s_{o2} = 296 mm, and s_{i2} = 151 mm.

We also found that if we increase the distance between the detector and L_2 ,i.e., from s_{i2} = 151 mm to s_{i2} = 180 mm, we would get a less noisy result for the calibration which is shown in Fig. 5.5. The reason could be that the image formed on the detector was slightly

magnified to yield a smaller calibration factor (i.e., the correlation between q and pixel number), and hence a higher resolution. In addition, the calibration factor was adjusted according to the new configuration. However, it is important to note that once the calibration factor is determined, it has to remain fixed throughout later experiments. The SALS set up can also be calibrated by using a 10 μm pinhole; however, in this case the signal to noise is weaker compared to the single slit calibration.

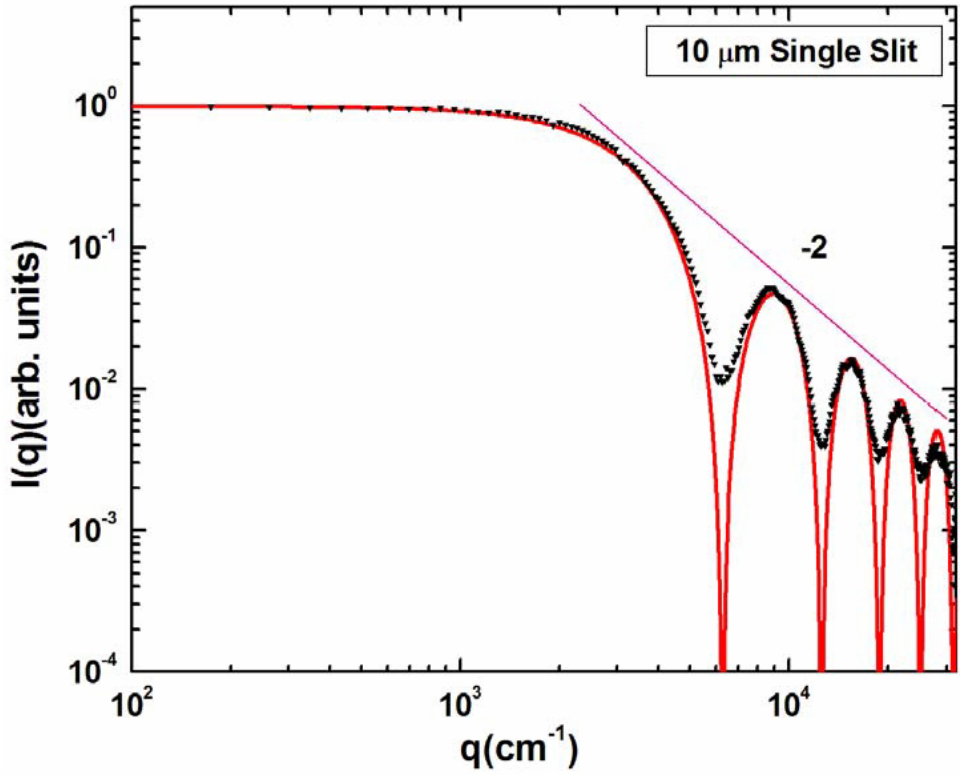

Figure 5.5 The 10 μm single slit calibration for the SALS setup, where s_{o1} = 82 mm, s_{i1} = 371 mm s_{o2} = 296 mm, and s_{i2} = 180 mm.

In order to test the setup further, we performed an experiment with aqueous dispersions of polystyrene latex spheres with a diameter of 9.6 μm (7.4% coefficient of variance), obtained from Interfacial Dynamics Corporation. The volume fraction was chosen so that multiple scattering was negligible (Chapter 3). We used a quartz cell with an optical path length of 2 mm.

Prior to the measurements, the empty cell was first placed on the translation stage. The position of the cell in y-z plane was adjusted in order to minimize the scattering from the empty cell which could be due to the imperfection in the quartz cell. The cell was then slightly tilted with respect to the optical axis to avoid beam reflections falling onto the detector (Ferri 1997). Then, the small mirror was adjusted so that the focused transmitted beam hit the tip very close to the upper edge, allowing the scattered light at very small angles to pass clear. The cell was then filled with distilled water and was positioned on the translation stage. The background data was then measured and was subsequently subtracted from the measurements. The colloidal suspension was then transferred into the cell, and the scattered light intensity was measured versus the pixel number, hence q.

Figure 5.6 shows the scattered intensities $I(q)$ versus q . The volume fraction of the polystyrene dispersion was $f_v = 5 \times 10^{-4}$. The theoretical Mie-Lorentz scattering curve (red curve) is also plotted as a reference (see section 3.4). The agreement between theory and experiment was satisfactory.

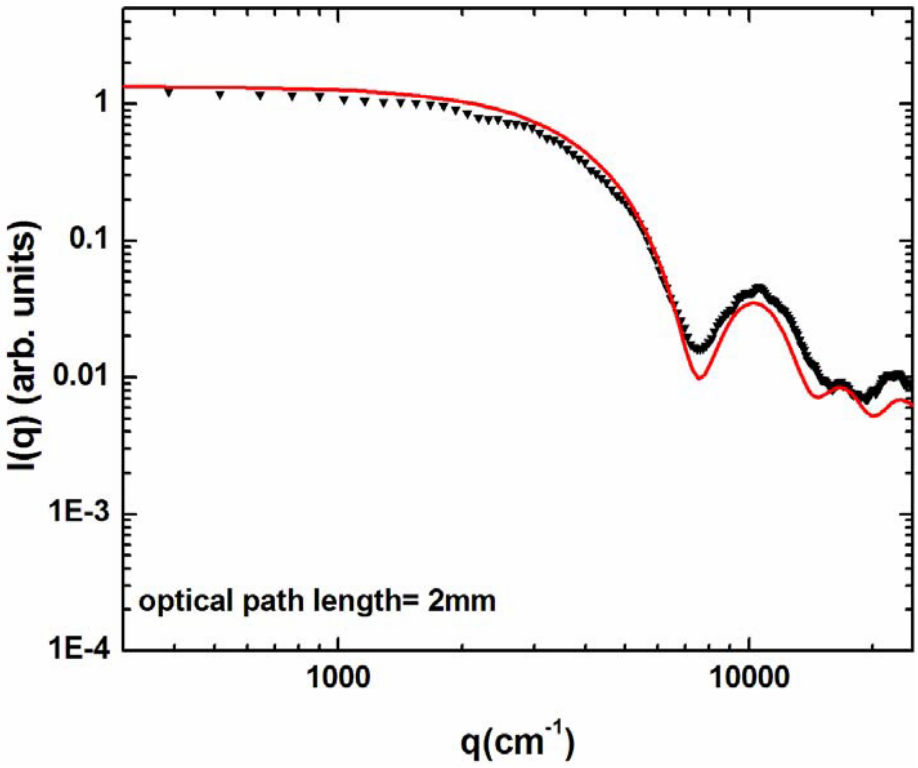

Figure 5.6 The scattered intensity is plotted versus q for a dispersed solution of polystyrene microspheres (9.6 μm). The volume fraction is $f_v = 5 \times 10^{-4}$. The result is compared to the Mie-Lorentz theory.

5.2 Experimental Methods and the Scattering Cell

The experiments were performed with surfactant-free nearly monodisperse polystyrene latex spheres with a diameter of σ = 20 nm (12-15% coefficient of variance which was provided by the manufacturer), purchased from IDC. The surface of polystyrene colloids is negatively charged with sulfate and high density of carboxylate-modified functional groups on the surface (i.e., CML). The surface charge is pH dependent, but is stable at wide range of pH. In addition, the surface (i.e., negatively charged) is hydrophobic at low pH and somewhat hydrophilic at high pH. In order to minimize bacterial contamination, the polystyrene samples should be stored in the refrigerator at 2-8 ^oC. Magnesium chloride salt ($MgCl_2$) (purchased from Aldrich) was used

to screen the double-layer repulsive potential (DLVO theory), and hence to induce the aggregation.

The polystyrene and $MgCl_2$ solutions were prepared in a 50-50 volume to volume mixture of H_2O and D_2O (purchased from Cambridge Isotopes Lab, Inc.) to match the density of polystyrene (i.e., 1.05 g/cm^3) (Cipelletti et al 2000); hence, to prevent any sedimentation effects due to gravity (Allain & Cloitre 1993, Allain et al 1995, Asnaghi et al 1992, Gonzalez 2001). Equal volumes of polystyrene dispersions and $MgCl_2$ solutions were simultaneously squirted using micro liter syringes (Hamilton Company) into the scattering cell (i.e., described below). The scattering cell was then mounted on a XYZ-translation stage for SALS measurements.

The scattering cell, which is shown in Fig. 5.7, was made of one O-ring (silicone or Viton) sandwiched between two 23 mm-diameter quartz windows (purchased from NSG Precision Cells, Inc.) and two washers (i.e., to help to seal the sample). The sample was sealed inside a metal sample holder, which had a hole centered on the quartz windows. The scattering cell was then immediately mounted onto a sample holder (i.e., sample rotator). The background intensity was then measured after placing the unstable colloidal sample on the sample holder. The background intensity, which was very small fraction of the scattered intensity, was then subtracted from subsequent light scattering measurements.

Prior to any light scattering measurement, the empty cell was first placed on the translation stage. The position of the cell in Y-Z plane was adjusted so that the backscattered beam from both windows overlapped. This was particularly needed for the scattering cell used in this work, because the two windows could not exactly be parallel, and hence this procedure was required before any light scattering measurements. The cell was then slightly tilted with respect to the optical axis to avoid beam reflections falling onto the detector (Ferri 1997). The background intensity was measured immediately after placing the unstable colloidal sample on the sample holder. The background intensity, which was very small fraction of the scattered intensity, was then subtracted from subsequent light scattering measurements. It is important to note that the largest aggregate size in our experiments were approximately 20 μm whereas the

size of the laser beam was 1.25 mm. Therefore, the light scattering measurement were an ensemble average over the area of the laser beam hitting the sample.

Figure 5.7 The scattering cell (left) and the sample holder (right) are shown. The solutions are injected into the cell through two holes inserted in the O-ring. The metal sample holder has a hole centered on the quartz windows. The sample is mounted onto the translation stage for SALS measurements

CHAPTER 6 Light Scattering Measurements of the Gel Time in the DLCA Regime

6.1 Motivation

Our motivation to perform these experiments was based on the discrepancy we found between our experimental gel time in a DLCA regime and the theoretical gel time given in Eq. (4.50). Here we show the reason for this discrepancy.

In Fig. 6.1, the theoretical characteristic time (below) and the theoretical gel time (top) are plotted versus various volume fractions of particles of radii 10 nm and 100 nm as examples. Water was chosen as the dispersed medium having a viscosity of $\eta = 0.89 \times 10^{-3} (kg/ms)$ at $25^{o}C$. The fractal dimension of $D_f = 1.8$ (representing a DLCA process) was used to calculate Eq. (4.49). The dashed line shown in Fig. 6.1 (below) is the mixing time (i.e., typically about one second) which is the time required to stir the colloidal solutions and the salt concentrations. The latter is used to screen the double layer repulsive potential of the initially charge stabilized particles, and thus to induce an aggregation.

As can be seen in Fig. 6.1 (below) the mixing time is two to three orders of magnitude larger than the characteristic time, indicating that mixing can effect (enhance or decrease) the aggregation rate in an aggregating system. One is almost tempted to use larger particle sizes to avoid this problem. However, this solution is not as simple as it sounds for two main reasons. By increasing the particle size to (for example) 100 nm, the gel time will unbearably become very long for the measurements, as can be seen in Fig. 6.1 (top). For example, for the volume fraction of 1E-4, the characteristic time is about 6 seconds (i.e., above mixing time); however, one has to wait 666 hours for the sample to gel! On the other hand, one may propose to choose a higher

volume fraction, and hence a more realistic gel time. This, however, could give rise to another problem, particularly in the SALS experiments. That is, the scattering of the particles would enhance significantly ($I \propto a^6$), and hence the multiple scattering would become troublesome.

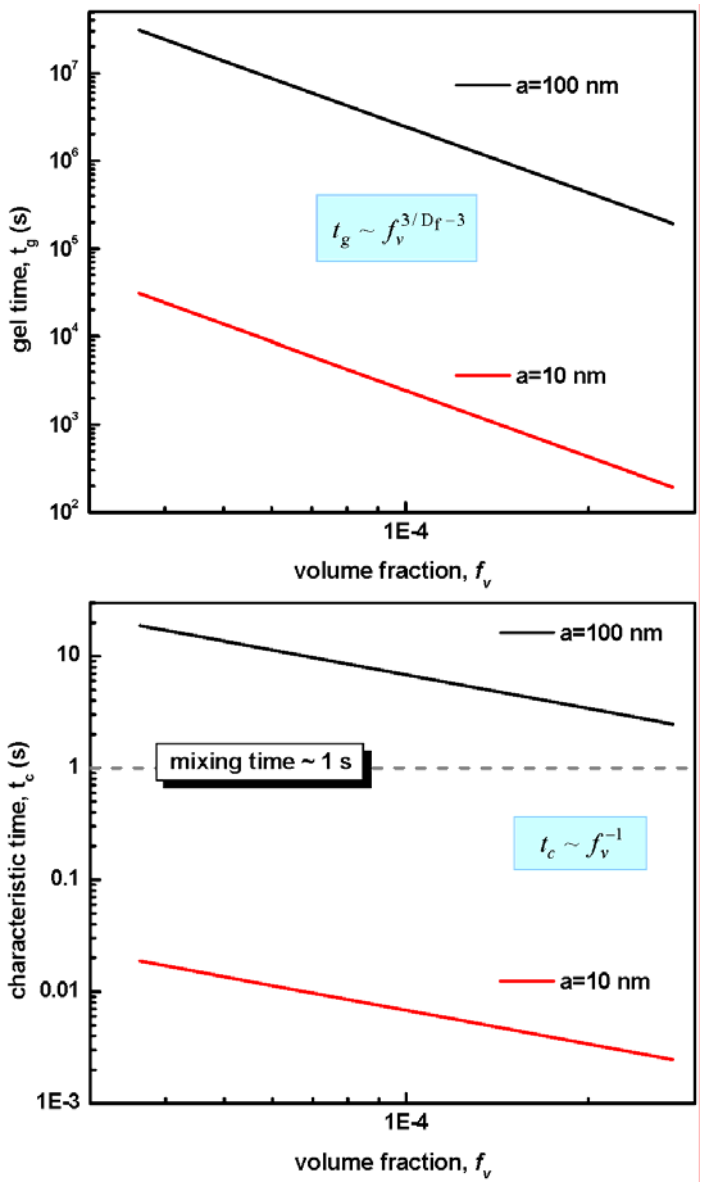

Figure 6.1 The theoretical characteristic time (below) and the gel time (top) are plotted versus various volume fractions for particles of radii 10 nm and 100 nm. The dashed line (below) is the mixing time required to stir the colloidal solution and the salt concentration (i.e., to induce the aggregation).

6.2 Results and Discussions

In order to understand the effect of initial mixing on the aggregation rate in a DLCA regime, we performed a series of light scattering measurements with aqueous dispersions of polystyrene colloids of radius $a = 10\,\text{nm}$ (14.6 % coefficient of variance). The final volume fraction of the polystyrene particles ranged between 3.63×10^{-5} and 2.76×10^{-4} (the initial volume fraction of polystyrene was double the final volume fraction). In order to find the correct range of salt concentrations the following procedure was carried out.

(i) The volume fraction of the polystyrene close to 10^{-4} was chosen so that the experimental gel time can be measured within a reasonable time.
(ii) The salt concentration was varied ranging from 2 mM to 50 mM (i.e., final concentration).
(iii) The gel time was then measured based on the SALS measurements, that is, when the light scattering data stop evolving further within 10% variation (i.e., somewhat arbitrary but the gel time measurements need to be consistent in this sense).
(iv) The gel time measurements (for the given volume fraction) were plotted against the salt concentrations.
(v) The DLCA regime is when the gel time does not depend on the salt molarity. However, in practice, the salt concentration cannot be very high, because the sample flocculates immediately after the initial mixing the two solutions. Here flocculation means that visible sub-millimeter aggregates form in the sample.

Figure 6.2 shows an example of the gel time measurements for various salt concentrations (i.e., 2, 5, 10, and 40mM). The final volume fraction of the polystyrene solution was 1.2E-4.

As can be seen in Fig. 6.2, the gel time remains approximately constant as the salt concentration is decreased from 40 mM to 10 mM; this indicates that the aggregation process is in the DLCA regime (compared to stability ratio shown in Fig 4.4). However, as the salt concentration decreases to 5 mM and 2 mM, the gel time increases indicating that the

aggregation is in the RLCA regime. For the salt concentration of 2 mM, the light scattering of the system remained unchanged comparable to that of the background (i.e., water) for up to 20 hours. Therefore, the measurements were stopped since we were interested to perform the gel time measurements in the fast regime.

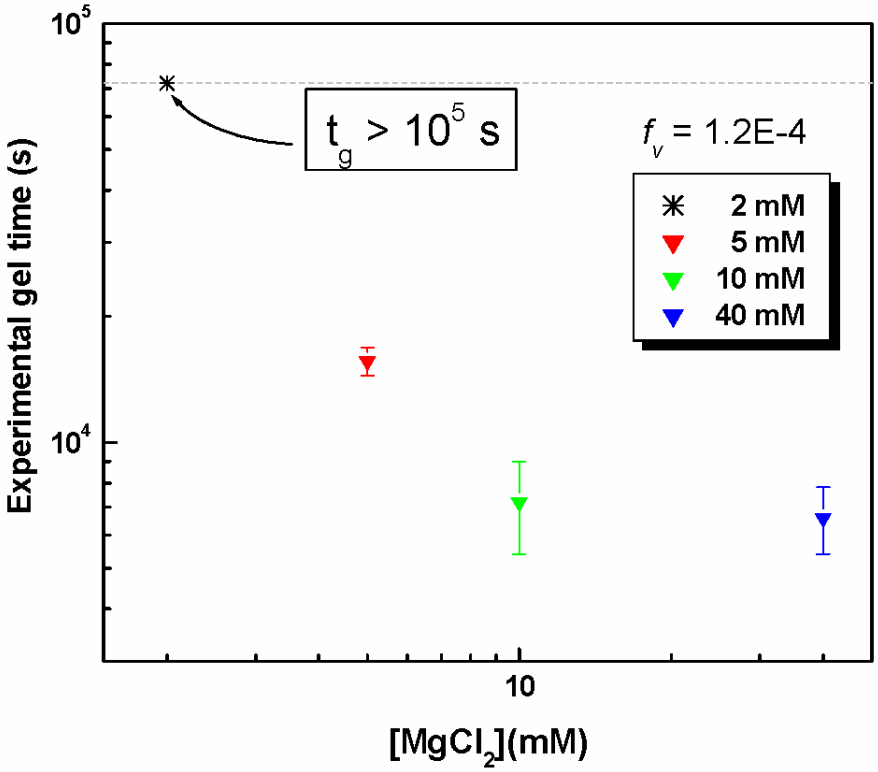

Figure 6.2 The gel time measurements (i.e., determined via SALS) versus the salt concentrations. The gel time is ca. constant at high salt concentrations increasing rapidly at lower salt concentrations.

In Fig. 6.3, the DLVO potential is plotted versus x (i.e., $x = r/\sigma$, and $\sigma = 20$ nm) for the above salt concentrations (i.e., 2, 5, 10, and 40mM). The ζ-potential of 30 mV was used to calculate the DLVO potential that is somewhat arbitrary, but in the range of the ζ-potential reported in the literature (Brinker & Scherer 1990). As shown in this figure, increasing the salt concentration further reduces the height of the repulsive potential barrier, and hence the aggregation is governed by a DLCA process.

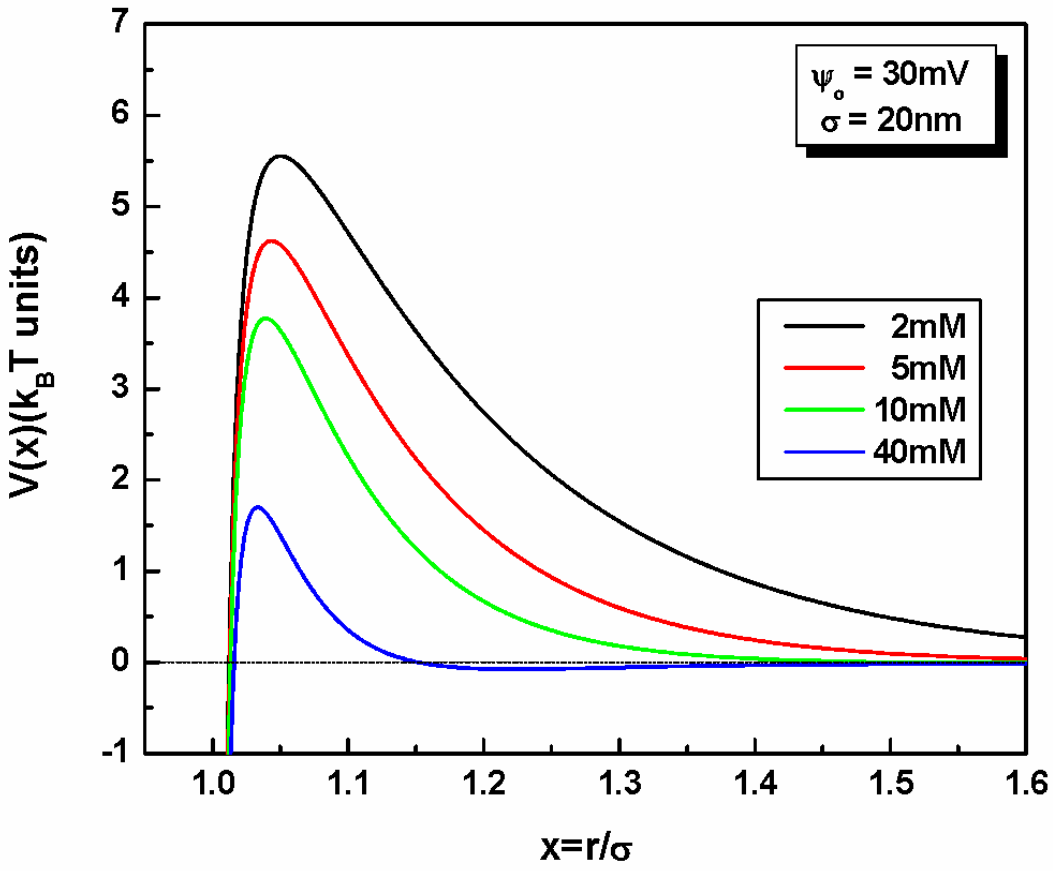

Figure 6.3 The DLVO potential is plotted versus x (i.e., $x = r/\sigma$) for various salt concentrations. The particle diameter is σ = 20 nm, and ψ_o = 30 mV. Increasing the salt concentration decreases the repulsive potential barrier further.

Figure 6.4 shows the scattered intensity $I(q)$ (arbitrary units) measurements versus the scattering wave vector, q (cm^{-1}) at various times (i.e., 7- 290 min) after the onset of aggregation. The final volume fraction of the polystyrene solution was 1.59E-4, and the final salt concentration was 10 mM. The first data, which was taken immediately (i.e., within a few seconds) after the onset of aggregation, is below 1E-4 on the intensity scale, and hence is negligible compared to the scattered light from the aggregating sample at later times. The first data was then subtracted from all subsequent measurements.

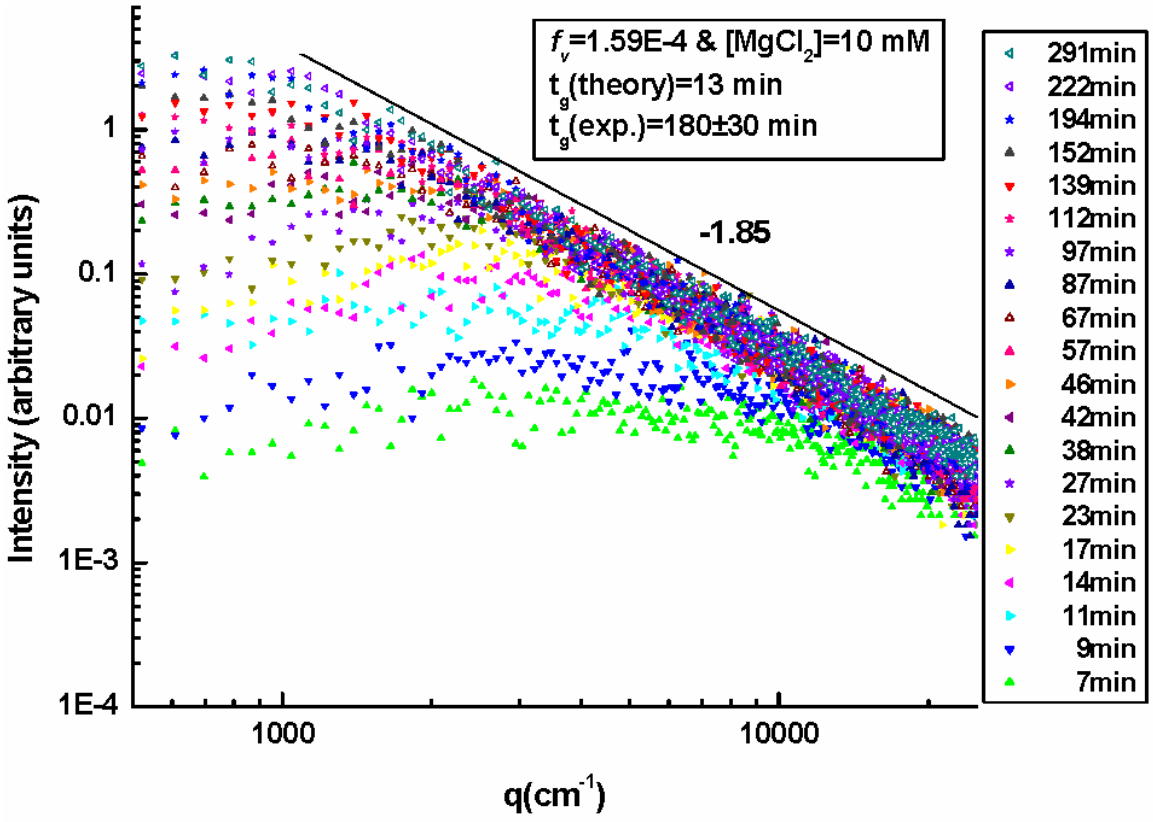

Figure 6.4 Static light scattering $I(q)$ versus the scattering wave vector $q(\mathrm{cm}^{-1})$ at different times after the onset of aggregation. The fractal dimension is 1.85 indicating the aggregation is in DLCA regime. The experimental gel time is ca. 180 ± 30 min. The theoretical gel time is 13 min.

There are several features, from light scattering point of view, that can be seen in Fig. 6.4.

(i) The scattered intensity at small q (i.e., Rayleigh regime) increases with time as $I \propto n_m N$, where n_m is the initial monomer number density (i.e. a constant), and N is the number of monomers per cluster. Therefore, the scattered intensity increases as the system aggregates (the number of monomers per cluster increases) which is referred to as the Tyndall effect.

(ii) The power law regime can yield the fractal dimension of the aggregating system if RDG conditions are satisfied (i.e., $2ka|m-1| << 1$, and $|m-1| << 1$, where n_2 (polystyrene) =1.59, n_1 (water) =1.33, $m = n_2 / n_1$, and $ka \sim 0.129$).

(iii) It can be seen that as aggregates become larger, the Guinier regime, where the slope of I versus q goes from 0 to negative, progresses to smaller q. One can qualitatively determine the size of the aggregates by using $R_g \sim q^{-1}$. Based on this approximate equation, the aggregates at the gel point are ca. 10 μm.

(iv) When light scattering intensity stops evolving further, it indicates that the aggregates have reached to a critical size at which they have spanned the entire system, and hence the system is gelled. From this perspective, the experimental gel time can be obtained, and compared with the theoretical gel time.

(v) There is an apparent peak in $I(q)$ versus q. A peak appears in the structure factor ($S(q) \propto I(q)$) of dense aggregating colloidal systems when the aggregates radius of gyration, R_g becomes comparable in magnitude to the mean nearest neighbor separations of the aggregates, R_{nn}. It has been shown, by our group, that the appearance of this peak is an artifact (Cerda et al 2004, Huang et al 1998), and its position on the q scale does not represent a true characteristic length scale of the system as have been suggested in literature (Carpineti & Giglio 1992, Gonzalez & Ramirezsantiago 1995, Poulin et al 1999).

The sample gelled, based on the definition of a gel in our work, within 180 ± 30 min. The fractal dimension of aggregating system is ca. 1.85 indicating that the aggregation is in the DLCA regime. We then used Eq. (4.49) to calculated the theoretical gel time which is ca. 13min if D_f = 1.8 is used, and 31 min if D_f = 1.85 is used instead. However, in order to be consistent in our interpretation of the results, any variation up to 0.05 in the slope was not considered in the calculation. In this experiment, a discrepancy can be seen between the calculated and experimental gel time. Therefore, the volume fraction was lowered, and the salt concentration was kept the same as above. Then the same light scattering measurements were performed in

order to determine the experimental gel time. The whole process of preparation and experiments in each run tried to be kept as consistent as possible.

Figure 6.5 shows the scattered light intensity versus $q(cm^{-1})$ for the lowest volume fraction, f_v = 3.63E-5 in this set of experiments. As can be seen in Fig. 6.5, the experimental gel time is 480±50 min, and the theoretical gel time is 514 min. For this volume fraction, there is a good agreement between the experimental and theoretical gel time.

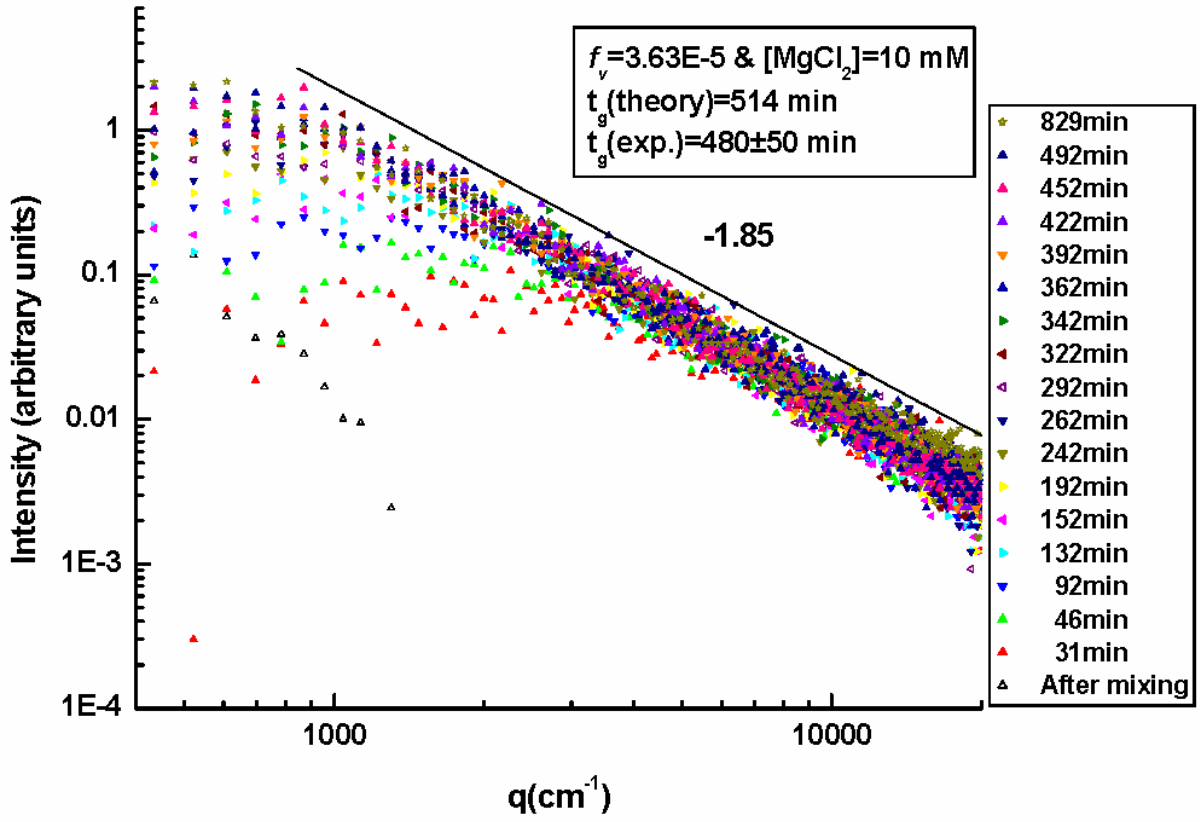

Figure 6.5 Static light scattering $I(q)$ versus the scattering wave vector $q(\mathrm{cm}^{-1})$ at different times after the onset of aggregation. The fractal dimension is 1.85 indicating the aggregation is in DLCA regime. The experimental gel time is ca. 480 ± 50 min. The theoretical gel time is 514 min.

Figures 6.6 to 6.9 show a series of light scattering measurements performed for various volume fractions, i.e., lower to higher, respectively. One can see that as the volume fraction increases the agreement between the experimental and the theoretical gel times become worse. Each graph is self-explanatory based on the light scattering descriptions given above.

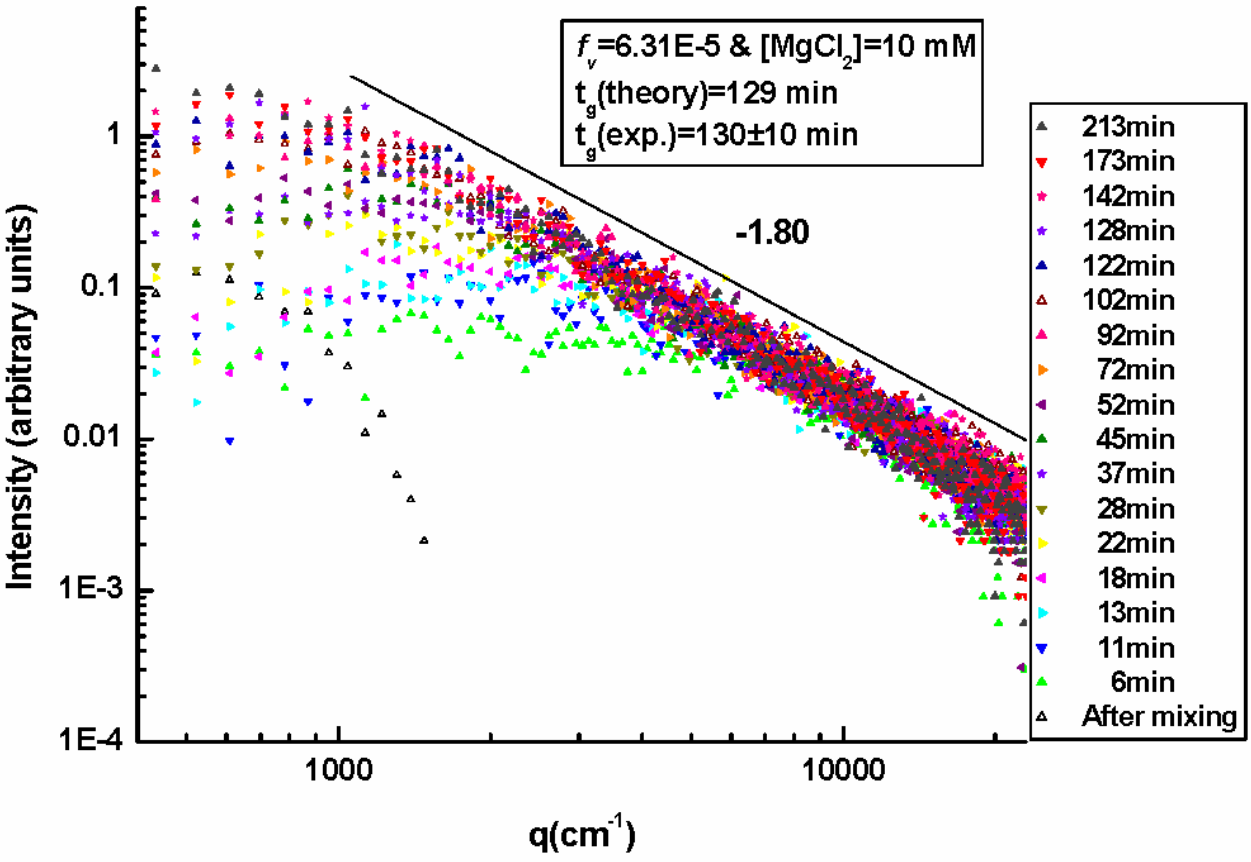

Figure 6.6 Static light scattering $I(q)$ versus the scattering wave vector $q(\mathrm{cm}^{-1})$ at different times after the onset of aggregation. The fractal dimension is 1.80 indicating the aggregation is in DLCA regime. The experimental gel time is ca. 130 ± 10 min. The theoretical gel time is 129 min.

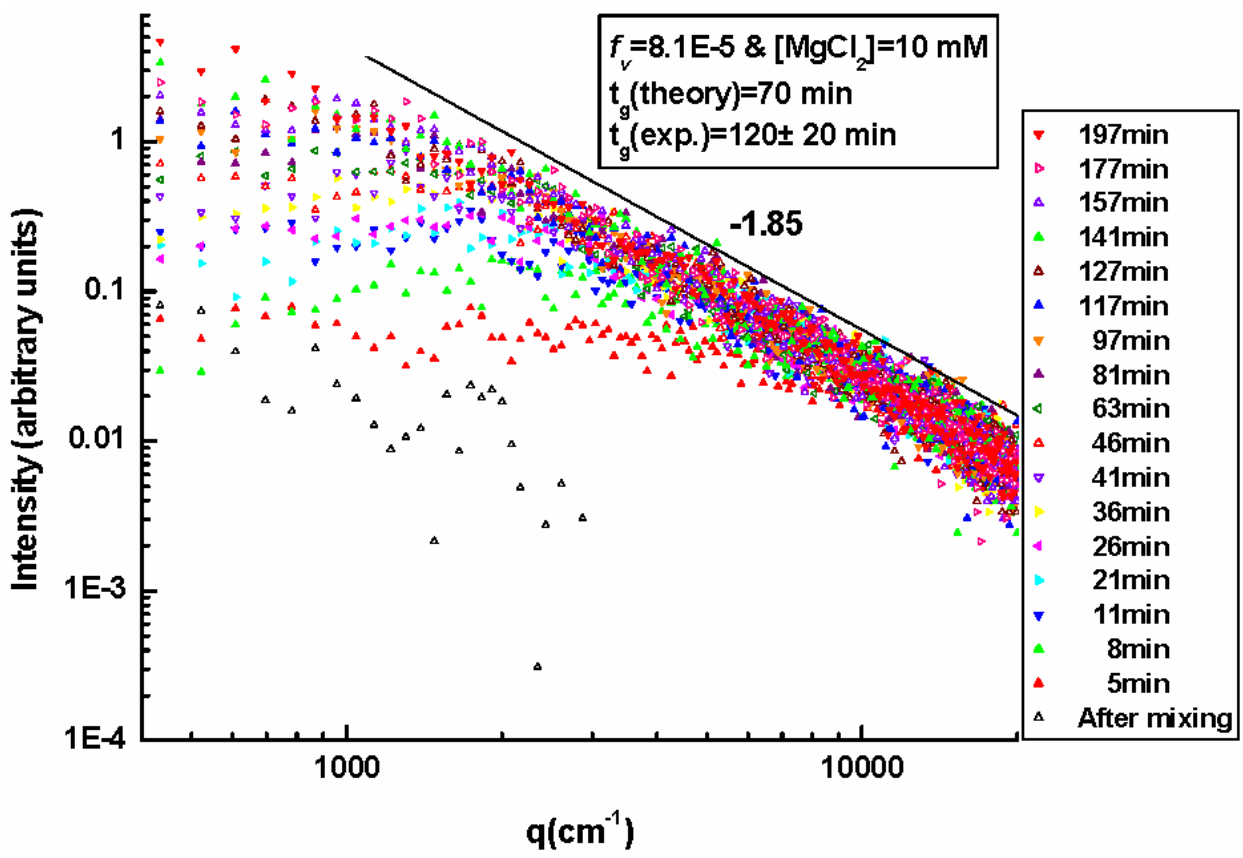

Figure 6.7 Static light scattering $I(q)$ versus the scattering wave vector $q(\mathrm{cm}^{-1})$ at different times after the onset of aggregation. The fractal dimension is 1.85 indicating the aggregation is in DLCA regime. The experimental gel time is ca. 120 ± 20 min. The theoretical gel time is 70 min.

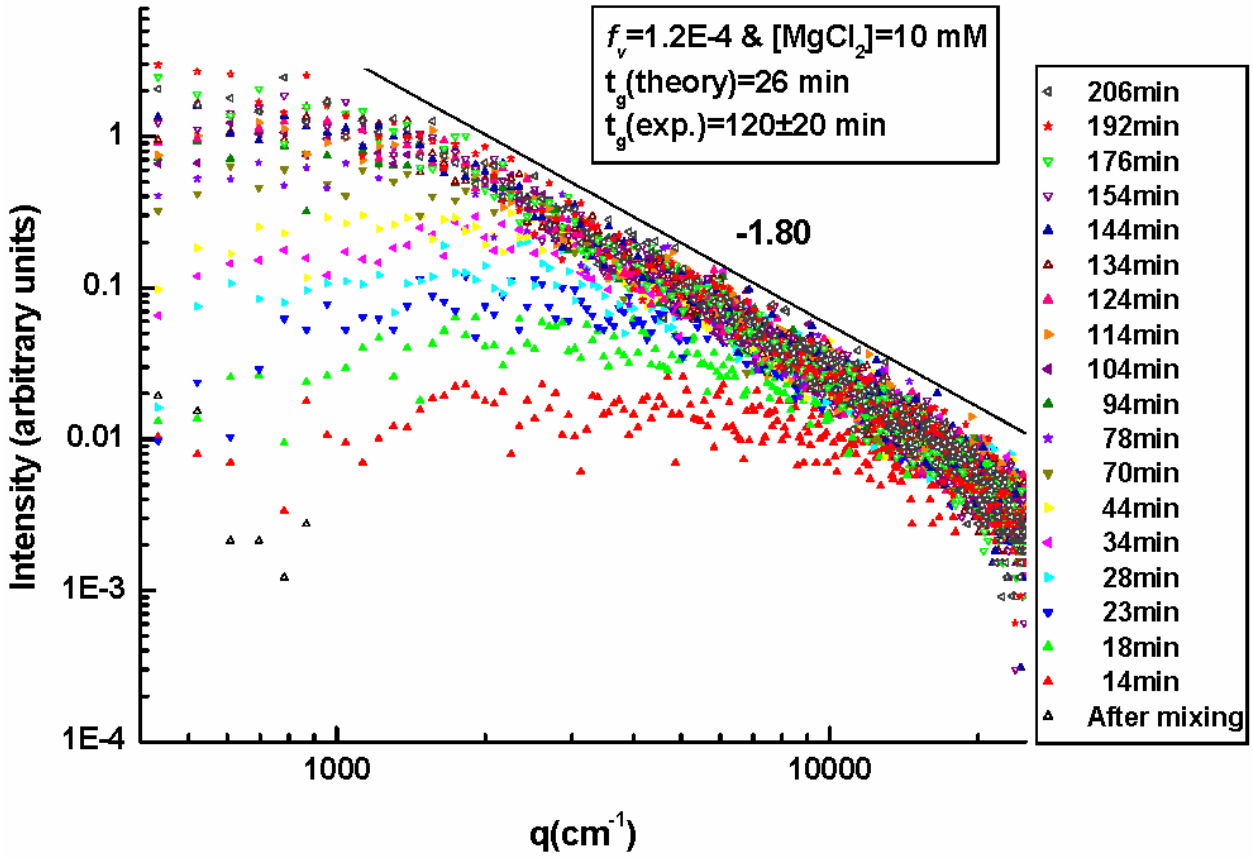

Figure 6.8 Static light scattering $I(q)$ versus the scattering wave vector $q(\mathrm{cm}^{-1})$ at different times after the onset of aggregation. The fractal dimension is 1.80 indicating the aggregation is in DLCA regime. The experimental gel time is ca. 120 ± 20 min. The theoretical gel time is 26 min.

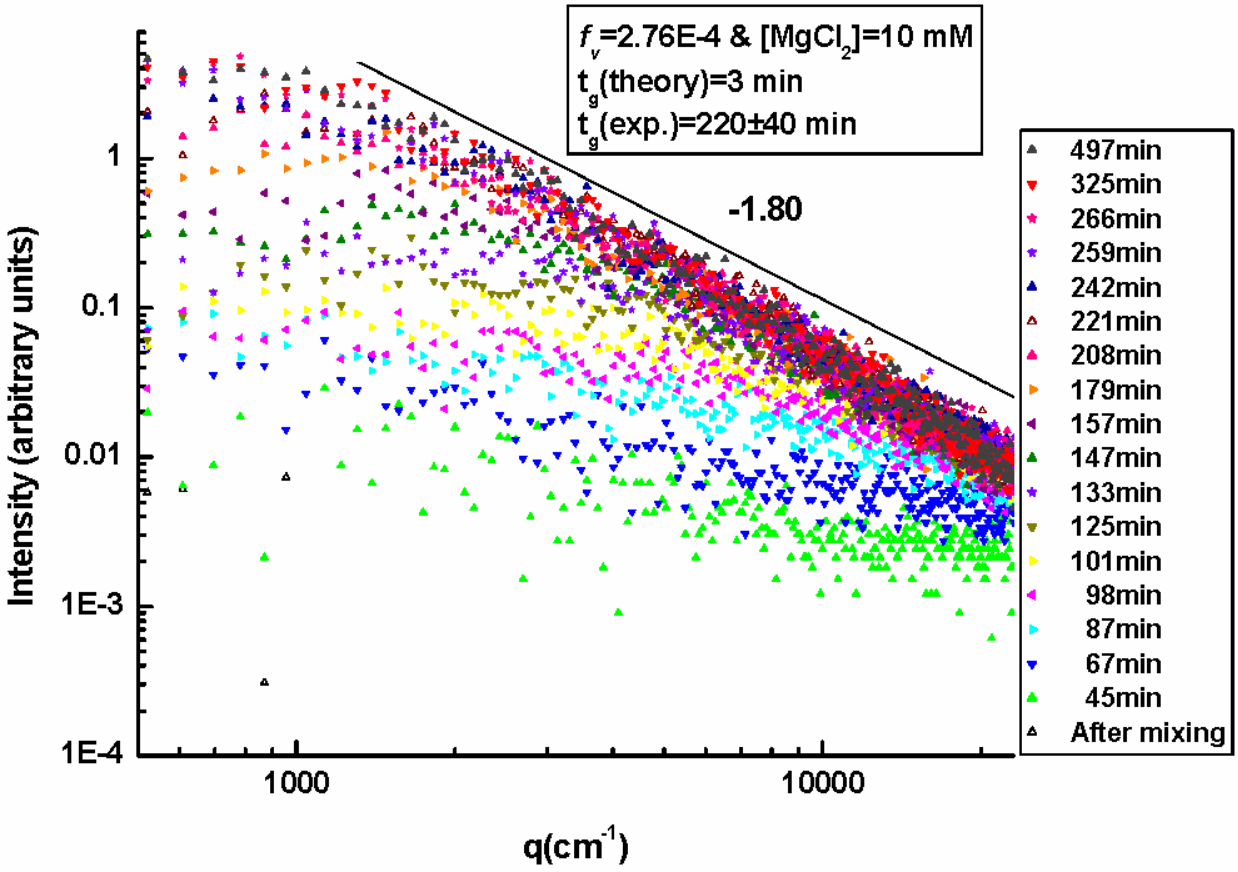

Figure 6.9 Static light scattering $I(q)$ versus the scattering wave vector $q(\mathrm{cm}^{-1})$ at different times after the onset of aggregation. The fractal dimension is 1.80 indicating the aggregation is in DLCA regime. The experimental gel time is ca. 220 ± 40 min. The theoretical gel time is 3 min.

In Fig. 6.10, the experimental gel time (sec) (i.e., determined by using SALS) and the theoretical gel time (sec) (i.e., calculated using Eq. (4.49)) are plotted versus various volume fractions of polystyrene colloidal dispersions ($a = 10\,\mathrm{nm}$) ranging between $3.63\times10^{-5} \le f_v \le 2.76\times10^{-4}$. The final salt concentration was 10 mM. In the inset figure, the theoretical characteristic time $t_c(s)$, the gel time $t_g(s)$, and the initial mixing time $t_{mixing}(s) \sim 1s$ are plotted versus the volume fractions given above.

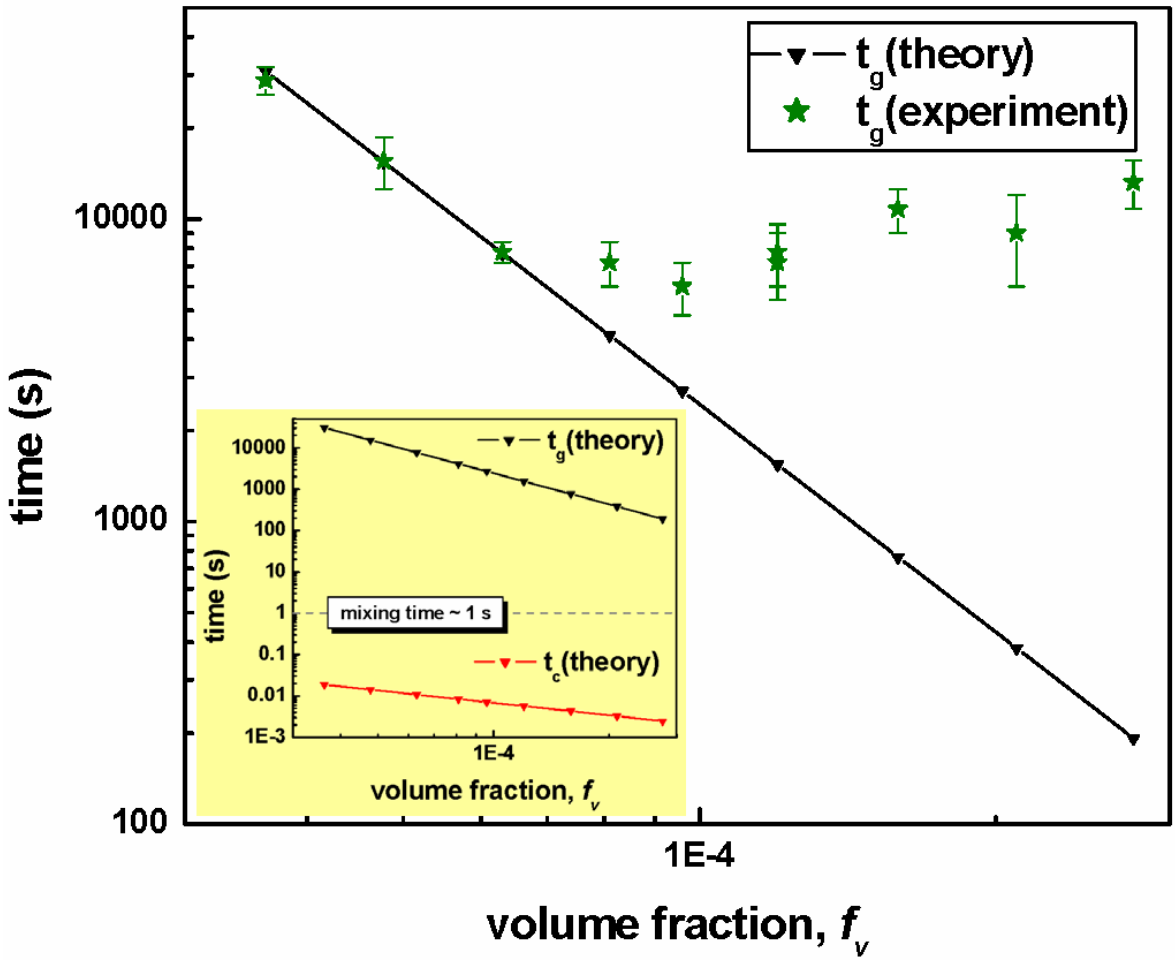

Figure 6.10 The theoretical and experimental gel times versus various volume fractions. The inset graph shows the theoretical gel time and characteristic time. Initial mixing time is also plotted in the inset graph which is the time (i.e., approximately one second) needed to stir the sample.

As can be seen in Fig. 6.10, the experimental gel time at low volume fractions agrees well with the theoretical gel time. However, by increasing the volume fractions, the agreement between theory and experiment gradually diminishes, and at highest volume fraction, the experimental gel time is almost 100 times longer than the predicted theoretical gel time. However, as can be seen in Fig. 6.10, the experimental gel times at high volume fractions are more or less similar. What is going on?

One may propose that the aggregation may not be in a pure DLCA regime causing a longer experimental gel time compared to the theory. This scenario is not justified, because if the aggregation process is in the RLCA regime, the gel time should be longer at all volume fractions in this experiment. On the other hand, it can be seen in Fig. 6.10 that the experimental gel time is in fact in good agreement with the theory at low volume fractions.

To our knowledge, this kind of comparison between theoretical and experimental gel time have been only made in the RLCA regime using silica colloidal particles (Bremer et al 1995, Smith & Zukoski 2006). Moreover, the calculated theoretical gel time of the DLCA experiments of other works (Carpineti & Giglio 1992, Cipelletti et al 2000) show similar behavior as our work (i.e., theoretical gel time at high volume fraction is much faster than the experimental gel time). The volume fraction of the polystyrene (radius of 10 nm) solutions used in their experiments were 2.96E-4 (Carpineti & Giglio 1992) and 4.8E-4 (Cipelletti et al 2000); $MgCl_2$ salt was used in both experiments to induce the aggregation.

A scaling argument has been proposed by our group in order to understand the discrepancy between the theoretical and experimental gel time at high volume fractions. We should note here that this scenario has not been tested yet, but so far is the only reasonable qualitative approach to understand the data shown in Fig. 6.10.

Equation (4.50) (i.e., $t_g \propto a^3 f_v^{-2.5}$, where $D_f = 1.8$) can be written in terms of the "monomer" number density as

$$t_g \propto a^3 (n_m a^3)^{-2.5} \propto n_m^{-2.5} a^{-4.5}, \tag{6.1}$$

Now let's assume that there are some kind of small perturbations (e.g., initial mixing), for a very short period of time, in an aggregating system immediately after the onset of aggregation. If the characteristic time is longer than the initial mixing time, the initial mixing would not affect the aggregation rate. However, if the characteristic time is less than the initial mixing time

($t_c << t_{mixing}$), then by the time the unstable sample is being mixed, the monomers are aggregating to form dimers, trimers, tetramers, and finally N-mers. Depending on the duration of initial mixing, one can approximately determine the number of monomers in these small clusters, N. Hence the size of these small aggregates a' can be determined by using Eq. (4.47), i.e.,

$$a' \propto a\, N^{1/\mathrm{D}}, \tag{6.2}$$

where D is the fractal dimension of these small aggregates (i.e., formed during initial mixing). D could be different than $\mathrm{D_f}$ (i.e., the fractal dimension of the aggregated system at the gel point) depending on the initial mixing time, the volume fraction, and the rate of initial mixing. The number of these small aggregates in the system (i.e., "new" monomer number density) can be obtained using Eq. (4.38) (i.e., $n_c = n_m / N$). Therefore, the new gel time t_g' can be rewritten as

$$t_g' \propto n_c^{-2.5} a'^{-4.5} \propto n_m^{-2.5} N^{2.5} a'^{-4.5}. \tag{6.3}$$

Equation (6.2) can be substituted into Eq. (6.3) to give

$$t_g' \propto n_m^{-2.5} N^{2.5} a^{-4.5} N^{-4.5/D}, \tag{6.4}$$

where in Eq. (6.4), t_g' can be written in terms of t_g (i.e., the gel time of an unperturbed system) as

$$t_g' \propto t_g\, N^{2.5} N^{-4.5/D}. \tag{6.5}$$

The new gel time given in Eq. (6.5) can now be considered for two different conditions, i.e.

At low volume fractions: Initial mixing forms small fractal aggregates with $D = 1.8$. Therefore, by using $D = 1.8$ in Eq. (6.5), the new gel time is

$$t_g' \propto t_g N^{2.5} N^{-2.5} \propto t_g. \tag{6.6}$$

This is consistent with the results shown in Fig. 6.10 that at low volume fractions, the experimental and theoretical gel time are in good agreements.

At high volume fractions: Initial mixing forms compact aggregates with $D = 3$. Therefore, by using $D = 3$ in Eq. (6.5), the new gel time is

$$t_g' \propto t_g N^{2.5} N^{-1.5} \propto t_g N, \tag{6.7}$$

where

$$N = t_{mixing} / t_c. \tag{6.8}$$

Now substituting Eq. (4.48) (i.e., $t_g = N_G t_c$) into Eq. (6.8) yields

$$N = N_G t_{mixing} / t_g, \tag{6.9}$$

where $N_G t_{mixing}$ can approximately be considered as a constant, and hence $N \propto 1/t_g$. Therefore,

$$t_g' \propto t_g (1/t_g) \propto \text{constant}. \tag{6.10}$$

Again, this result is consistent with the results shown in Fig 6.10 that the gel time at high volume fractions are approximately constant. However, this scaling argument would not yield the correct experimental gel time, and this remains unsolved up to this point. Therefore, more experiments are needed to understand the effect of initial mixing on an aggregating system.

6.3 Conclusions

Our SALS gel time measurements showed good agreements between the theoretical and the experimental gel times only at low volume fractions of the polystyrene particles. As the volume fraction of the polystyrene solution increased to higher values, the difference between theoretical and experimental gel times became significantly large. A scaling argument was proposed to explain this discrepancy between the theoretical and experimental gel times. It was proposed that the initial mixing time of the colloidal solution with the salt in a DLCA regime is essentially important in affecting the aggregation rate.

6.4 Recommendations for Future Work

In order to further investigate the effect of initial mixing on the aggregation rate and gelation, a family of curves, an example is shown in Fig. 6.11, can be obtained by the following experiments.

(i) The characteristic time can be increased, especially at high volume fractions, and an example of which is shown in Fig. 6.11, curve 3.

   a To slow down the aggregation rate by decreasing the salt concentration, where the aggregation is in the RLCA regime (i.e., $t_c(RLCA) = t_c(DLCA)W$). This is particularly important at high volume fractions in which initial mixing time can drastically affect the aggregation rate (e.g., see Fig. 6.10).

   b To increase the viscosity of the dispersion medium, and hence increase the characteristic time ($t_c \propto \eta$). This can be done by using, for example, glycerol in which its viscosity is 1000 time more than that of water. One other advantage of glycerol is that its refractive index (n_{glycerol}=1.47) is close to that of polystyrene (n_{ps}=1.59), and hence multiple scattering would be less problematic (Hoekstra et al 2003, Kikuchi et al 2005, Lumma et al 2000, Torres et al 1991a).

(ii) The initial mixing time can be increased at low volume fractions to obtain curve (1) as shown in Fig. 6.11.

(iii) To increase the particle size, and hence to increase the characteristic time (i.e., $t_c \propto a^3$). However, as mentioned earlier, multiple scattering can become troublesome with large particle sizes, and thus there is an upper limit to flexibility of this method. Therefore, for SALS purposes, an increase up to twice as large as the previous experiment (diameter 20 nm) is suggested.

It is important to note that there are certainly some constraining limits to the flexibility of the experiments suggested above. Here we only addressed a few of those such as multiple scattering at large particle sizes, very long gel times at large particle sizes, and/or low volume fractions. Therefore, some preliminary experiments are required before further pursuing any systematic and extensive experiments to investigate the effect of initial mixing on gelation

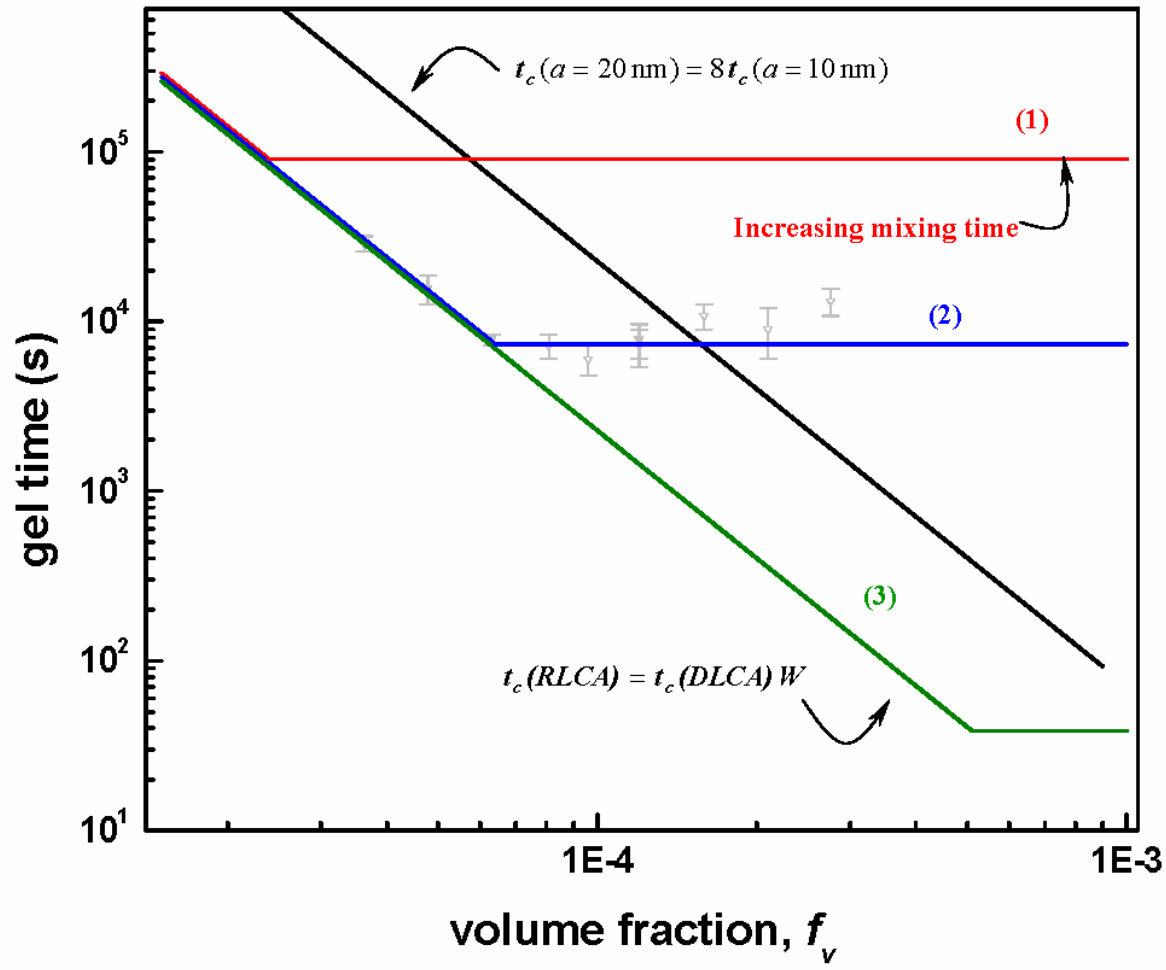

Figure 6.11 A schematic family of curves is shown for the gel time versus the volume fractions. Curve (1) (i.e., red curve) suggests that if an unstable aggregating colloidal solution is initially mixed for longer times, the initial mixing itself would induce the gelation. Curve (2) is similar to the curve shown in Fig. 6.10 for which the gel time experiments were performed. However, this curve can be extended by more experiments at lower volume fractions. Curve (3) is particularly important at higher volume fractions in which initial mixing can affect the aggregation rate drastically. Curve 3 can be obtained by performing the experiments in RLCA regime. The back line shows the gel time for the 20 nm in radius colloids. The gray hollow triangles are the experimental gel times from Fig. 6.10.

CHAPTER 7 SALS Studies of the Effects of Shear on Colloidal Aggregation and Gelation

7.1 Introduction

Many experimental and theoretical studies have been carried out to investigate the effect of shear flow on the kinetics of aggregation, the resulting size distributions, and the structures of particle aggregates.

Shear can promote aggregation of colloidal particles by either increasing the rate in an unstable dispersion or mechanically destabilizing a dispersion resistant to Brownian aggregation. In the former situation, the degree of enhancement depends primarily on the rate of collisions due to shear relative to those from diffusion alone, as reflected by Péclet number (Russel et al 1999).

An aggregate subjected to stress may undergo structural revision in two ways and possibly with a combination of the two mechanisms. If there is a weak bond in the structure, it may fracture and break apart, recombining with the same or another aggregate under more favorable conditions (forming bonds at more than a few sites) (Flesch et al 1999). If the weak points can withstand the stress, then part of the aggregates can rotate and form more bonds within itself, becoming more compact in the process (Lin et al 1990a, Selomulya et al 2002). The former revision is known as a fragmentation-reaggregation process and the latter as restructuring.

7.2 Literature Review

A brief overview of the shear experiments in the literature is given below. We then discuss these results later in more detail (e.g., the fractal dimension of the fractal aggregates and the mechanisms by which these aggregates have formed, i.e., restructuring, fragmentation, or a combination of both).

In order to study shear, various types of shear cells are used for this purpose such as

(i) The Couette flow cell which can be a two concentric-cylinder system with an inner cylinder rotating while the outer cylinder is at stationary (Wang et al 2005) or vice versa (Zeichner & Schowalter 1979). Some of these Couette cells are designed such that *in situ* measurements can be performed using static light scattering technique (Clarke et al 1995, Hashimoto et al 1986, Varadan & Solomon 2001, Weber & Schosseler 2002).

(ii) A parallel plate shear cell with a continuous rotation (Clarke et al 1995, Kikuchi et al 2005) or an oscillatory rotation (Yan et al 1994).

(iii) Using stirred tanks is another type of shear cell which is useful especially because of its industrial applications (Flesch et al 1999, Spicer et al 1996).

The colloidal dispersion and the salt solution are prepared with the desired concentrations which are then mixed.

(i) The unstable colloidal solutions are then immediately subjected to shear until a stable aggregate size is reached in the system (Kikuchi et al 2005, Oles 1992, Selomulya et al 2002, Serra & Casamitjana 1998, Serra et al 1997, Torres et al 1991a, Wang et al 2005).

(ii) The system is allowed to aggregate for a period of days, and then the shear is applied in short impulses, which would subsequently increase, to the aggregated system (Sonntag & Russel 1986).

(iii) The colloidal system is allowed to aggregate and reach to a certain size (500nm). The shear is then applied for 0.5 second (Lin et al 1990a, Lindsay et al 1987).

The particle sizes (diameter σ) used have been

(i) $\sigma < 50$ nm (Lin et al 1990a, Lindsay et al 1987).

(ii) 50 nm $< \sigma <$ 100 nm (Selomulya et al 2002, Torres et al 1991a).

(iii) 0.1 μm $< \sigma <$ 1 μm (Flesch et al 1999, Selomulya et al 2002, Sonntag & Russel 1986).

(iv) $1\ \mu m < \sigma < 5\ \mu m$ (Kikuchi et al 2005, Oles 1992, Serra & Casamitjana 1998, Serra et al 1997).

(v) $\sigma \sim 10\ \mu m$ (Wang et al 2005).

Finally, the shear rates in these experiments are

(i) $\gamma < 10\ sec^{-1}$ (Wang et al 2005).

(ii) $10\ sec^{-1} < \gamma < 150\ sec^{-1}$ (Kikuchi et al 2005, Oles 1992, Selomulya et al 2002, Serra & Casamitjana 1998, Serra et al 1997).

(iii) $\gamma > 500\ sec^{-1}$ (Lin et al 1990a, Lindsay et al 1987, Sonntag & Russel 1986, Torres et al 1991a).

The parameters of the shear experiments listed above hopefully would facilitate a quick reference to the shear experiments reviewed in this chapter. In addition, as we talk about our experiments later, one can see where our work stands compared to the shear experiments in the literature. However, certainly in all the experiments listed above, the Péclet number have been much larger than one to ensure that the aggregation in these systems is governed by the shear aggregation compared to the Brownian aggregation.

Sonntag and Russel (Sonntag & Russel 1986) examined the aggregation in shear flow (γ = **1500-6000 sec^{-1}**) of diluted suspension of polystyrene latexes in a Couette flow cell using static light scattering technique. In their experiments polystyrene (**140 nm** in diameter) dispersion was prepared in a mixture of glycerol and water. Glycerol was used to slow down the characteristic time to allow sufficient time for mixing, shearing, and sampling. The addition of **NaCl** salt to the polystyrene solution brought the ionic strength to $\mathbf{0.4}\,\boldsymbol{M}$ and the volume fraction to $f_v = 7.4 \times 10^{-3}$. The system was then allowed to aggregate for a period of days. To ensure a uniform starting point for their experiments, the aggregation was allowed to continue until the latex separated from the suspending medium. The suspensions were then subjected to short impulses of know shear rate, in order to minimize the effect of aggregate-aggregate collisions, causing an instantaneous **fragmentation**. Then subsequent impulses of greater shear rate were

applied which would progressively reduce the aggregate size in accord with the increasing maximum shear rate. At desired intervals during the shear history, the Couette cell was stopped, and a sample was extracted and transferred into a scattering cell for light scattering measurements. The fractal dimension of the aggregates was $\mathbf{D_f = 2.48}$ when the samples were sheared at two widely different shear rates.

Torres, Russel, and Schowalter (Torres et al 1991a), similar to the experiment described above, used a mixture of glycerol/water for both salt and polystyrene solutions. The shear experiments were carried out using a Couette shear cell at $f_v = 1 \times 10^{-6}$ of polystyrene **98 nm** and a **NaCl** salt concentration of $\mathbf{1}\,M$. After mixing the polystyrene and the salt solutions, the sample was immediately transferred into a shear cell. The unstable sample was then subjected to a shear (γ **= 780-1590** $\mathbf{sec^{-1}}$) for shearing times between **5** and **30 min**. After shearing for a predetermined time, they removed a sample and transferred it into a light scattering cell for static light scattering measurements (the scattering angles ranging between $12^o - 160^o$)[18]. They found $\mathbf{D_f = 1.8}$ for the sheared samples regardless of the shear rates; their static light scattering measurements for Brownian and shear aggregation were indistinguishable. Further, their dynamic light scattering (DLS) measurements showed that the aggregation growth rate in a sheared sample was much faster than the Brownian aggregation. Their DLS measurements showed that the aggregates grew due to shear until they reached a maximum size; this maximum size would depend on the shear rate (i.e., smallest for the highest shear rates). Initially they considered two possibilities of restructuring and fragmentation of the aggregates due to shear; however, their DLS measurements did not show slow kinetics. Therefore, they concluded that restructuring of the aggregates did not occur in their experiments (because restructuring would yield more compact aggregates, and hence would slow the kinetics accordingly) and **fragmentation** was the most likely mechanism happening in their shear experiments. This group, based on the following argument, presented an approximated breakup criterion. They

---

[18] Note that the largest aggregate size that could be probed in their light scattering setup was about 300 nm; thus, if the aggregates had a different structure, it could not be detected with their light scattering setup.

proposed that fragmentation occurred when the hydrodynamic force pulling the aggregates apart exceeded the attractive forces. Furthermore, by assuming that two aggregates (i and j) joined at one particle-particle bond, they showed[19] that

$$(R_{h,i} + \mathrm{R_{h,j}}) \le (\frac{a\,A_H}{18\pi\eta\gamma\delta^2})^{1/2}, \tag{7.1}$$

where A_H is the Hamaker constant, R_h is the hydrodynamic radius of the aggregates (R_h is defined as the radius of a sphere having the same Stokes drag as the given aggregate, and $R_h / R_g = 0.875$), δ is a value that corresponds to length scales at which molecular structure, roughness, etc., become important and can be approximated to 1 nm. Hierarchical simulations performed by the same group (Torres et al 1991b) supported their experimental results for flow-induced cluster-cluster aggregation in which rigid bonds form at contact.

Oles (Oles 1992) carried out aggregation experiments in a laminar shear Couette apparatus ($\boldsymbol{\gamma}$**= 25-150 sec**$^{-1}$) using **NaCl=1.16** $\boldsymbol{M}$ to destabilize a monodisperse suspension of polystyrene particles of **2.17 μm** with a final $\boldsymbol{f_v = 10^{-6}}$ and $\boldsymbol{f_v = 5\times 10^{-6}}$. The unstable system was transferred into the shear cell within 4-5 minutes. To monitor the dynamics of the size distribution, continuous samples were taken from the Couette-flow system with a system of plastic tubing. The samples passed through the optical cell of a particle sizer and were pumped back into the Couette-flow system. Similar to the above experiments, the particle aggregated due to shear, and the aggregation slowed down and a stable aggregate size was reached. Oles found that high shear leaded to an increase in the aggregation rate and to a decrease of the equilibrium size. The fractal dimension of the aggregates in the initial growth phase was 2.1, changing to $\mathbf{D_f = 2.5}$ in later stages of the aggregation. He proposed that the initial fractal dimension of $\mathbf{D_f = 2.1}$ was due to restructuring of the aggregates in the shear field and the further increase in

[19] Zeichner and Schowalter have shown that the Hamaker constant for both fast aggregation and fast shear induced aggregation is similar, i.e., $A_H \sim 2\times 10^{-21}$ J.

the fractal dimension ($D_f = 2.5$) was due to a preferred **fragmentation** of weak parts of the clusters. Furthermore, his results show that the fractal dimension is independent of the shear rates examined in their experiments.

Serra and Casamitjana (Serra & Casamitjana 1998) studied the aggregation and breakup behaviors of particles in a laminar Couette flow apparatus (γ **=25, 32, and 50 sec^{-1}**). Suspensions of latex particles of **2 μm** were prepared in **1.29** M NaCl at volume fraction of $f_v = 5 \times 10^{-5}$. Similar to Oles's work, the samples were taken from the Couette cell into a scattering cell for measurements by using tubes, pumped back into the Couette system after the measurements. The fractal dimension of the aggregates in the initial stage of growth was $D_f = 1.8$. The fractal dimension of the aggregates after reaching the equilibrium size was $\mathbf{D_f = 2.24 \pm 0.22}$. This fractal dimension was independent of the shear rates. They found that the aspect ratio of the aggregates did not change during the aggregation process, which seemed to be in accordance with the fact that there was no change in the structure of the aggregates. Therefore, they concluded that there was no restructuring in the process, and instead **fragmentation** was the only mechanism impeding further growth of the aggregates. Serra, Colomer, and Casamitjana (Serra et al 1997) carried out similar experiments in both laminar and turbulent regime (**γ=25-195 sec^{-1}**) and found that shear-induced fragmentation was the pronounced mechanism in their shear experiments.

Kikuchi et al. (Kikuchi et al 2005) studied aggregation and breakup behaviors of latex particles in shear flow confined between two parallel plates using laser scanning confocal microscope (CLSM). The distance between two plates was ranging between 30 and 100 μm. The shear rates were from **20 to 80 sec^{-1}**. A suspension of polystyrene latex particles of **2 μm** diameter was used in all the experiments with a final volume fraction of $\mathbf{2 \times 10^{-3}}$ or $\mathbf{4 \times 10^{-3}}$. The salt concentration (**NaCl**) was **0.2 M**. In their experiments, the aggregation was initially dominant in the early stage of shearing. However, at later stage of shearing, **fragmentation** and aggregation became equally significant, and thus the steady state was maintained. The perimeter based fractal dimension D_p was determined via image analysis of their CLSM measurements.

The perimeter based fractal dimension was found to be independent of the shear rate and the gap width between two plates in their experiments $\mathbf{D_p = 1.2}$ [20].

Flesch, Spicer, and Pratsinis (Flesch et al 1999) carried out aggregation experiments of a polystyrene particle/$Al(OH)_3$/water system in a stirred tank. The volume fraction of the polystyrene particle (diameter of **870 nm**) was $\mathbf{1.4 \times 10^{-5}}$**.** The salt (i.e., $\mathbf{Al_2(SO_4)_3}$) was added to the polystyrene suspension and mixed with the suspension and then the impeller was set to the desired speed. The average shear rates in their experiment were $\boldsymbol{\gamma}$**= 50, 100, and 150 sec^{-1}**. During the shear aggregation experiment, samples were taken, at different times, from the tank into a particle sizer (light scattering set up, Malvern instruments) using a syringe. The particles aggregated initially due to shear, but then reached a steady state at which the aggregate size did not increase further. The fractal dimension characterizing the aggregate structure was independent of shear rates in their experiment, i.e., $\mathbf{D_f = 2.05 \pm 0.05}$. In order to have an agreement between their experimental results and the Smoluchowski's theory for shear aggregation, the **fragmentation** needed to be considered in the theory. In another study, Spicer, Keller, and Pratsinis (Spicer et al 1996) had investigated the effects of impeller type and the average shear rates of $\boldsymbol{\gamma}$**= 15, 25, and 50 sec^{-1}** on aggregate size and their structure during the shear-induced aggregation. An optical microscope equipped with video camera was used to determine the perimeter-based fractal dimension D_p in their experiments. They found that the evolution of the perimeter-based fractal dimension D_p (from the beginning of the shear until the system reached steady state in terms of aggregate size and fractal dimension) was not influenced by impeller type at γ= 15, 25 sec^{-1}. However, at $\gamma = 50$ sec^{-1} a maximum in D_p was observed prior to attainment of steady state for the axial flow impellers as a result of "restructuring"; however, **fragmentation** decreased $\mathbf{D_p \approx 1.3}$ (i.e., $\mathbf{D_f \approx 2.55}$) at later times. The fractal dimension of the aggregates remained more or less within D_p =1.23-1.33 (less than 8%

[20] Using the formula given earlier (i.e., $D_p = 1 + (3 - D_f)^{3/2}$, for $D_f > 2$), the mass fractal dimension is calculated to be D_f =2.66.

variation) during shearing as shown in Fig 8C in their paper (Spicer et al 1996). Therefore, it is more logical to consider the restructuring of the aggregates within the uncertainty of their experiments. Also, it should be pointed that this group obtained more compact aggregates for $\gamma < 50\ \text{sec}^{-1}$ (i.e., $D_f \approx 2.55$) than that for $\gamma = 50 - 150\ \text{sec}^{-1}$ (i.e., $D_f \approx 2.05$).

Wang et al. (Wang et al 2005) performed an experimental and computational investigation on the effect of local fluid shear rate in the aggregation and fragmentation of an aqueous dispersion of **9.6 μm** latex spheres undergoing laminar shear flow in a Couette cell. Polystyrene suspension $\boldsymbol{f_v = 4 \times 10^{-2}}$ was then mixed with **NaCl** salt so that the concentration of NaCl in the resulting suspension was **1.29 M** .The shear rates were ($\boldsymbol{\gamma}$**= 2.20, 4.49, and 6.74** $\textbf{sec}^{-1}$). The unstable sample was transferred to the Couette cell and the shear was set to the desired rate. A progressive scan monochrome CCD camera was used to capture images in their experiments. They found that that the perimeter fractal dimension of the aggregates (i.e., obtained from the image analysis) initially increased and at later times, D_p decreased as **fragmentation** became significant and broke apart the aggregates. However, they observed that even as the mean aggregate size reached a plateau (fragmentation and aggregation become both significant), the perimeter-based fractal dimension decreased. Therefore, they suggested that even after aggregates stopped growing, they undergo a "breakup-induced restructuring" process so that they become more compact. Furthermore, they found that D_p decreased with increasing mean shear rate (indicating that the mass fractal dimension increased with increasing the shear rate). However, based on the graph shown in their paper (Fig. 16 in their paper), D_p is in the range between 1.15 and 1.25 (i.e., $D_f \approx 2.6$-2.7) throughout their shear experiments. Hence their interpretations regarding the "breakup-induced restructuring" mechanism and their statement on having more compact aggregates with higher shear rates should be considered with care.

Lin et al. and Lindsay et al. (Lin et al 1990a, Lindsay et al 1987) performed an experiment with colloidal **gold** (diameter of **15 nm).** The initial volume fraction in their experiment was ca. $\textbf{10}^{-6}$. The aggregation was initiated by addition of **pyridine**. When the aggregates were roughly about 500 nm, the shear (ca. $\boldsymbol{\gamma \approx 10^4\ \text{sec}^{-1}}$) was applied by forcing the

sample through a tube using a syringe pump. The clusters were exposed to shear for times shorter than **0.5 sec**, ensuring that no significant aggregation occurs during this shearing. Immediately after the shearing, the aggregation was stopped by addition of surfactant. The sample was then examined by static light scattering measurements. There were **two slopes** in the light scattering structure. The slope at smaller length scale (large q) was similar to the unsheared sample (i.e., $\mathbf{D_f = 1.84}$ in DLCA regime). The second slope, having a stronger slope, was at larger length scale (small q). By increasing the shear rate, the negative slope (at low q) increased from **2.2** to **2.8**. They suggested that the shear caused the fractal aggregates to restructure the aggregates. These **restructuring** occurred at larger length scales, where the structure is weaker and the forces larger. However, below some length scale, the aggregates were strong enough to withstand the shear to which they were subjected. The formation of loops and additional bonds ensured that some of the mass of the clusters was moved toward their centers, hence resulting in a decrease in R_g. They also considered the possibility of fragmentation, but their DLS results did not show any measurable change in R_h after the shear was applied, and hence they concluded that fragmentation did not happen in their experiments. Moreover, the length scale R_q corresponding to the cross over between the two slopes on q scale decreased very rapidly with increasing shear. By further increasing the shear rate, R_q approached a asymptotic constant value of 100 nm.

Selomulya et al. (Selomulya et al 2002) used a SALS technique ($q = 100 - 10^5\ cm^{-1}$) to monitor the aggregate size and structure in the shear-induced aggregation of dilute suspensions of latex particles with different diameters (i.e., 60, 380, and 810 nm) in a Couette flow cell under shear rates ranging from **30 to 300** $\mathbf{sec^{-1}}$. In their experiments, both laminar and turbulent (i.e., $\gamma > 100\ \mathrm{sec}^{-1}$) shear rates were studied. The volume fractions of **60, 380, and 810 nm** polystyrene dispersions were, respectively, $\boldsymbol{f_v = 3.83 \times 10^{-6}}$, $\boldsymbol{f_v = 3.74 \times 10^{-5}}$, and $\boldsymbol{f_v = 3.76 \times 10^{-4}}$ after being mixed with equal volume of $\mathbf{MgCl_2}$ salt solutions (i.e., with final concentration of **0.05 M**). A small sample was continuously transferred into the scattering cell using a tube; the sample was then pumped back into the shear cell. This group found that the aggregates formed of 60 nm and 380 nm particles rapidly attained their maximum size before

reaching significantly smaller steady state values, particularly at low shear rates. Whereas the aggregates of 810 nm particles displayed negligible or no decrease in aggregation size on approaching equilibrium. They also showed that the differences in the aggregates behavior were less apparent at higher shear rates, where fragmentation was favored, regardless of the primary particle size. There were two slopes in their light scattering data (i.e., similar to the results of Lin et al. presented above) of which here we focus on the small q region (or larger length scale) referred by this group as SE[21] (i.e., scattering exponent). For **60 nm**, the SE was $\mathbf{D_f \approx 2.65}$ for $\gamma = 32 \text{ sec}^{-1}$ increasing to $\mathbf{D_f \approx 2.8}$ for $\gamma = 330 \text{ sec}^{-1}$. For $\gamma < 100 \text{ sec}^{-1}$, it was suggested that restructuring was the main mechanism to form compact aggregates based on the measurements of the aggregate size R_g and the number of particles per cluster N (both obtained from SALS measurements). If fragmentation was the sole cause of the reduction of the aggregate size, it was expected that R_g and N decreased simultaneously. However, their results showed that R_g and N initially increased due to shear-induced aggregation, R_g then reached a maximum before N. They suggested that aggregates first **restructured** but then **fragmentation** eventually occurred as R_g and N decreased concurrently. For $\gamma > 100 \text{ sec}^{-1}$, both R_g and N initially increased due to shear-induced aggregation, but remained more or less constant during shearing. The aggregates formed of **380 nm** particles **restructured** due to shear which then followed by **fragmentation**, and at higher shear rates fragmentation was the dominating mechanism (i.e., similar to aggregates formed of 60 nm particles). The fractal dimension of the aggregates was $\mathbf{D_f \approx 2.50}$ for $\gamma = 32 \text{ sec}^{-1}$ and $\mathbf{D_f \approx 3}$ for $\gamma = 246 \text{ sec}^{-1}$. For aggregates formed of **810 nm** particles, no decrease in size was observed after the aggregates reached their equilibrium size, whereas *SE* still continued to increase. Therefore, they concluded that **fragmentation** and **reaggregation** were the main mechanisms in governing the final aggregate size and structure.

[21] A complication, which arises with the light scattering measurement of aggregates undergoing restructuring, is a change in the slope of scattered light intensity versus the scattering vector q plots, which violates the RDG approximation. The slope of these plots were designated the scattering exponent (SE), rather than the fractal dimension in view of these uncertainties (Peker 2007)

The fractal dimension of the aggregates was $\mathbf{D_f \approx 2}$ for $\gamma = 32\ \text{sec}^{-1}$ and $\mathbf{D_f \approx 2.7}$ for $\gamma = 246\ \text{sec}^{-1}$.

Figure 7.1 shows a schematic illustration of the possible effects of shear on the structure of a fractal aggregate.

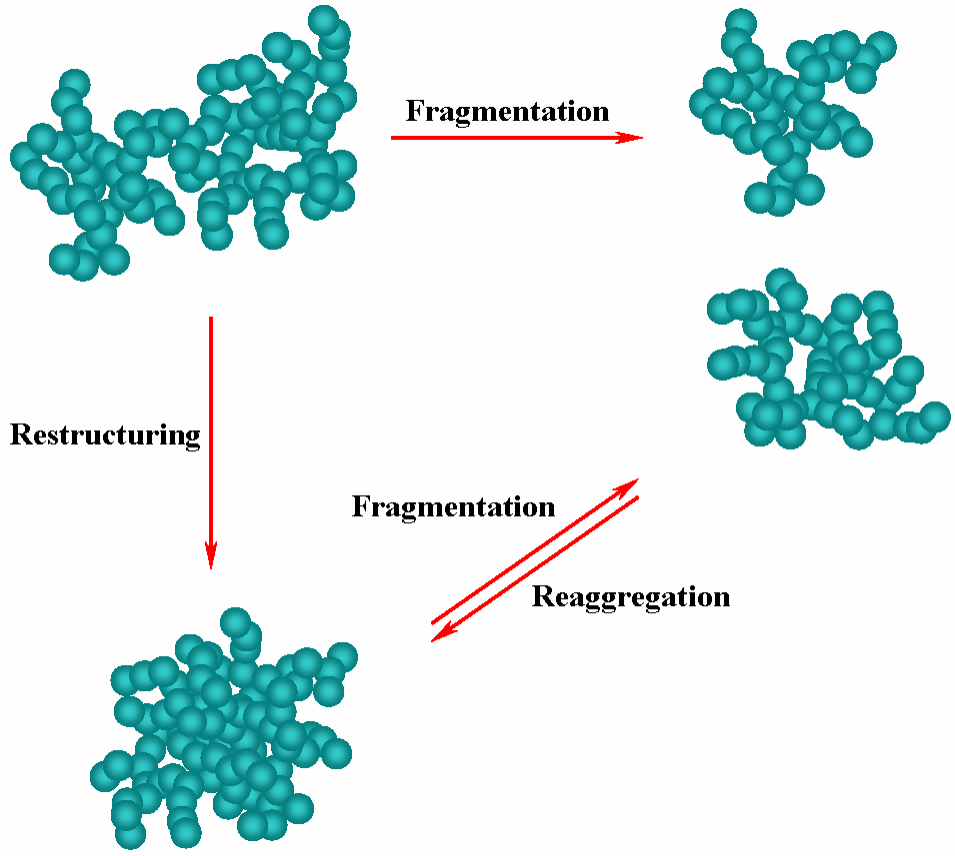

Figure 7.1 A schematic of shear effects on the structure of a fractal aggregate.

Based on the literature presented above, it can be concluded that aggregates made of smaller particles are more prone to restructuring instead of fragmentation when compared with those composed of larger particles particularly at low to moderate shear rates. It is shown that the aggregates of smaller primary particle size are generally stronger than the aggregates of the larger particles in similar physical and chemical conditions (Selomulya et al 2002). Although larger primary particle size may lead to greater bonding force between the particles, the aggregate strength also depends on the number of contacts per unit cross sectional area.

Consequently, the average size of flocs constituted of larger primary particles that can survive in a given shear field is usually lower than their counterparts composed of smaller particle size, and hence more prone to fragmentation.

Figure 7.2 summarizes the highlights of the literature-reviewed shear effects on the structure of the fractal aggregates. We have also included our work for comparison. Shear stress may result in restructuring (denoted with R), fragmentation (denoted with F), or a combination of both (denoted with R&F). In the legend of Fig. 7.2, the papers corresponding with these data are listed.

As can be seen in the legend of Fig. 7.2, some of the authors' names are shown in a gray area. This is to distinguish the experiments which showed an increase in the fractal dimension (i.e., more compact aggregates) for higher shear rates from those in which the fractal dimension was independent of the shear rates. Moreover, it should be pointed that in all the papers listed in the legend of Fig. 7.2, relatively compact aggregates were obtained, except for the work of Torres et al. where the fractal dimension of the sheared and unsheared aggregates were similar ($D_f = 1.8$).

In the presented literature review, the effect of shear has been mostly studied in a continuous presence of shear where shear-induced aggregation was dominant over Brownian aggregation (i.e., $Pe > 1$) during the entire experiment. Further, mostly large particle sizes (i.e., 0.5-2 μm) were used by these groups. When small particle sizes are used, the shear has been relatively high so that fragmentation was favored in their systems (Selomulya et al 2002, Torres et al 1991a), or the shear was applied for less than a second to investigate the immediate effect of shear (Lin et al 1990a).

To our knowledge, the effect of shear for small particle sizes and low shear rates has not been studied in the literature (see Fig. 7.2); therefore, a series of experiments were carried out in this group to investigate the shear effect at these conditions. Unlike other groups, we applied a low shear rate for only a short period; then, the morphology of the aggregates and the aggregation kinetics were studied up to the completion of gelation. Moreover, in this work shear

was initiated both in a cluster dilute regime (similar to other works) and in a cluster dense regime. A cluster dilute regime is defined as when the mean nearest neighbor separation R_{nn} is much larger than the aggregates characteristic size R_g ; a cluster dense regime is defined as when R_{nn} is comparable with R_g in an aggregating system (Huang et al 1998).

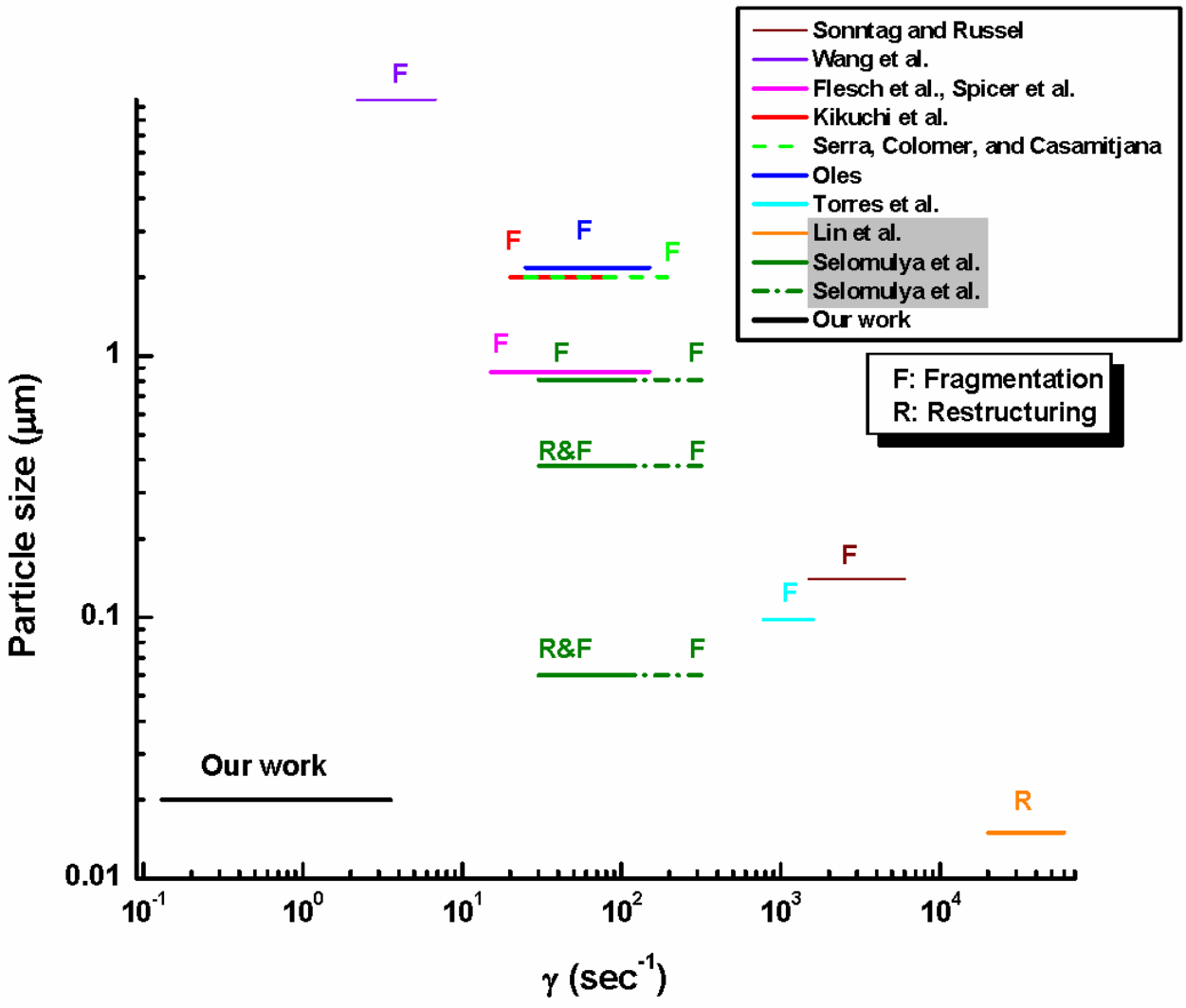

Figure 7.2 Literature review of the effects of shear on structure of aggregates. Aggregates may undergo fragmentation (F), restructuring (R), or a combination of restructuring and fragmentation (R&F). The gray area in the legend distinguishes the work of those in which fractal dimension increased with a higher shear rate (gray area) from those where fractal dimension was independent of the shear rate.

7.3 Experimental Methods

In the work presented here, we investigated the effect of shear on an aggregating colloidal system with small primary particles, 20 nm. The shear was applied for only a short period during the aggregation. The sample was sheared only once at different times after the onset of aggregation. Thus, the effect of shear (e.g., fractal dimension, gel time) was studied for both $Pe < 1$ (i.e., Brownian aggregation is dominant) and $Pe > 1$. *In situ* light scattering technique was carried out to study the effect of shear.

The final salt concentration was **10 mM**, and the final volume fraction of the polystyrene particles was $\boldsymbol{f_v = 4.36 \times 10^{-4}}$. Equal volumes of polystyrene and salt solutions were simultaneously squirted, with 50 μl syringes, into the scattering cell. The optical path length of the cell was 1.8 mm. The mixed solution did not completely fill the cell, and a bubble (i.e., approximately 0.14 of the total volume of the cell) was present in the cell.

In the experiments presented here, the rotational speed of the sample holder was varied between **0.085 rad/sec** to **2.83 rad/sec**, corresponding to the simulated average shear rates of **0.13 to 3.56 sec^{-1}** (i.e., described below). The axis of rotation of the sample holder, hence the angular velocity vector $\vec{\omega}$ was parallel to the direction of the incident laser beam, perpendicular to the windows. The rotation rate of the sample holder was varied by altering the voltage of a DC gear motor (Grainger).

The samples were sheared for a short period (i.e., referred to as **shear duration time)** and *only once* at different times after the onset of aggregation (i.e., referred to as **shear initiation time)**. The shear initiation time was typically **1, 2, 3, 5, and 15 min**. The shear duration time was **33 ± 3 sec**. The schematic side view of the sample holder is shown in Fig. 7.3.

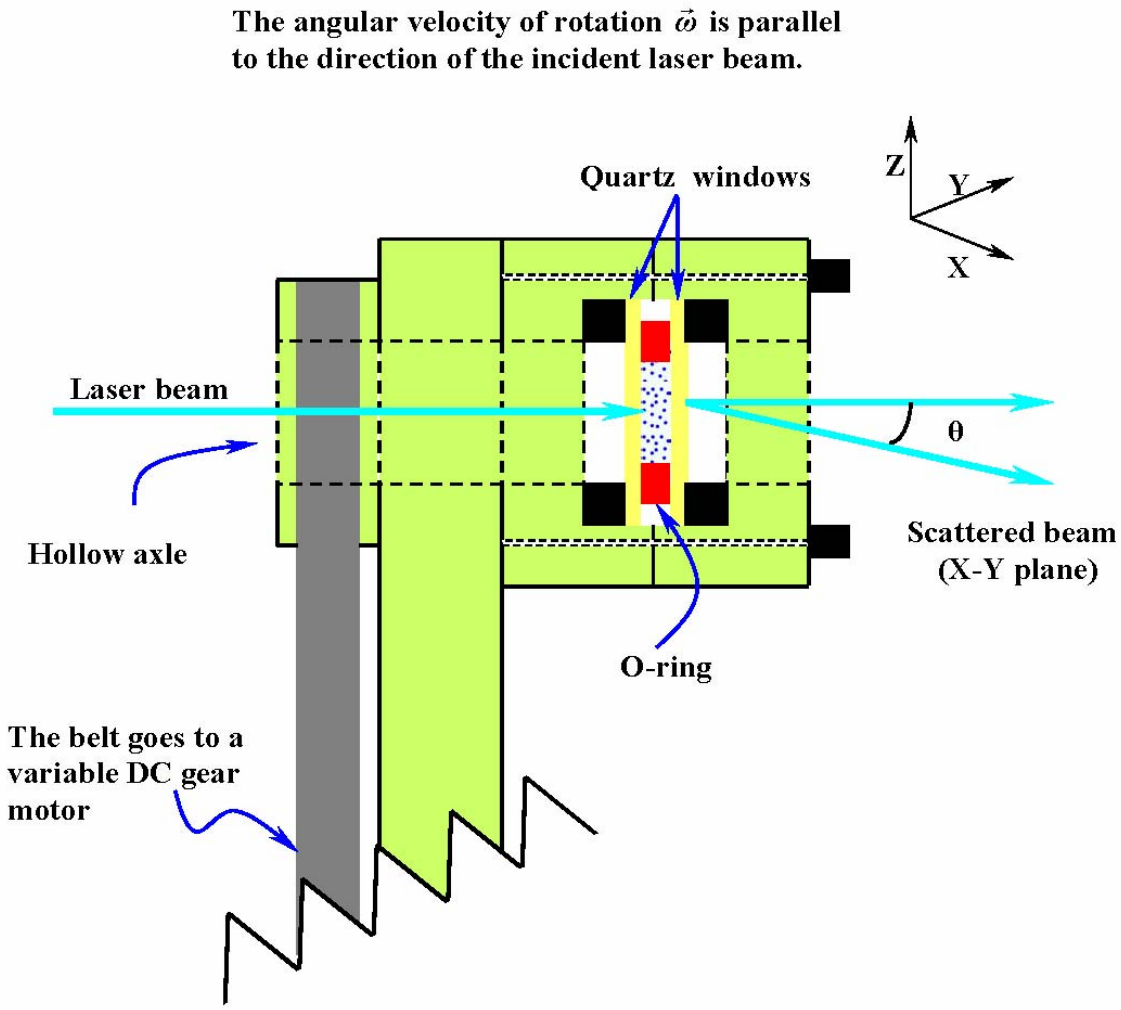

Figure 7.3 A schematic side view of the scattering cell and the sample rotator.

The velocity profile of a sheared sample is shown as an example in Fig. 7.4. Particle Image Velocimetry (PIV) technique was used to observe the effect of the air bubble (mentioned above) on the shear flow. We used 9.6 μm polystyrene colloidal dispersion in order to perform these measurements.

As can be seen in Fig. 7.4, the local shear rate is zero in the center and has the maximum value (for a given shear rate) near the edge of the cell. The shear rate was linear throughout the entire cell, excluding the air bubble in the cell. Also, due to the presence of a bubble on the top of the cell (i.e., mentioned earlier), the shear is rather nonuniform on the upper half of the cell. Therefore, the vertical position of the scattering cell was adjusted so that the laser beam mostly

hit the lower half of the cell, approximately at a fixed position during the shear experiments. However, we should remind again that no measurements were obtained during shearing.

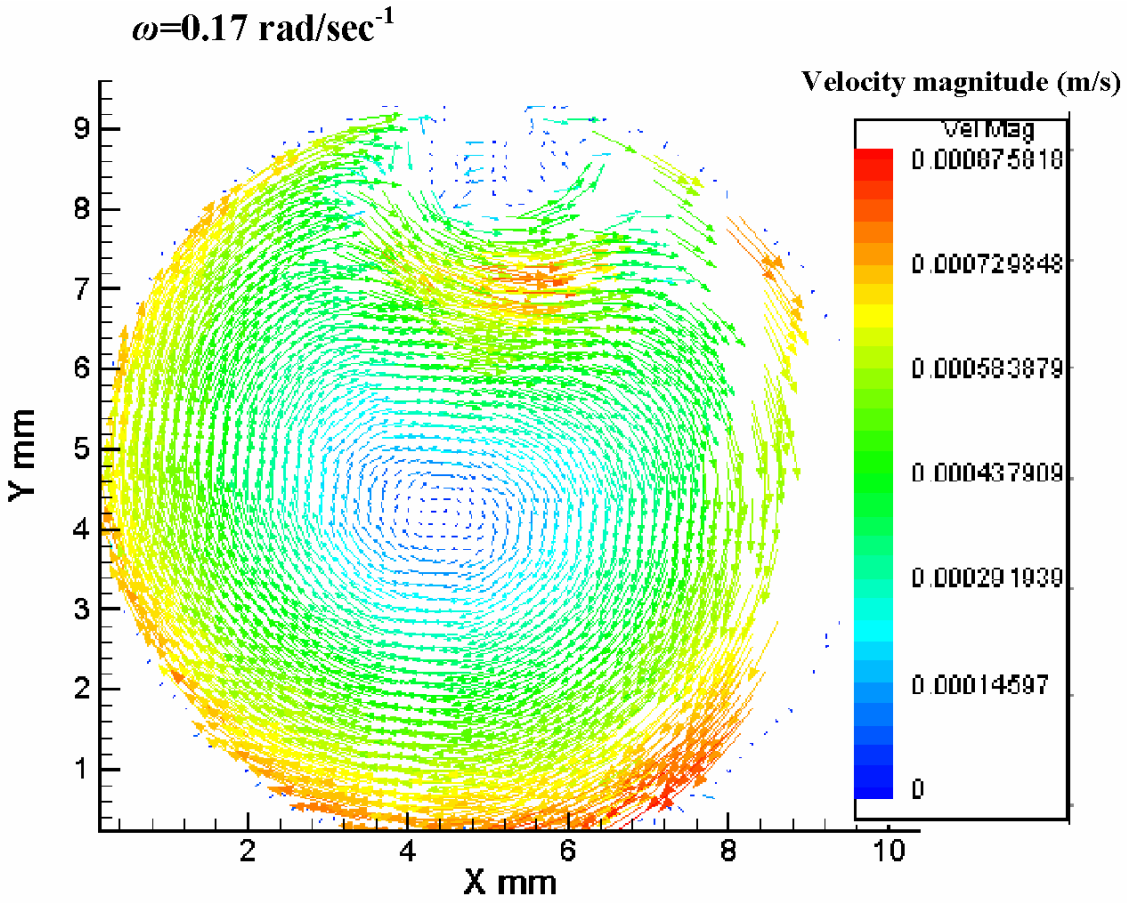

Figure 7.4 Particle velocity profile of a sheared cell. A colloidal dispersion of 9.6 μm polystyrene particles was used for the PIV measurements. The angular velocity of the cell was 0.17 rad/sec.

In order to estimate the laminar shear rate for our cell, we assumed that the velocity of the suspension near the glass plates was equal to the velocity of the glass plates themselves when the sample was rotated (i.e., there was no slip). We also assumed that the velocity of the suspension halfway between the two windows was zero, because gravity held the liquid at the bottom of the cell. Thus, the approximate shear rate $g(r)$ was determined, i.e.,

$$g(r) = \frac{r\omega}{d/2}, \tag{7.2}$$

where r is the radial distance from the rotation axis, d is the thickness of the cell (d = 2mm). The approximate average shear rate $\boldsymbol{\gamma}$ was then determined by the following integration over the entire cell, i.e.,

$$\gamma = \frac{\int_0^{R_{cell}} g(r)\, 2\pi r\, dr}{\int_0^{R_{cell}} 2\pi r\, dr}, \tag{7.3}$$

where R_{cell} is the radius of the cell that is the radius of the O-ring, R_{cell} = 4.5mm (see Fig. 7.3). Eq. (7.2) was substituted into Eq. (7.3), and after the integration the approximate average shear rate was determined as

$$\gamma = \frac{4 R_{cell}\, \omega}{3d}. \tag{7.4}$$

In this work, the rotational speeds were 0.085, 0.17, 0.35, 0.75, 1.26, 2.09, and 2.83 rad/sec. Equation (7.4) was then used to **calculate** the average shear rates 0.26, 0.51, 1.1, 2.2, 3.8, 6.3, and 8.5 $\sec^{-1}$.

The average shear rate was also simulated[22] with the computational fluid dynamics (CFD) software FLUENT 6.2.12 (Tannehill et al 1997). This program uses the finite volume method to numerically solve the equations of motion and continuity on a computational mesh of user-specified geometry. It also allows the user considerable flexibility to select appropriate options (e.g., rheological models, turbulence closure schemes, boundary conditions, numerical integration schemes, etc.). CFD simulations of Newtonian fluids in relatively simple geometries

[22] Chung-yin Cheng and Dr. Dennis Vigil at Iowa State University performed these simulation work.

at low Reynolds numbers have been well validated by experimental measurements. Hence the use of CFD simulations to calculate the shear rates in our shear cell is justified.

In the present case, a computational mesh consisting of 10,770 nodes was constructed to represent the interior and the inside walls of the fluid flow cell. The unsteady equations of motion for laminar Newtonian flow with no slip boundary conditions at the cell walls were integrated using FLUENT's built in variable time step option to minimize error. The presence of the air bubble required the use of a two-phase model. The FLUENT implementation of the volume of fluid scheme (Hirt & Nichols 1981) was selected for this purpose because of its ability to accurately simulate, with relatively low computational cost, the transport of fluid-fluid interfaces. The integrations were carried out with stagnant fluid initial conditions and were terminated after the calculated velocity fields reached steady state. The computed steady-state velocity fields exhibited simple and intuitive results. In particular, the liquid phase was nearly stagnant in a region approximately intermediate between the bubble-liquid interface and the bottom of the cell, in the plane that bisects the two disks. The magnitude of the fluid velocity increased monotonically as the flow cell walls were approached from this stagnation zone (except of course where the rotational axis intersects the walls).

The volume-averaged shear rate in the liquid phase was computed from the calculated velocity fields excluding a small region near the bubble-liquid interface where the computed shear rate was evidently high because of the large difference between the velocities in the liquid and gas phases. The computed average shear rates were **0.13, 0.24, 0.48, 0.99, 1.60, 2.61, and 3.56 $\mathbf{sec^{-1}}$** for rotational speeds of 0.085, 0.17, 0.35, 0.75, 1.26, 2.09, and 2.83 rad/sec.

Our simple model of estimating the average shear rate and the simulation work were approximately different by a factor of 2.3, where the calculated shear rates were higher than the computed values. In this work, we have reported our results based on the computed shear rates. However, we should mention here that the average shear rates reported here should be taken as estimates rather than absolute values.

In order to approximately estimate the Péclet number in our experiments, the characteristic size of the aggregates R_g immediately **before applying shear** was substituted instead of the particle radius a in Eq. (4.33), i.e.,

$$Pe = \frac{3\pi\eta R_g^3 \gamma}{k_B T}. \tag{7.5}$$

The reason for the substitution of R_g was that in our experiments shear was initiated at different times after the onset of aggregation. Therefore, the use of the particle size was not an appropriate choice to determine the Péclet number.

7.4 Results and Discussions

In order to study how shear affects the aggregation kinetics and the structure of the aggregates, we carried out light scattering measurements of an aggregating system with no shear (i.e., Brownian aggregation), an example of which is shown in Fig. 7.5. It is important to note that the intensity of the laser beam varied from sample to sample and throughout this project. Therefore, the scattered intensities of the figures shown hereafter cannot be compared with one another.

Figure 7.5 shows the scattered intensity $I(q)$ (arbitrary units) measurements versus the scattering wave vector, $q\,(cm^{-1})$ at various times (i.e., 6- 57 min) after the onset of aggregation. The final volume fraction of the polystyrene solution was 4.36×10^{-4}, and the final salt concentration was 10 mM.

As can be seen in Fig. 7.5, the scattered intensity at small q increases with time; this can be explained as follows. $I(q) \propto n_m N \propto N$, where n_m is the initial monomer number density (i.e., constant), and N is the number of monomers per cluster. As an aggregating colloidal system aggregates, N increases with time resulting in an enhancement of the scattered intensity.

The Guinier regime, (i.e., where the slope of I versus q goes from 0 to negative) progresses to smaller q as aggregates become larger. One can qualitatively determine the size of the aggregates by using $R_g \sim q^{-1}$. The fractal dimension of the aggregating system (i.e., the power law regime) is $\mathbf{D_f = 1.78 \pm 0.03}$, consistent with the DLCA process.

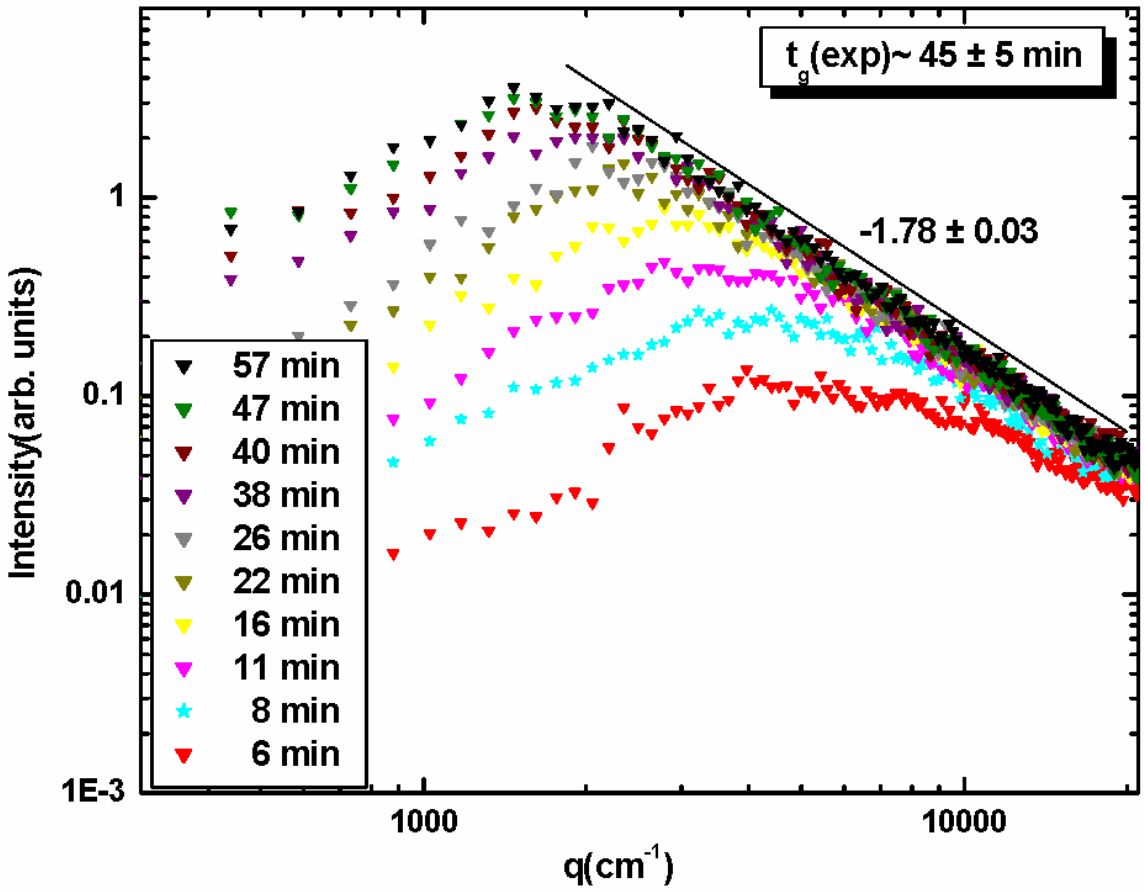

Figure 7.5 Static light scattering $I(q)$ versus the scattering wave vector $q(\mathrm{cm}^{-1})$ at different times after the onset of aggregation. The fractal dimension is ca. $D_f = 1.78 \pm 0.03$ (i.e., in DLCA regime). The experimental gel time is ca. $t_g = 45 \pm 5$ min.

The peak in $I(q)$ versus q appears in the structure factor ($S(q) \propto I(q)$) of the dense aggregating colloidal systems when the characteristic size of aggregates R_g becomes comparable in magnitude to the mean nearest neighbor separation of the aggregates, R_{nn} (Cerda

et al 2004, Huang et al 1998). The static light scattering stopped evolving after about 45 ± 5 min. Based on the definition of a gel in our work, a sample is gelled when light scattering intensities stops evolving, and there is no further aggregation. With this definition, the gel time of the sample was $\boldsymbol{t_g = 45 \pm 5\,min}$.

Light scattering measurements was then carried out for shear initiation time of **1 min** at various shear rates (i.e., $\gamma = 0.13 - 3.56\ \text{sec}^{-1}$). The volume fraction (i.e., 4.36×10^{-4}) and the salt concentration (10 mM) remained similar to the Brownian aggregation experiment (i.e., unsheared). An example of the shear experiments with the above conditions are shown in Fig. 7.6.

Figure 7.6 shows the scattered intensities $I(q)$ (arbitrary units) versus $q(cm^{-1})$ at different times before initiating the shear and after cessation of the shear. The average shear rate was $\boldsymbol{\gamma = 0.99\,sec^{-1}}$. The shear initiation time was **1 min**, and the sample was sheared for ca. **33 sec**. In order to understand the light scattering data, the legend of the figure is separated into two different boxes, i.e., the data before shear was applied and the data after shear was stopped. In addition, the time in both legends has started from zero. However, these two different times are added for the reported experimental gel time. The time gap between these two measurements is the time that sample was sheared (i.e., marked with the yellow box).

As can be seen in Fig. 7.6, the light scattering intensity increases with time indicating the system is aggregating. The fractal dimension is $\mathbf{D_f = 1.80 \pm 0.04}$ and the sheared sample gelled within $\boldsymbol{t_g = 50 \pm 10\,min}$. If the fractal dimension (indicating the compactness of an aggregating system) in this figure is compared with Fig. 7.5, it can be seen that the fractal dimensions are similar within the uncertainty of the experiments. Therefore, shear did not form more compact aggregates. Furthermore, the gel time, which is related to the kinetics of aggregation, remained the same as the unsheared sample (Fig. 7.5). On the other hand, the scattered intensities did not enhance due to shear as expected for the shear-induced aggregation (for example, compare the data for 0.5 min after shear was stopped and before applying the shear). These comparisons between Figs. 7.5 and 7.6 indicate that shear did not affect the kinetics of aggregation and the

structure of aggregates. However, later in this work, we will present the analyses of the evolution of the aggregate size (R_g) with time as to compare the kinetics of aggregation for various shear initiation times and at different shear rates in this work.

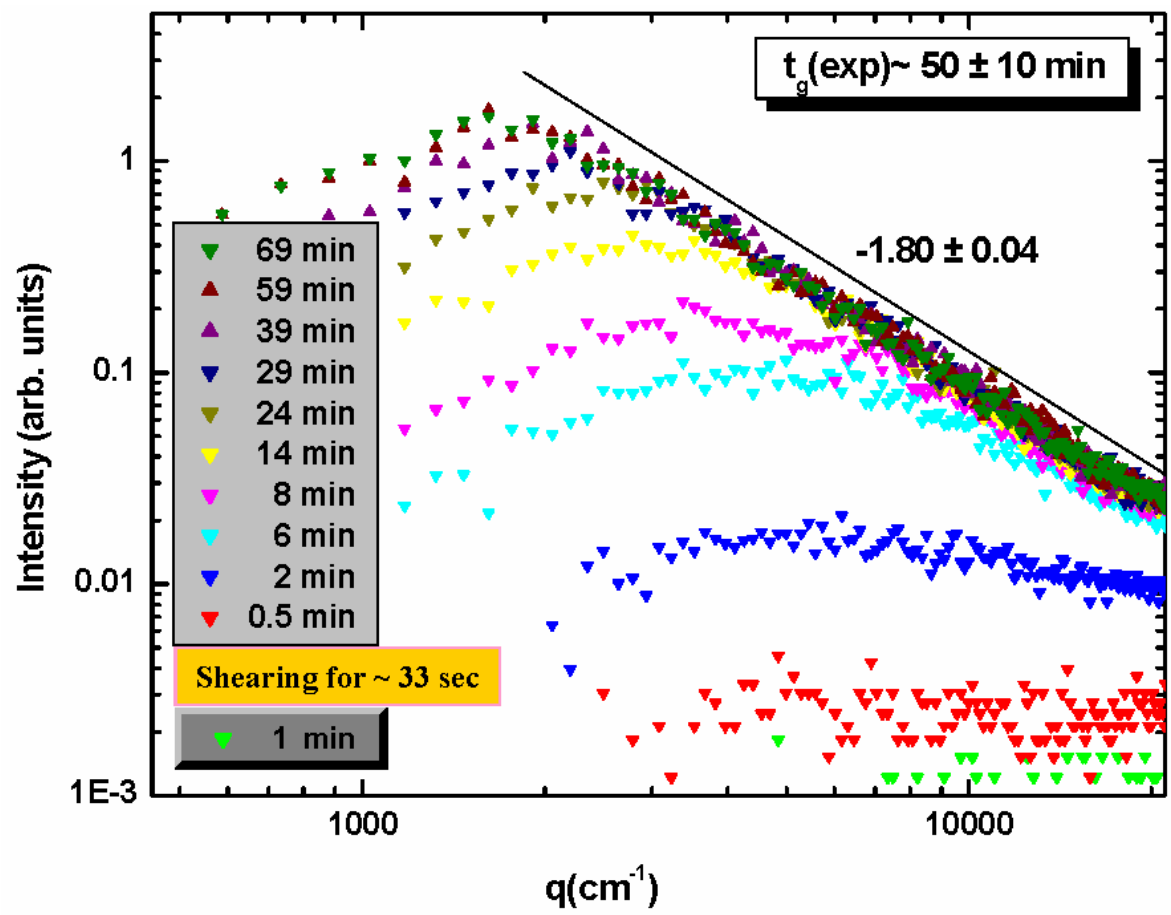

Figure 7.6 Static light scattered intensities $I(q)$ (arbitrary units) versus q (cm^{-1}) at different times before applying the shear and after termination of the shear, γ = 0.99 sec^{-1}. The shear initiation time was 1 min. Gelation occurred at about t_g = 50 ± 10 min. The fractal dimension is D_f = 1.80 ± 0.04.

Table 7.1 summarizes the results (i.e., t_g and D_f) of the shear experiments at various shear rates when the shear initiation time was 1 min.

As can be seen in Table 7.1, at all shear rates the gel time is more or less the same as that of the unsheared sample (i.e., $t_g = 45 \pm 5$ min). The fractal dimension also remained 1.80 for various shear rates which is similar to that of the unsheared sample (i.e., $D_f = 1.78 \pm 0.03$). The Péclet number (i.e., calculated using Eq. (7.5)) was less than one at all shear rates.

Table 7.1 Results of the gel time and fractal dimension for shear initiation time of 1 min at various shear rates ranging from 0.13 to 3.56 sec^{-1}. The error in the fractal dimension is approximately 0.04.

Shear initiation time: 1 min							
γ (sec^{-1})	**0.13**	**0.24**	**0.48**	**0.99**	**1.60**	**2.61**	**3.56**
D_f	**1.80**	**1.80**	**1.80**	**1.80**	**1.78**	**1.80**	**1.80**
t_g (min)	**40 ± 5**	**40 ± 5**	**35 ± 5**	**50 ± 10**	**45 ± 10**	**40 ± 10**	**45 ± 10**

Figure 7.7 shows the scattered intensities $I(q)$ (arbitrary units) versus $q(cm^{-1})$ at different times before applying the shear and after shear was stopped. The average shear rate was $\gamma = \mathbf{2.61\,sec^{-1}}$. The shear initiation time was ca. **2 min**, and the sample was sheared for ca. **33 sec**. Similar to Fig 7.6, the data before applying the shear and after cessation of the shear are shown in separate legends.

Figure 7.7 shows that the light scattering data before applying shear indicates that the size of the aggregates are small compared to the wavelength of the light, and hence the scattering is in Rayleigh regime. The sample was then sheared for 33 sec. The first data was collected after shear was stopped (i.e., shown with red triangle symbol).

As can be seen in this figure, the scattered intensity has significantly increased (i.e., shown with the arrow) after shear was stopped. This enhancement in the scattered intensity suggests that shear has enhanced the aggregation.

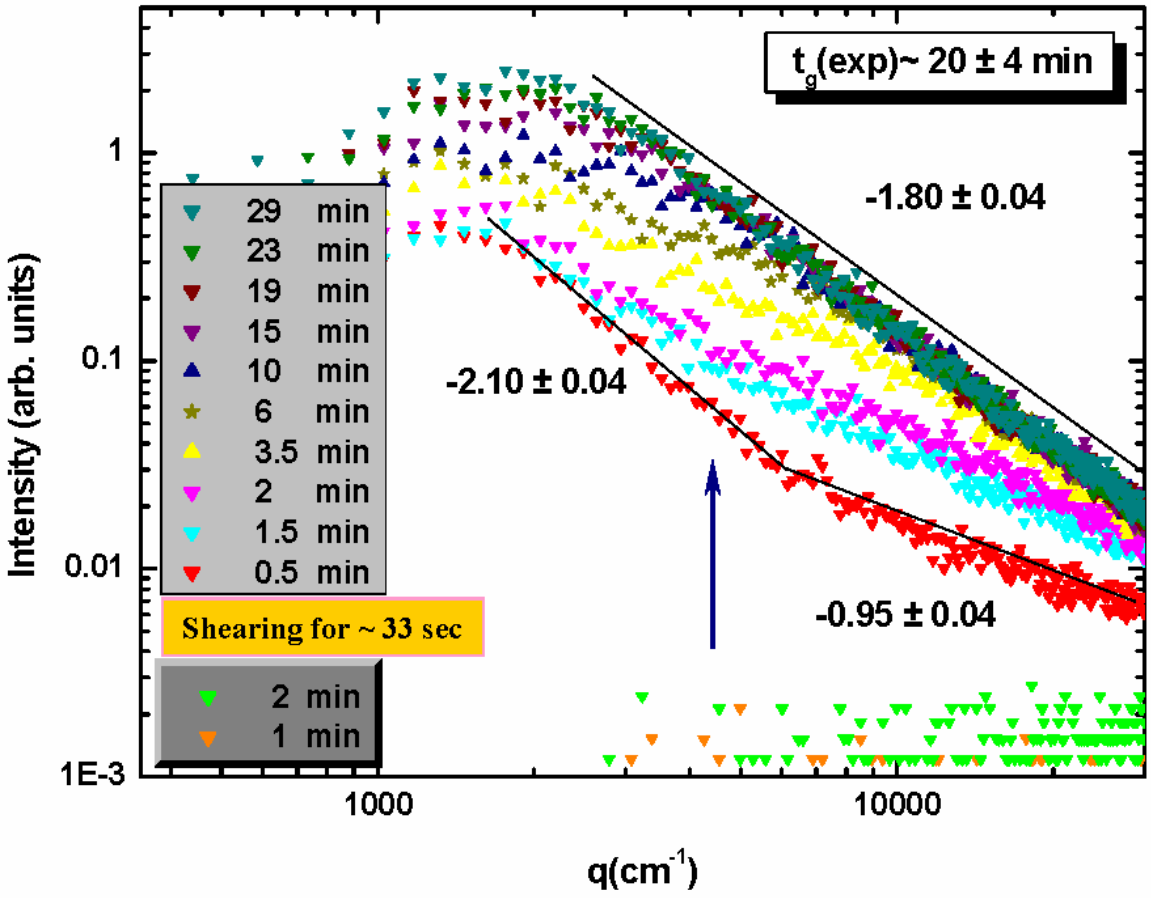

Figure 7.7 Static light scattered intensities $I(q)$ (arbitrary units) versus q (cm^{-1}) at different times before applying the shear and after termination of the shear, $\gamma = 2.61\ sec^{-1}$. The shear initiation time was ~2 min. Gelation occurred at about $t_g = 20 \pm 4$ min. There is a crossover between two slopes of -0.95 ± 0.04 and -2.10 ± 0.04 evolving to -1.80 ± 0.04 at the gel point.

Figure 7.7 shows that shear has caused a hybrid aggregate structure in the aggregating system (two slopes over the entire range of q imply a hybrid structure), and a crossover between two negative slopes of $\mathbf{0.95 \pm 0.04}$ and $\mathbf{2.10 \pm 0.04}$ can be seen in this figure. These two slopes indicate two different aggregate structures at different length scales. We speculate that the

negative slope of 0.95 at higher q does not have any quantitative significance. As we were limited in our ability to detect the scattering intensity at larger scattering angles, and hence the power law regime, which *could have* a negative slope of 1.8, was not detected. After shear was stopped, Brownian aggregation eventually overcame the shear-induced hybrid structure and **repaired** the clusters over time, until the sample gelled with a more tenuous structure that is $\mathbf{D_f = 1.80 \pm 0.04}$. The Guinier analysis showed that the aggregates slightly decreased in size after cessation of the shear all throughout the completion of gelation. We call this *post-shear aggregate restructuring*. A rough calculation shows that if these fairly compact $D_f = 2.1$ aggregates changed to a more tenuous $D_f = 1.8$ aggregates, the aggregate radius of gyration should have become approximately 3 times larger. However, our results do not show any increase in the aggregates' size. Thus, the disappearance of the double structure is perplexing and remains yet a question. The sample gelled at about $\mathbf{t_g = 20 \pm 4\ min}$ which was shorter than the gel time of the unsheared sample, another evidence for the shear enhanced aggregation.

For shear initiation time of 5 min, three different behaviors were observed depending on the applied shear rates. The Péclet number was greater than one at all shear rates. These results are shown in Table 7.2 and will be explained accordingly. An example of light scattering measurements will be given for each category.

Table 7.2 Gel time and fractal dimension for the shear initiation time of 5 min at various shear rates ranging from $\gamma = 0.13\text{-}3.56\ \text{sec}^{-1}$. The error in the fractal dimension is approximately 0.03.

Shear initiation time: 5 min							
γ (sec^{-1})	0.13	0.24	0.48	0.99	1.60	2.61	3.56
D_f	1.71	1.73	1.75	1.81	1.4 & 2.1 evolved to 1.84	1.4 & 2.1 evolved to 1.83	1.7&2.45
t_g (min)	30 ± 5	25 ± 5	20 ± 5	25 ± 5	15 ± 5	13 ± 3	6 ± 1

(5min-i) At low shear rates ($\boldsymbol{\gamma = 0.13 - 0.99\ sec^{-1}}$), applying the shear enhanced the aggregation. After termination of the shear, Brownian motion continued the aggregation until the sample gelled with a fractal dimension of $\mathbf{D_f = 1.75 \pm 0.05}$. The average gel time of the sheared sample in this range was approximately $\boldsymbol{t_g = 25 \pm 5\ min}$, shorter than the gel time of an unsheared sample. Figure 7.8 shows an example representing this category.

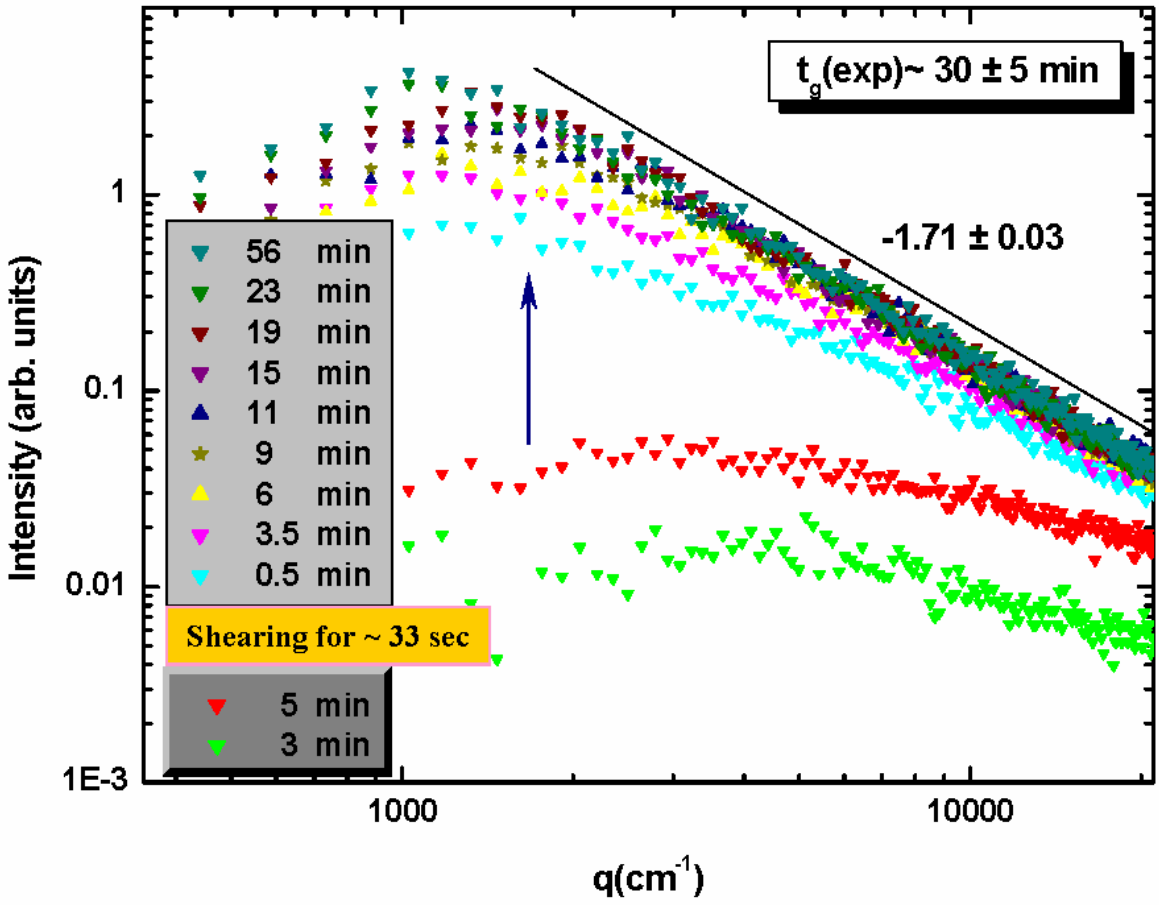

Figure 7.8 Static light scattered intensities $I(q)$ (arbitrary units) versus q (cm^{-1}) at different times before applying the shear and after termination of the shear, γ = 0.13 sec^{-1}. The shear initiation time was 5 min. The sample gelled at about t_g = 30 ± 5 min with the fractal dimension of 1.71 ± 0.03.

(5min-ii) At moderate shear rates of $\gamma = \mathbf{1.60\ sec^{-1}}$ and $\mathbf{2.61\ sec^{-1}}$, shear enhanced the aggregation and caused a hybrid aggregate structure after termination of the shear. Brownian aggregation then "repaired" the hybrid aggregate structure into a uniform gel, which was somewhat similar to Fig. 7.7 (Fig. 7.7 shows this effect more significantly than Fig. 7.9). The fractal dimension at the gel point was ca. $\mathbf{D_f = 1.83 \pm 0.03}$. The average gel time was approximately $\boldsymbol{t_g = 14 \pm 4\ min}$, shorter than the gel time of an unsheared sample. Figure 7.9 shows an example representing this category.

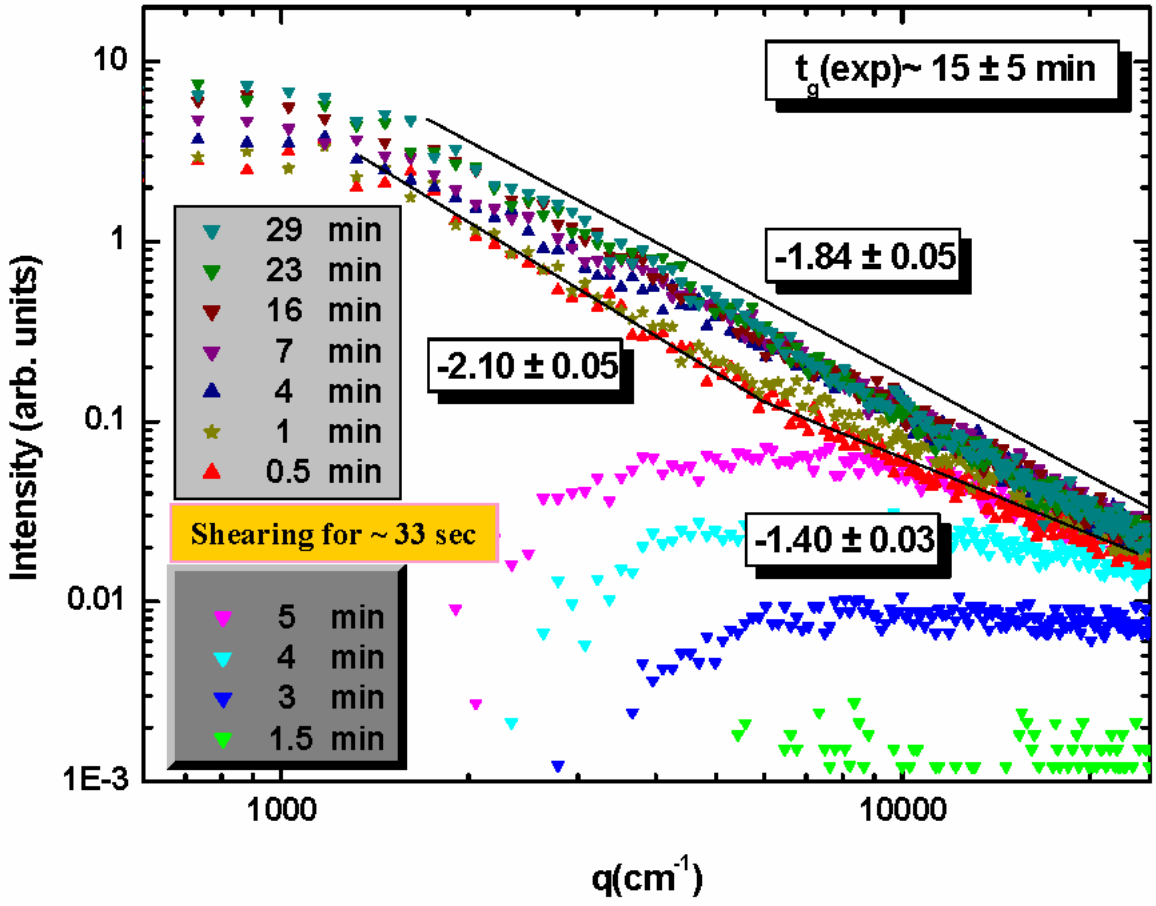

Figure 7.9 Static light scattered intensities $I(q)$ (arbitrary units) versus q ($\mathrm{cm^{-1}}$) at different times before applying the shear and after termination of the shear, γ = 1.60 $\mathrm{sec^{-1}}$. The shear initiation time was 5 min. Gelation occurred at about t_g = 15 ± 5 min. There is a crossover between two negative slopes of 1.40 ± 0.03 and 2.10 ± 0.05 evolving to 1.84 ± 0.05 at the gel point.

(5min-iii) At the highest shear rate $\boldsymbol{\gamma = 3.56\ sec^{-1}}$, not only did the shear enhance the aggregation, but it also caused the sample to reach its gel point. Furthermore, shear caused a *hybrid gel structure* (i.e., there were two slopes in the structure factor measurements). The gel time was significantly shorter than the gel time of an unsheared sample, i.e., $\boldsymbol{t_g = 6 \pm 1\ min}$. Figure 7.10 is an example representing this category.

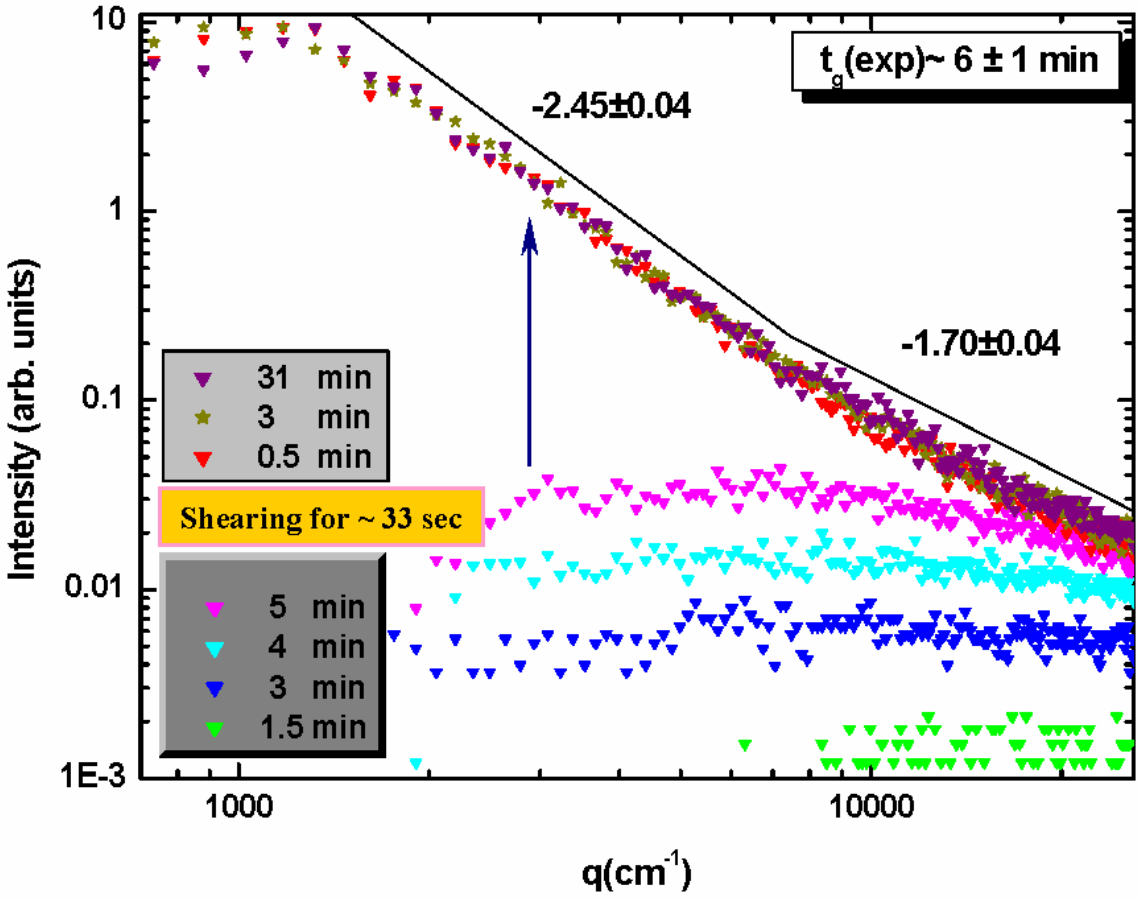

Figure 7.10 Static light scattered intensities $I(q)$ (arbitrary units) versus q (cm^{-1}) at different times before applying the shear and after termination of the shear, γ = 3.56 sec^{-1}. The shear initiation time was 5 min. Gelation occurred at about t_g = 6 ± 1 min. A crossover between two negative slopes of 1.70 ± 0.04 and 2.45 ± 0.04 can be seen at the gel point.

For the shear initiation time of 15 min, two different behaviors were observed, i.e., similar to the cases of (5min-i) and (5min-iii). The Péclet number was well above one at all shear rates. These results are shown in Table 7.3. An example of light scattering measurements will be given for each category.

As can be seen in Table 7.3, at low shear rates $\gamma < 0.48\ \text{sec}^{-1}$, shear enhanced the aggregation, and the gel time was shorter than the unsheared sample. The fractal dimension of the gel was 1.75 ± 0.04. At moderate to high shear rates $\gamma > 0.48\ \text{sec}^{-1}$, shear caused the gelation of the sample. Moreover, the gel had a hybrid aggregate structure. It is important to note that ,unlike the work of Lin et al. and Selomulya et al. (Lin et al 1990a, Selomulya et al 2002), increasing the shear rate did not increase the fractal dimension of the gel. It can be seen that the fractal dimension at larger length scales is more or less independent of the shear rates. Moreover, Sorensen, in his review article, has shown that the power law regime of an aggregate structure ($S(q) \sim q^{-D_f}$) breaks down when the fractal dimension is larger than $D_f > 2.9$ (Sorensen 2001). The highest fractal dimension reported in this work is ca. $D_f = 2.6$, and hence the fractal dimensions in our experiments are in the power law regime.

Table 7.3 Gel time and fractal dimension for the shear initiation time of 15 min at various shear rates ranging from 0.13 to 3.56 sec^{-1}. The error in the fractal dimension is approximately 0.04.

Shear initiation time: 15 min							
γ (sec^{-1})	0.13	0.24	0.48	0.99	1.60	2.61	3.56
D_f	1.75	1.75	1.75 & 2.60	1.75 & 2.55	1.65 & 2.61	1.60 & 2.52	1.73 & 2.45
t_g (min)	18 ± 2	16 ± 1	16 ± 1	16 ± 1	16 ± 1	16 ± 1	16 ± 1

(15min-i) At low shear rates ($\boldsymbol{\gamma = 0.13\ sec^{-1}}$ and $\boldsymbol{0.24\ sec^{-1}}$), the aggregating system gelled within a few minutes after termination of the shear. The average gel time was $\mathbf{t_g = 17 \pm 2\ min}$. The gel had a uniform aggregate structure with the fractal dimension of $\mathbf{D_f = 1.75 \pm 0.04}$. Figure 7.11 shows an example representing this category.

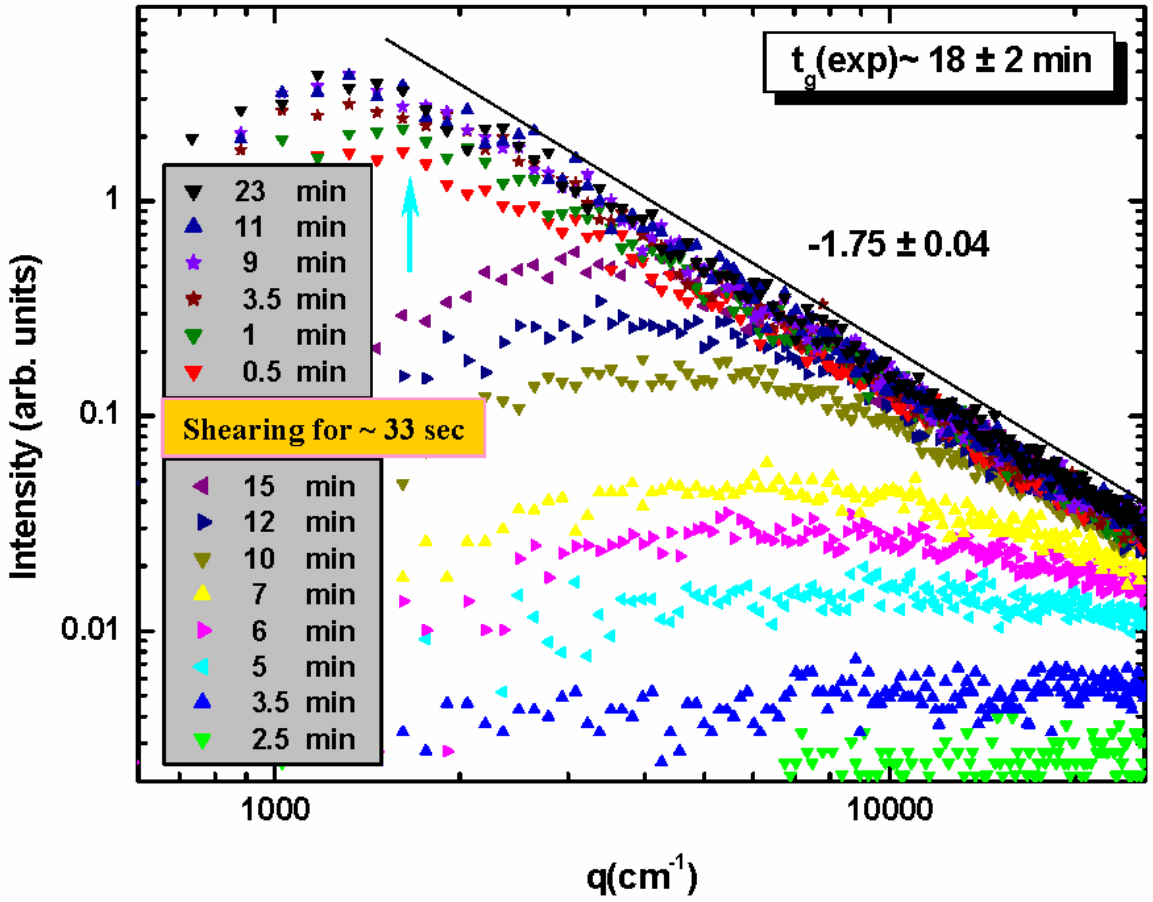

Figure 7.11 Static light scattered intensities $I(q)$ (arbitrary units) versus q (cm^{-1}) at different times before applying the shear and after termination of the shear, γ = 0.13 sec^{-1}. The shear initiation time was 15 min. The sample gelled within a few minutes after cessation of the shear at about t_g = 18 ± 2 min. The fractal dimension of the sample was 1.75 ± 0.04.

(15min-ii) At moderate to high shear rates, shear induced the gelation of the aggregating system, and the sample gelled within $\mathbf{t_g = 16 \pm 1\ min}$ (i.e., one minute past the shear initiation time). However, at these shear rates, shear caused a hybrid gel structure as can be seen in Table 7.3. Note that the hybrid aggregate structure occurred at a lower shear rate $\boldsymbol{\gamma = 0.48\ sec^{-1}}$ compared to $\boldsymbol{\gamma = 3.56\ sec^{-1}}$ in Table 7.2 suggesting that as the shear initiation time increased, a smaller shear rate was required to cause a hybrid aggregate structure. Figure 7.12 shows an example representing this category.

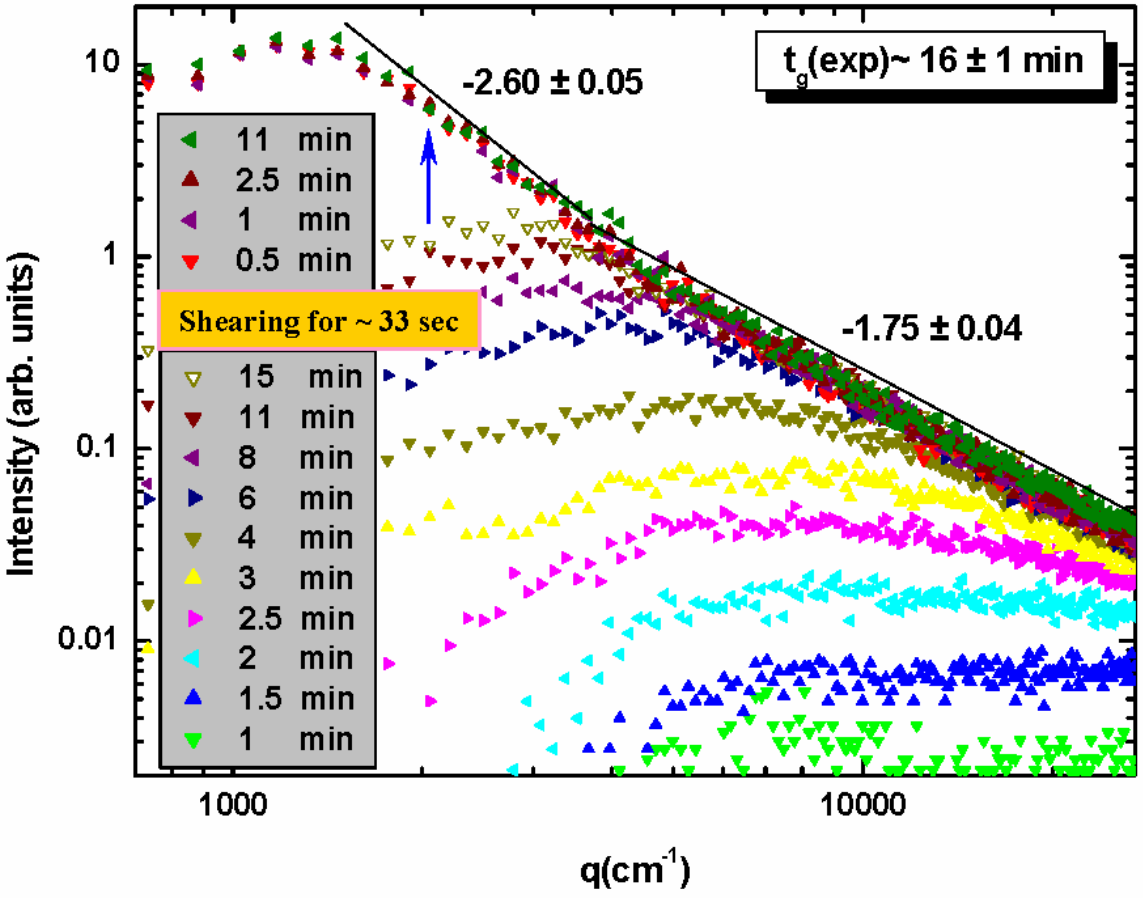

Figure 7.12 Static light scattered intensities $I(q)$ (arbitrary units) versus q (cm^{-1}) at different times before applying the shear and after termination of the shear, γ = 0.48 sec^{-1}. The shear initiation time was 15 min. Gelation occurred at about t_g = 16 ± 1 min. There is a crossover between two negative slopes of 1.75 ± 0.04 and 2.60 ± 0.05 at the gel point, indicating a hybrid aggregate structure.

Table 7.4 summarizes the highlights of the shear experiments (i.e., described above) for the shear initiation times of 1, 5, and 15 min for various shear rates ranging from $\gamma = \mathbf{0.13 - 3.56\ sec^{-1}}$.

Table 7.4 Summary of the shear effects for the shear initiation times of 1, 5, and 15 min at various shear rates ranging from 0.13 to 3.56 sec^{-1}.

Shear initiation time	Shear rate	Shear effect
No shear	N/A	Uniform gel structure (D_f~ 1.8) t_g= 45 ± 5 min.
1 min	γ= 0.13- 3.56 sec^{-1}	Uniform gel structure (D_f~ 1.8) t_g= 42 ± 8 min.
5 min	γ= 0.13- 0.99 sec^{-1}	Enhanced shear aggregation Uniform gel structure (D_f~1.8) t_g= 25 ± 5 min.
	γ= 1.60- 2.61 sec^{-1}	Enhanced shear aggregation Double structure after cessation of shear Uniform gel structure at gel point t_g= 14 ± 4 min.
	γ=3.56 sec^{-1}	Enhanced shear aggregation Double structure after cessation of shear t_g= 6 ± 1 min.
15 min	γ= 0.13- 0.24 sec^{-1}	Enhanced shear aggregation Uniform gel structure (D_f~1.8) t_g= 16 ± 1 min.
	γ= 0.48- 3.56 sec^{-1}	Enhanced shear aggregation, Double structure after cessation of shear t_g= 16 ± 1 min.

In order to gain a better understanding of the aggregation growth at different shear rates and shear initiation times, Guinier analysis was used to determine the radius of gyration at various times after the onset of aggregation. The results of these analyses are shown in Fig. 7.13.

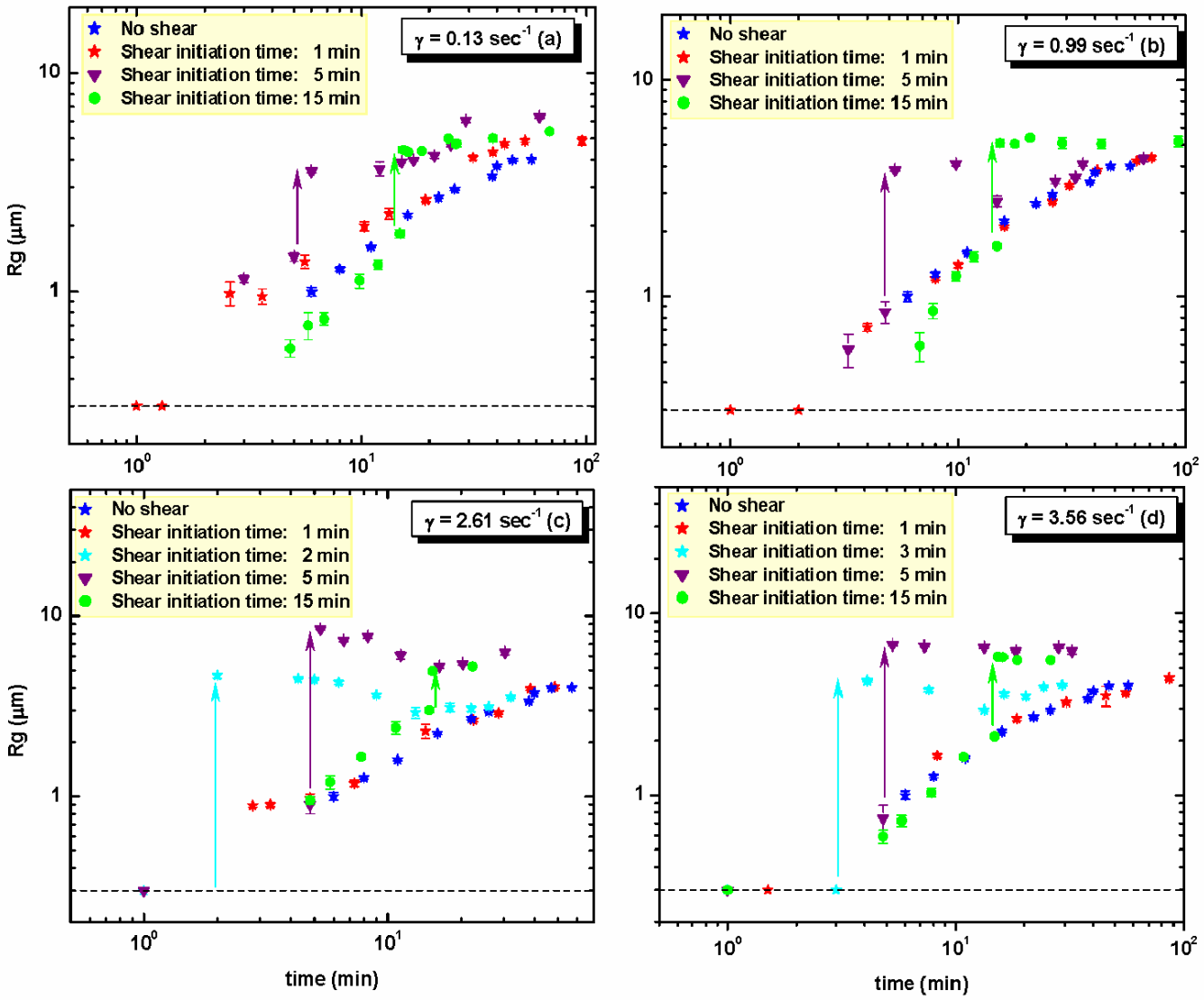

Figure 7.13 The radius of gyration R_g (μm) are plotted versus time for the no shear situation and the shear rates of (a) 0.13 sec^{-1}, (b) 0.99 sec^{-1}, (c) 2.61 sec^{-1}, and (d) 3.56 sec^{-1}. The shear initiation time was 1, 5, and 15 min for all shear rates. For shear rates of (c) 2.61 sec^{-1} and (d) 3.56 sec^{-1}, the analysis for shear initiation times of 2 min and 3 min are also shown, respectively. The horizontal dashed line is the lower limit of our SALS size measurements that is ca. 300 nm. The last data point in each curve represents the gel point

Figures 7.13(a), (b), (c), and (d) show the results of these analyses for the shear initiation times of 1, 5, and 15 min at various shear rates of $\dot{\gamma}$ = **0.13, 0.99, 2.61 and 3.56 sec^{-1}**, respectively. For shear rates of $\dot{\gamma}$**= 2.61 sec^{-1}** and **3.56 sec^{-1}**, the analyses for the shear initiation time of 2 min and 3 min are also shown. The analysis of the unsheared sample (i.e. Brownian aggregation) is also plotted in all the figures for comparison. The horizontal dashed line (shown in Fig. 7.13) represents the lower limit of our SALS size measurements that is ca. 300 nm.

The similarities and differences of the aggregate size evolution for various shear initiation times and shear rates are described as follows:

(i) For the shear initiation time of **1 min**, regardless of the shear rates, the data more or less follow the same curve as that of the unsheared sample until there is no further growth of the aggregating system. The size of the aggregates at the gel point for the shear initiation time of 1min at the given shear rates was $R_{g,G} \sim 4\ \mu m$, similar to that for the no shear situation. Note that the gel time is defined as when the aggregates stop further evolving in an aggregating system (i.e., when the data reach a plateau in Fig. 7.13) .

(ii) For the shear initiation times of **2 min** (shown in (c)) , **3 min** (shown in (d)), and **5 min** (shown in (a) to (d)), shear enhanced the aggregation significantly as depicted by the arrows in each figure (also see Figs. 7.7 and 7.8). At the highest shear rates (3.56 sec^{-1} shown in (d)), shear also induced the gelation of the sample.

(iii) For the shear initiation times of **15 min**, the data initially followed the same curve as that for the unsheared sample; however, applying the shear enhanced the aggregation. At the shear rate of 0.13 sec^{-1}, there were some slight increase in the aggregate size can be seen in Fig 7.13 (a) (sample gelled within a few minutes after the termination of the shear). At shear rates of 0.99, 2.61, and 3.56 sec^{-1}, shear induced the gelation of the sample.

(iv) For the shear initiation times of **5 and 15 min**, the aggregate size at the gel point was slightly larger ($R_{g,G} \sim$ 5-6 μm) compared to that for the shear initiation times of 1 and 3 min ($R_{g,G} \sim 4\ \mu m$). This difference in the aggregate size could be due to some

experimental error or could have some significant meaning, which needs to be investigated more in our future work.

(v) In Fig. 7.13 (b), (c), and (d), corresponding, respectively, to the shear initiation times of 5, 2, and 3 min, a slightly different trend can be seen. These samples where those for which a hybrid aggregate structure was observed initially after the termination of the shear *repaired* later by Brownian aggregation. As can be seen in these figures, after the initial enhancement of the aggregate size (shown by the arrows), the aggregates start to slightly decrease in size until a stable aggregate size was reached at the gel point. We speculate that the decrease in the aggregate size could be due to the restructuring of the aggregates due to shear.

The presented results in this work showed that shear can cause a hybrid aggregate structure. Here the possible mechanism, by which these hybrid structures are formed, will be explained.

In order to emphasize on the effect of shear on the aggregate structures, Figs 7.10 and 7.12 (shown above) are replotted here again, but only the data right before initiation of the shear and immediately after termination of the shear are shown. Figure 7.14 (bottom) shows the scattered intensities for the shear initiation time of **5 min** and the shear rate of $\boldsymbol{\gamma = 3.6\ sec^{-1}}$. Figure 7.14 (top) shows the scattered intensities for the shear initiation time of **15 min** and the shear rate of $\boldsymbol{\gamma = 0.48\ sec^{-1}}$. The vertical arrows in Fig. 7.14 show that shear has enhanced the aggregation; at the same time, as shown with the horizontal arrows, the aggregates have increased in size (i.e., smaller q means larger aggregates $R_g \propto 1/q$). This new shear induced structure between the arrows has an effective fractal dimension of 2.45 ± 0.04 (bottom) and 2.60 ± 0.05 (top)

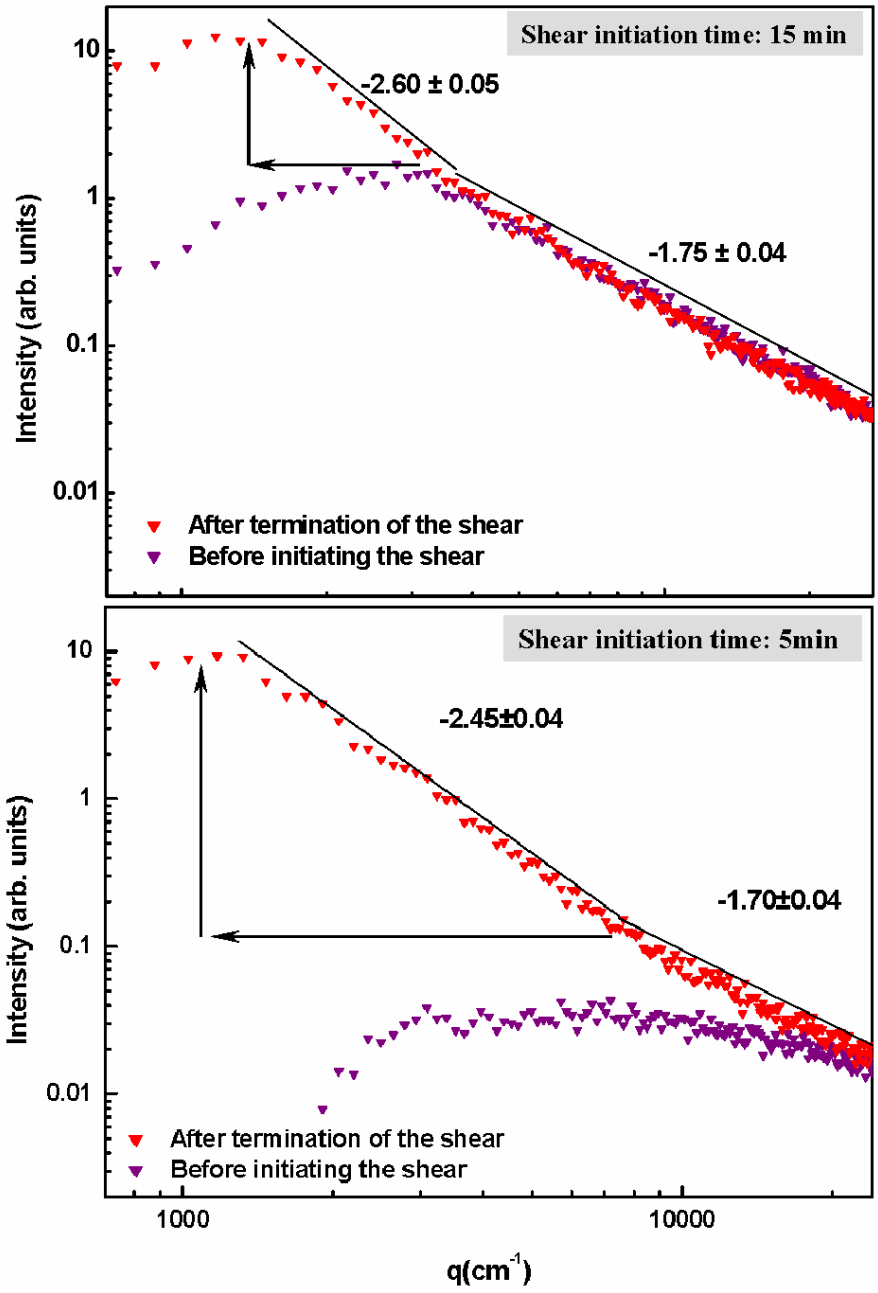

Figure 7.14 (bottom) Light scattering data for the shear initiation time of 5 min and the shear rates of $\gamma = 3.56\ \text{sec}^{-1}$ (top) light scattering data for the shear initiation time of 15 min and the shear rates of $\gamma = 0.48\ \text{sec}^{-1}$.

In the literature, fragmentation and restructuring have been the only mechanisms by which the effects of shear on aggregating systems are discussed. Although, the hybrid aggregate structures are associated with the restructuring mechanism, we will consider both mechanisms here as the possible consequences of shear on the structure of aggregates.

- **Fragmentation**: An aggregate subjected to shear can breakup into smaller aggregates yet remains tenuous (Torres et al 1991a) , or the weaker arms of the aggregate can fall off and cause a more compact, and hence smaller aggregate(Kikuchi et al 2005, Oles 1992, Selomulya et al 2002, Sonntag & Russel 1986). However, Our results showed no indication of fragmentation. Instead, the aggregate radius of gyration increased, for example, from $R_g \approx 500\ nm$ before applying the shear to $R_g \approx 8\,\mu m$ after termination of the shear as shown in Fig. 7.14 (bottom). Eq. (7.1) was also used to estimate an approximate aggregate size that could remain intact under the largest shear rates applied in our experiments. We found that aggregates smaller than 10 μm will not breakup under the largest shear rates applied in our experiments ($\gamma = 3.6\ \text{sec}^{-1}$).

- **Restructuring**: In the work of Lin et al., aggregates, formed of 15 nm gold particles, restructured at high shear rates ($10^4\ \text{sec}^{-1}$) (Lin et al 1990a). Lin et al. found that aggregates subjected to shear decreased in size. Moreover, they found that the degree of restructuring (i.e., higher fractal dimension) depended on the magnitude of the shear applied. In another work by Selomulya et al., relatively large particles (60 nm and 380 nm) was used for the shear experiments ranging from 30-100 sec^{-1} . They also found that aggregates restructured due to shear in their experiments (Selomulya et al 2002). We once again refer to Fig. 7.14, where we see that shear caused an increase in the fractal dimension but also an increase in the cluster size, not a decrease as expected for restructuring. Furthermore, in contrast with the results of Lin et al., our results did not show any increase in the fractal dimension at larger shear rates, and the fractal dimension remained more or less the same independent of the applied shear rate. Therefore, the restructuring mechanism cannot explain our results either.

Recently, in a work from this laboratory, soot aggregates in an acetylene/air laminar diffusion flame were studied using small angle light scattering (Sorensen et al 2003). An inhomogeneous aggregate structure was observed at higher heights above the burner orifice (i.e., late aggregation times). Similar to Fig. 7.14, Sorensen et al. observed a hybrid aggregate structure with two slopes of -1.8 and -2.6 in their light scattering measurements (Sorensen et al 2003). Sorensen et al. proposed that this hybrid structure of the flame soot was an indication of superaggregates, a term coined to mean a large aggregate of a given fractal dimension over large length scales composed of smaller aggregates with a different fractal dimension for their smaller length scale (Sorensen et al 2003). This proposition was based on simulation work by Fry et al. who showed that DLCA can proceed creating $D_f = 1.8$ fractal aggregates until the system becomes cluster dense (i.e., when the cluster mean nearest neighbor separation becomes comparable to the cluster size) (Fry et al 2004). Once cluster dense, the aggregation mechanism can cross over to a percolation mechanism and $D_f = 2.55$ percolated superaggregates (of smaller $D_f = 1.8$ DLCA aggregates) result. Theoretically, the percolation of the aggregates is shown that will eventually occur in all aggregating systems resulting in a cross over between two slopes of -1.8 and -2.55 (Gimel et al 1999, Hasmy & Jullien 1996, Rottereau et al 2004, Stauffer 1992). Yet, in the literature, DLCA colloidal aggregation experiments (no shear) have not shown any evidence of a percolated aggregating system. The cross over length scale between the two slopes of -1.8 and -2.55 is shown to occur when the size of the DLCA aggregates reach the radius of gyration at the gel point $R_{g,G}$, discussed in Chapter 4 (Fry et al 2004).

Figure 7.15 shows a schematic drawing of a superaggregate where the $D_f = 1.8$ fractal aggregates are percolated to form a superaggregate with a fractal dimension of $D_f \sim 2.6$ at larger length scales.

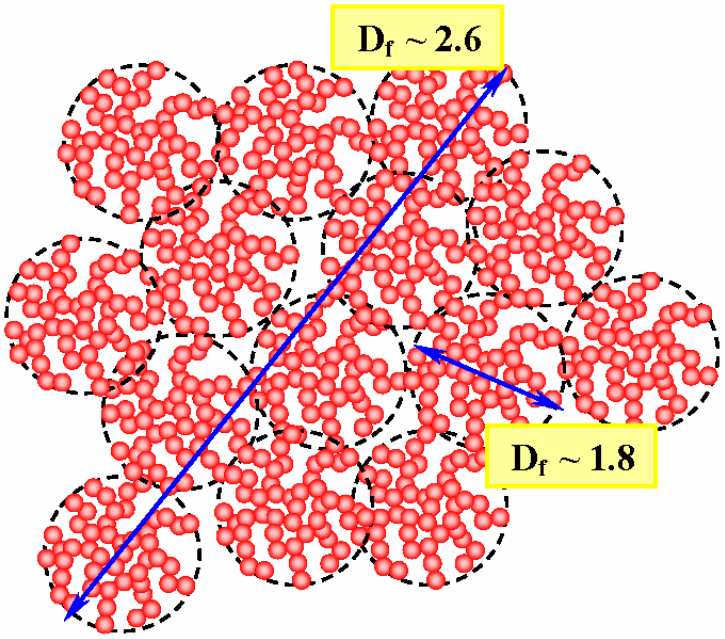

Figure 7.15 A schematic drawing of a superaggregate.

The crossover length scale in our shear experiments (i.e., when a hybrid aggregate structure was observed) was determined with the uncertainty of our experiments. In order to calculate the theoretical $R_{g,G}$ (i.e., $R_{g,G} \approx 0.5\, a\, f_v^{\,1/(\mathrm{D_f}-3)}$), $f_v = 4.36\times10^{-4}$ (used in our experiments) and the fractal dimension given in Tables 7.2 and 7.3 were used; the fractal dimension had some variation from run to run which is included in the error. The experimental and theoretical $R_{g,G}$ are shown in Table 7.5.

As can be seen in Table 7.5, for the shear initiation time of 15 min, there is a good agreement between theory and experimental results. For the shear initiation time of 5 min, the agreement is not as good with the calculated value. It should be noted that $R_{g,G}$ is greatly dependent on any small variation of the fractal dimension; this can be seen in the approximate equation given for $R_{g,G}$. Furthermore, we speculate that this difference between the theoretical and experimental $R_{g,G}$ for shear initiation time of 5 min may be due to the fact that the system was not as deep into the cluster dense regime (i.e., it is farther from the gel point than at 15 min).

The results shown in Table 7.5 support our proposed mechanism of *shear-induced supperaggregates formation*, where shear causes the growth of a hybrid aggregate structure.

Table 7.5 The comparison between calculated $\boldsymbol{R_{g,G}}$ (μm) and the measured $\boldsymbol{R_{g,G}}$ (μm) at shear initiation times of 5 and 15 min.

γ (sec^{-1})	Shear initiation time 5 min		Shear initiation time 15 min	
	Measured $R_{g,G}$ (μm)	Calculated $R_{g,G}$ (μm)	Measured $R_{g,G}$ (μm)	Calculated $R_{g,G}$ (μm)
0.13				
0.24				
0.48			2.8 ± 0.2	2.5 ± 0.5
0.99			2.0 ± 0.2	2.5 ± 0.5
1.60	1.3 ± 0.1	0.6 ± 0.1	1.9 ± 0.2	1.6 ± 0.3
2.61	1.4 ± 0.2	0.6 ± 0.1	1.3 ± 0.1	1.3 ± 0.2
3.56	1.3 ± 0.1	2.0 ± 0.3	2.2 ± 0.1	2.3 ± 0.4

7.5 Conclusions

In a cluster dilute regime, applying a shear did not enhance the aggregation kinetics leading to a gel structure indistinguishable from that formed via a DLCA process, $D_f = 1.80 \pm 0.04$. In a cluster dense regime and at low shear rates, shear enhanced the aggregation and the gel structure was uniform with a fractal dimension of $D_f = 1.75 \pm 0.04$. In a cluster dense regime and at moderate to high shear rates, shear caused the sample to reach the gel point with a hybrid aggregate structure with the fractal dimensions of $D_f = 1.70 \pm 0.05$ and $D_f = 2.55 \pm 0.05$.Moreover, we see no evidence for fragmentation or restructuring due to the

shear in our data. Moreover, the previous literature has no evidence for shear causing *growth to a hybrid structure*. We also found that the fractal dimension of the hybrid aggregate structure of the sheared sample did not increase by increasing the shear rates. These results are different than the work of Lin et al. and Selomulya et al. in which the fractal dimension increased by increasing the shear rates; these groups proposed that shear induced-restructuring occurred in their experiments (Lin et al 1990a, Selomulya et al 2002).

CHAPTER 8 Conclusions

The focus of this work has been on the experimental investigation of the effects of shearing on the structure and the aggregation kinetics of an aggregating colloidal system. It is well known that the aggregation of particles in a colloidal system can be controlled by three different mechanisms including Brownian aggregation, shear-induced aggregation, and differential sedimentation aggregation.

Small angle light scattering experiments were conducted with 20 nm monodisperse polystyrene sols induced to aggregate in the diffusion-limited regime by the addition of $MgCl_2$. The morphology and the growth kinetics of the aggregating system when subjected to a shear field (γ = 0.13- 3.56 sec^{-1}) was studied. In our experiments, shear was applied only once (ca. 30 seconds) at various times (1-15 minutes) after the onset of aggregation.

In a cluster dilute regime, applying a shear did not enhance the aggregation kinetics leading to a gel structure indistinguishable from that formed via a DLCA process, $D_f = 1.80 \pm 0.04$. In a cluster dense regime and at low shear rates, shear enhanced the aggregation and the gel structure was uniform with a fractal dimension of $D_f = 1.75 \pm 0.04$. In a cluster dense regime and at moderate to high shear rates, shear caused the sample to reach the gel point with a hybrid aggregate structure with the fractal dimensions of $D_f = 1.70 \pm 0.05$ and $D_f = 2.55 \pm 0.05$.

Our experimental results have shown that shear may enhance the aggregation and gelation causing structural modification, not by shear destruction of aggregates (fragmentation or restructuring), but by shear induced growth, a new mechanism by which superaggregates form in a shear field. Hence, our results have introduced a new consequence of shear morphological effects to the previous shear studies which observed only shear-induced restructuring or

fragmentation. Our shear experiments have also shown a new feature in which Brownian aggregation "repairs" the hybrid aggregate structure formed initially due to shear.

Similar to shearing experiments, initial mixing of an unstable aggregating system can affect the aggregation kinetics. A series of light scattering measurements were carried out to study the effect of initial mixing on the gel time. Our light scattering measurements of the gel times have shown quantitative agreement between theoretical and experimental gel time at low volume fractions $f_v < 6 \times 10^{-5}$. However, at high volume fractions of the polystyrene colloidal solutions, the theoretical and experimental gel times differ by orders of magnitudes, with a much faster theoretical gel time. These gel time experiments have only been performed in a RLCA regime (slow regime), where initial mixing is negligible compared to their experimental gel time (Bremer et al 1995, Smith & Zukoski 2006). Yet, there are more experiments to be done in future to resolve this interesting enigmatic problem.

Relevant to our light scattering measurements, the extent and effect of multiple scattering on angularly resolved light scattering measurements were studied. For simple interpretation of light scattering experiments, it is important to have single scattering. Therefore, it is important to be aware of how multiple scattering can affect light scattering measurements, how to detect it, and how one can possibly avoid it. Our experimental results have shown that the average number of scattering events is a universal parameter to describe the extent of multiple scattering. This quantity can easily be measured or calculated hence provides a useful experimental indicator of multiple scattering.

References

Adachi Y. 1995. Dynamic Aspects of Coagulation and Flocculation. *Advances in Colloid and Interface Science* 56: 1-31

Allain C, Cloitre M. 1993. The Effects of Gravity on the Aggregation and the Gelation of Colloids. *Advances in Colloid and Interface Science* 46: 129-38

Allain C, Cloitre M, Wafra M. 1995. Aggregation and Sedimentation in Colloidal Suspensions. *Physical Review Letters* 74: 1478-81

Asnaghi D, Carpineti M, Giglio M, Sozzi M. 1992. Coagulation Kinetics and Aggregate Morphology in the Intermediate Regimes between Diffusion-Limited and Reaction-Limited Cluster Aggregation. *Physical Review A* 45: 1018-23

Berg MJ, Sorensen CM, Chakrabarti A. 2005. Patterns in Mie scattering: Evolution When Normalized by the Rayleigh Cross Section. *Applied Optics* 44: 7487-93

Berne BJ, Pecora R. 2000. *Dynamic Light Scattering: With Applications to Chemistry, Biology, and Physics*: Dover Publications. 384 pp.

Bohren CE, Huffman DR, eds. 1983. *Absorption and Scattering of Light by Small Particles*. New York: John Wiley & Sons, Inc.

Bremer LGB, Walstra P, Vanvliet T. 1995. Estimations of the Aggregation Time of Various Colloidal Systems. *Colloids and Surfaces a-Physicochemical and Engineering Aspects* 99: 121-7

Brinker CJ, Scherer GW. 1990. *Sol-Gel Science: The Physics and Chemistry of Sol-Gel Processing*. San Diego: Academic Press, Inc.

Brown W, ed. 1993. *Dynamic Light Scattering; The Method and Some Applications*: Oxford University Press

Carpineti M, Ferri F, Giglio M, Paganini E, Perini U. 1990. Salt-Induced Fast Aggregation of Polystyrene Latex. *Physical Review A* 42: 7347-54

Carpineti M, Giglio M. 1992. Spinodal-Type Dynamics in Fractal Aggregation of Colloidal Clusters. *Physical Review Letters* 68: 3327-30

Cerda JJ, Sintes T, Sorensen CM, Chakrabarti A. 2004. Structure factor scaling in colloidal phase separation. *Physical Review E* 70

Cipelletti L, Manley S, Ball RC, Weitz DA. 2000. Universal aging features in the restructuring of fractal colloidal gels. *Physical Review Letters* 84: 2275-8

Clarke SM, Ottewill RH, Rennie AR. 1995. Light-Scattering-Studies of Dispersions under Shear. *Advances in Colloid and Interface Science* 60: 95-118

Dhaubhadel R, Pierce F, Chakrabarti A, Sorensen CM. 2006. Hybrid Superaggregate Morphology as a Result of Aggregation in a Cluster-Dense Aerosol. *Physical Review E* 73

Dickinson E. 2000. Structure and rheology of simulated gels formed from aggregated colloidal particles. *Journal of Colloid and Interface Science* 225: 2-15

Drake RL. 1972. A General Mathematical Survey of The Coagulation Equation. In *Topics in Current Aerosol Research (Part 2)*, ed. GM Hidy, JR Brock. New York: Pergamon Press

Evans DF, Wennerström H. 1999. *The Colloidal Domain: Where Physics, Chemistry, Biology, and Technology Meet*. New York: Wiley-VCH

Family F, Maters BR, Platt DE. 1989. Fractal Pattern Formation in Human Retinal Vessels. In *Fractals in Physics*, ed. A Aharony, J Feder. Vence, France: Elsevier Science Publishers

Feke DL, Schowalter WR. 1985. The Influence of Brownian Diffusion on Binary Flow-Induced Collision Rates in Colloidal Dispersions. *Journal of Colloid and Interface Science* 106: 203-14

Ferri F. 1997. Use of a Charge Coupled Device Camera for Low-Angle Elastic Light Scattering. *Review of Scientific Instruments* 68: 2265-74

Flesch JC, Spicer PT, Pratsinis SE. 1999. Laminar and turbulent shear-induced flocculation of fractal aggregates. *Aiche Journal* 45: 1114-24

Friedlander SK. 2000. *Smoke, Dust, and Haze: Fundamentals of Aerosol Dynamics (Topics in Chemical Engineering)*. New York: Oxford University Press

Fry D, Chakrabarti A, Kim W, Sorensen CM. 2004. Structural crossover in dense irreversibly aggregating particulate systems. *Physical Review E* 69

Fry D, Sintes T, Chakrabarti A, Sorensen CM. 2002. Enhanced kinetics and free-volume universality in dense aggregating systems. *Physical Review Letters* 89

Gimel JC, Nicolai T, Durand D. 1999. 3D Monte Carlo simulations of diffusion limited cluster aggregation up to the sol-gel transition: Structure and kinetics. *Journal of Sol-Gel Science and Technology* 15: 129-36

Gonzalez AE. 2001. Colloidal aggregation with sedimentation: Computer simulations. *Physical Review Letters* 86: 1243-6

Gonzalez AE, Ramirezsantiago G. 1995. Spatial Ordering and Structure Factor Scaling in the Simulations of Colloid Aggregation. *Physical Review Letters* 74: 1238-41

Goodwin J. 2004. *Colloids and Interfaces with Surfactants and Polymers: An Introduction*. New York: John Wiley & Sons

Guinier A, Fournet G. 1955. *Small Angle Scattering of X-Rays*: John Wiley & Sons, Inc.

Hashimoto T, Takebe T, Suehiro S. 1986. Apparatus to Measure Small-Angle Light-Scattering Profiles of Polymers under Shear-Flow. *Polymer Journal* 18: 123-30

Hasmy A, Jullien R. 1996. Percolation in cluster-cluster aggregation processes. *Physical Review E* 53: 1789-94

Hecht E. 2002. *Optics*. San Fracisco: Pearson Education

Hiemenz PC. 1986. *Principles of Colloid and Surface Chemistry*. New York: Marcel Dekker, Inc.

Hirt CW, Nichols BD. 1981. Volume of Fluid (Vof) Method for the Dynamics of Free Boundaries. *Journal of Computational Physics* 39: 201-25

Hirtzel CS, Rajagopalan R. 1985. *Colloidal Phenomena: Advanced Topics*. New Jersey: Noyes Publications

Hoekstra H, Vermant J, Mewis J. 2003. Flow-induced anisotropy and reversible aggregation in two-dimensional suspensions. *Langmuir* 19: 9134-41

Huang H, Oh C, Sorensen CM. 1998. Structure factor scaling in aggregating systems. *Physical Review E* 57: 875-80

Hunter RJ. 1994. *Introduction to Modern Colloid Science*. New York: Oxford University Press

Israelachvili J. 2006. *Intermolecular and Surface Forces*. San Diego: Academic Press

Jullien R. 1992. From Guinier to Fractals. *Journal De Physique I* 2: 759-70

Jullien R, Botet R. 1987. *Aggregation and fractal aggregates*. Singapore: World Scientific

Jullien R, Thouy R, Ehrburgerdolle F. 1994. Numerical Investigation of 2-Dimensional Projections of Random Fractal Aggregates. *Physical Review E* 50: 3878-82

Kerker M. 1969. *The Scattering of Light and Other Electromagnetic Radiation*. New York and London: Academic Press, Inc. 666 pp.

Kikuchi Y, Yamada H, Kunimori H, Tsukada T, Hozawa M, et al. 2005. Aggregation behavior of latex particles in shear flow confined between two parallel plates. *Langmuir* 21: 3273-8

Kim W, Sorensen CM, Chakrabarti A. 2004. Universal Occurrence of Soot Superaggregates with a Fractal Dimension of 2.6 in Heavily Sooting Laminar Diffusion Flames. *Langmuir* 20: 3969-73

Kolb M, Botet R, Jullien R. 1983. Scaling of Kinetically Growing Clusters. *Physical Review Letters* 51: 1123-6

Lattuada M, Wu H, Morbidelli M. 2001. Estimation of Fractal Dimension of Colloidal Gels in the Presence of Multiple Scattering. *Physical Review E* 6406

Lin MY, Klein R, Lindsay HM, Weitz DA, Ball RC, Meakin P. 1990a. The Structure of Fractal Colloidal Aggregates of Finite Extent. *Journal of Colloid and Interface Science* 137: 263-80

Lin MY, Lindsay HM, Weitz DA, Ball RC, Klein R, Meakin P. 1989. Universality in Colloid Aggregation. *Nature* 339: 360-2

Lin MY, Lindsay HM, Weitz DA, Ball RC, Klein R, Meakin P. 1990b. Universal Reaction-Limited Colloid Aggregation. *Physical Review A* 41: 2005-20

Lin MY, Lindsay HM, Weitz DA, Klein R, Ball RC, Meakin P. 1990c. Universal Diffusion-Limited Colloid Aggregation. *Journal of Physics-Condensed Matter* 2: 3093-113

Lindsay HM, Lin MY, Weitz DA, Sheng P, Chen Z, et al. 1987. Properties of Fractal Colloid Aggregates. *Faraday Discussions*: 153-65

Lumma D, Lurio LB, Borthwick MA, Falus P, Mochrie SGJ. 2000. Structure and dynamics of concentrated dispersions of polystyrene latex spheres in glycerol: Static and dynamic x-ray scattering. *Physical Review E* 62: 8258-69

Mandelbrot BB. 1983. *The Fractal Geometry of Nature*. New York, San Francisco: Freeman and Company

Meakin P. 1983. Formation of Fractal Clusters and Networks by Irreversible Diffusion-Limited Aggregation. *Physical Review Letters* 51: 1119-22

Meakin P. 1988. Fractal Aggregates. *Advances in Colloid and Interface Science* 28: 249-331

Mishchenko MI. 2002. Vector Radiative Transfer Equation for Arbitrarily Shaped and Arbitrarily Oriented Particles: a Microphysical Derivation from Statistical Electromagnetics. *Applied Optics* 41: 7114-34

Mishchenko MI, Hovenier JW, Mackowski DW. 2004. Single Scattering by a Small Volume Element. *Journal of the Optical Society of America a-Optics Image Science and Vision* 21: 71-87

Mishchenko MI, Travis LD, Lacis AA. 2002. *Scattering, Absorption, and Emission of Light by Small Particles*: Cambridge University Press. 480 pp.

Mitsugu M. 1989. Experimental observation of aggregation. In *The Fractal Approach to Heterogeneous Chemistry: Surfaces, Colloids, Polymers*, ed. D Avnir: John Wiley & Sons Ltd

Mokhtari T, Sorensen CM, Chakrabarti A. 2005. Multiple-scattering Effects on Static Light-Scattering Optical Structure Factor Measurements. *Applied Optics* 44: 7858-61

Monk GS. 1937. *Light*. New York & London: McGraw Hill Book Company, Inc. 477 pp.

Oh C, Sorensen CM. 1997. The effect of overlap between monomers on the determination of fractal cluster morphology. *Journal of Colloid and Interface Science* 193: 17-25

Oh C, Sorensen CM. 1999. Scaling Approach for the Structure Factor of a Generalized System of Scatterers. *Journal of Nanoparticle Research* 1: 369-77

Oles V. 1992. Shear-Induced Aggregation and Breakup of Polystyrene Latex-Particles. *Journal of Colloid and Interface Science* 154: 351-8

Ottewill RH, Shaw JN. 1966. Stability of Monodisperse Polystyrene Latex Dispersions of Various Sizes. *Discussions of the Faraday Society*: 154-&

Peitgen HO, Jürgens H, Saupe D. 1991. *Fractals for the Classroom: Part one: Introduction to Fractals and Chaos*: Springer. 452 pp.

Peker S. 2007. Role of Surface Forces in the Formation and Stability of Fractal Structures. In *Colloid Stability: The Role of Surface Forces-Part 1*, ed. TF Tadros. New York: Wiley - VCH

Pesic P. 2005. *Sky in a Bottle*: The MIT Press. 270 pp.

Pfeifer P, Obert M. 1989. Fractals: Basic Concepts and Terminology. In *The Fractal Approach to Heterogeneous Chemistry: Surfaces, Colloids, Polymers*, ed. D Avnir: John Wiley & Sons Ltd

Poulin P, Bibette J, Weitz DA. 1999. From colloidal aggregation to spinodal decomposition in sticky emulsions. *European Physical Journal B* 7: 277-81

Rottereau M, Gimel JC, Nicolai T, Durand D. 2004. Monte Carlo simulation of particle aggregation and gelation: I. Growth, structure and size distribution of the clusters. *European Physical Journal E* 15: 133-40

Russel WB, Saville DA, Schowalter WR. 1999. *Colloidal Dispersions*. Cambridge: Cambridge University Press

Selomulya C, Bushell G, Amal R, Waite TD. 2002. Aggregation mechanisms of latex of different particle sizes in a controlled shear environment. *Langmuir* 18: 1974-84

Serra T, Casamitjana X. 1998. Structure of the aggregates during the process of aggregation and breakup under a sheer flow. *Journal of Colloid and Interface Science* 206: 505-11

Serra T, Colomer J, Casamitjana X. 1997. Aggregation and breakup of particles in a shear flow. *Journal of Colloid and Interface Science* 187: 466-73

Smith WE, Zukoski CE. 2006. Aggregation and gelation kinetics of fumed silica-ethanol suspensions. *Journal of Colloid and Interface Science* 304: 359-69

Somasundaran P, Markovic B, Krishnakumar S, Yu X. 1997. Colloid Systems and Interfaces Stability of Dispersions Through Polymer and Surfactant Adsorption. In *Handbook of Surface and Colloid Chemistry*, ed. KS Birdi. New York, Boca Raton: CRC Press

Sonntag H. 1993. Coagulation Kinetics. In *Coagulation and Flocculation: Theory and Applications*, ed. B Dobias. New York: Marcel Dekker, Inc.

Sonntag H, Strenge K. 1987. *Coagulation Kinetics and Structure Formation*. New York: Plenum Press

Sonntag RC, Russel WB. 1986. Structure and Breakup of Flocs Subjected to Fluid Stresses .1. Shear Experiments. *Journal of Colloid and Interface Science* 113: 399-413

Sorensen CM. 1997. Scattering and Absorption of Light by Particles and Aggregates. In *Handbook of Surface and Colloid Chemistry*, ed. KS Birdi. New York, Boca Raton: CRC Press

Sorensen CM. 2001. Light Scattering by Fractal Aggregates: A Review. *Aerosol Science and Technology* 35: 648-87

Sorensen CM, Cai J, Lu N. 1992. Test of Static Structure Factors for Describing Light-Scattering from Fractal Soot Aggregates. *Langmuir* 8: 2064-9

Sorensen CM, Fischbach DJ. 2000. Patterns in Mie scattering. *Optics Communications* 173: 145-53

Sorensen CM, Hageman B, Rush TJ, Huang H, Oh C. 1998. Aerogelation in a flame soot aerosol. *Physical Review Letters* 80: 1782-5

Sorensen CM, Kim W, Fry D, Shi D, Chakrabarti A. 2003. Observation of soot superaggregates with a fractal dimension of 2.6 in laminar acetylene/air diffusion flames. *Langmuir* 19: 7560-3

Sorensen CM, Roberts GC. 1997. The prefactor of fractal aggregates. *Journal of Colloid and Interface Science* 186: 447-52

Sorensen CM, Wang GM. 1999. Size Distribution Effect on the Power Law Regime of the Structure Factor of Fractal Aggregates. *Physical Review E* 60: 7143-8

Spicer PT, Keller W, Pratsinis SE. 1996. The effect of impeller type on floc size and structure during shear-induced flocculation. *Journal of Colloid and Interface Science* 184: 112-22

Stanley HE. 1985. Form: An Introduction to Self-Similarity and Fractal Behavior. In *On Growth and Form: Fractal and Non-Fractal Patterns in Physics*, ed. HE Stanley, N Ostrowsky. France: Martinus Nijhoff Publishers

Stauffer D. 1992. *Introduction to Percolation Theory*. London: Taylor & Francis

Stauffer D, Stanley HE. 1990. *From Newton to Mandelbrot: A Primer in Theoretical Physics*: Springer-Verlag Telos. 191 pp.

Strenge K. 1993. Structure Formation in Disperse Systems. In *Coagulation and Flocculation: Theory and Applications*, ed. B Dobias. New York: Marcel Dekker, Inc.

Swift DL, Friedlander SK. 1964. Coagulation of Hydrosols by Brownian Motion + Laminar Shear Flow. *Journal of Colloid Science* 19: 621-&

Tadros TF. 2007. General Principles of Colloid Stability and the Role of Surface Forces. In *Colloid Stability: The Role of Surface Forces-Part 1*, ed. TF Tadros. New York: Wiley - VCH

Tannehill JC, Anderson DA, Pletcher RH. 1997. *Computational Fluid Mechanics and Heat Transfer*. London: Taylor & Francis

Torres FE, Russel WB, Schowalter WR. 1991a. Floc Structure and Growth-Kinetics for Rapid Shear Coagulation of Polystyrene Colloids. *Journal of Colloid and Interface Science* 142: 554-74

Torres FE, Russel WB, Schowalter WR. 1991b. Simulations of Coagulation in Viscous Flows. *Journal of Colloid and Interface Science* 145: 51-73

Urban C, Schurtenberger P. 1998. Characterization of Turbid Colloidal Suspensions Using Light Scattering Techniques Combined with Cross-Correlation Methods. *Journal of Colloid and Interface Science* 207: 150-8

van de Hulst HC. 1957. Light Scattering by Small Particles. pp. 470: John Wiley & Sons, Inc.

Varadan P, Solomon MJ. 2001. Shear-induced microstructural evolution of a thermoreversible colloidal gel. *Langmuir* 17: 2918-29

Verwey EJW, Overbeek JTG. 1947. *Theory of the Stability of Lyophobic Colloids*. New York: Elsevier Publishing Co.

Vicsek T. 1992. *Fractal Growth Phenomena*: World Scientific Publishing Co. Pte. Ltd. 380 pp.

Victor JM, Hansen JP. 1984. Liquid-Gas Transition in Charged Colloidal Dispersions. *Journal De Physique Lettres* 45: L307-L12

Voss RF. 1989. Random Fractals: Self-affinity in Noise, Music, Mountains, and Clouds. In *Fractals in Physics*, ed. A Aharony, J Feder. Vence, France: Elsevier Science Publishers

Wang L, Marchisio DL, Vigil RD, Fox RO. 2005. CFD simulation of aggregation and breakage processes in laminar Taylor-Couette flow. *Journal of Colloid and Interface Science* 282: 380-96

Weber V, Schosseler F. 2002. Absolute Small Angle Light Scattering Measurements from Weakly Scattering Systems in a Shear Flow Apparatus. *Review of Scientific Instruments* 73: 2537-43

West AHL, Melrose JR, Ball RC. 1994. Computer-Simulations of the Breakup of Colloid Aggregates. *Physical Review E* 49: 4237-49

Witten TA, Sander LM. 1981. Diffusion-Limited Aggregation, a Kinetic Critical Phenomenon. *Physical Review Letters* 47: 1400-3

Yan YD, Dhont JKG, Smits C, Lekkerkerker HNW. 1994. Oscillatory-Shear-Induced Order in Nonaqueous Dispersions of Charged Colloidal Spheres. *Physica A* 202: 68-80

Zeichner GR, Schowalter WR. 1979. Effects of Hydrodynamic and Colloidal Forces on the Coagulation of Dispersions. *Journal of Colloid and Interface Science* 71: 237-53